



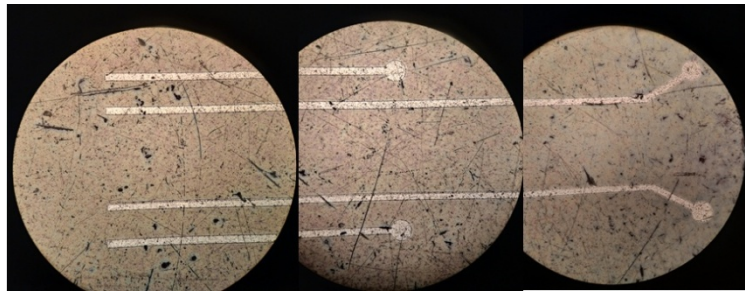
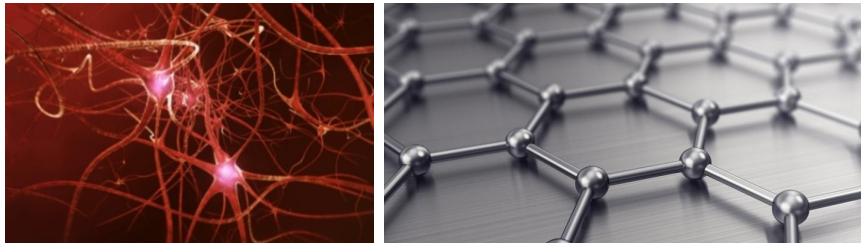
University of Crete

Department of **MATERIALS SCIENCE AND TECHNOLOGY**

SCHOOL OF SCIENCES AND ENGINEERING

MASTER THESIS - ΜΕΤΑΠΤΥΙΑΚΗ ΕΡΓΑΣΙΑ

**DEVELOPMENT OF GRAPHENE-BASED ELECTRODES FOR  
BIOELECTRONIC DEVICES**



PYLOSTOMOU ATHANASIA

ΠΥΛΟΣΤΟΜΟΥ ΑΘΑΝΑΣΙΑ

MASTER THESIS COMMITTEE / ΤΡΙΜΕΛΗΣ ΕΠΙΤΡΟΠΗ ΔΕΠ:

DR. EMMANUEL STRATAKIS, FOUNDATION FOR RESEARCH AND  
TECHNOLOGY-HELLAS (FORTH)

PROF. GEORGE KIOSEOGLU, UNIVERSITY OF CRETE (UOC)

PROF. ANNA MITRAKI, UNIVERSITY OF CRETE (UOC)



*"Any sufficiently advanced technology  
is indistinguishable from magic".*

*Arthur C. Clarke*



## ACKNOWLEDGEMENTS

I would like to thank Professors George Kioseoglou and Anna Mitraki that accepted to be supervising professors of my master thesis and also Dr. Emmanuel Stratakis, my supervising researcher, for trusting me in completing this project. Special thanks to my subgroup leader, Dr. Maria Pervolaraki, who was close to me at every step of the experiments. Her guidance and valuable advice have been crucial to the progress of my work. Many thanks to the other members of my subgroup team, especially to Dr. Kyriaki Savva and Dr. Abdus Salam Sarkar, who helped me with the laser training and the characterization techniques and who gave me important advice.

I would also like to thank Dr. George Kenanakis for the FTIR characterizations and his knowledge which is invaluable. Furthermore, many thank addressing to Mrs. Aleka Manousaki for the FESEM images and to Dr. Zacharias Viskadourakis for the I-V measurements. Furthermore, among the people I would like to thank for their help in my master thesis are Andreas Lemonis for helping me in technical issues and programming and also George Veisakis and Dr. Minas Stylianakis from Hellenic Mediterranean University (HMU) for the spray coating technique.

Moreover, I would like to thank my friends for their support and understanding (even if they missed me a lot) for all the evenings, nights, weekends and days-off that I had to work extra, instead of join their company. Finally, I could not, but thank with all my heart my family, who always supports me, empowers me morally and mentally and who will always be by my side, proud, in every single step.

The work reported in this thesis has been conducted at the Ultrafast Laser Micro- and Nano-Processing (ULMNP) laboratory of the Institute of Electronic Structure and Laser (IESL) of the Foundation for Research and Technology–Hellas (FORTH). This research was conducted within the European Commission FLAG-ERA Joint Transnational Call (JTC) 2017 under the EPIGRAPH project (European Reference Code: 26632, National Reference Code: T8EPA2-00008).



# CONTENTS

<b>ABBREVIATIONS</b> .....	<b>III</b>
<b>ABSTRACT</b> .....	<b>V</b>
<b>ΠΕΡΙΛΗΨΗ</b> .....	<b>VI</b>
<b>INTRODUCTION</b> .....	<b>1</b>
<b>CHAPTER 1 – ULTRAFAST FEMTOSECOND LASERS AND REDUCTION OF GRAPHENE OXIDE</b> .....	<b>4</b>
1.1 Lasers .....	4
1.2 Laser Reduction .....	7
1.3 Ultrafast Femtosecond lasers vs. Long-pulsed and Continuous Wave Lasers . . .	8
<b>CHAPTER 2 – GRAPHENE AND GRAPHENE-BASED ELECTRODES FOR BIOSENSING</b> .....	<b>11</b>
2.1 Graphene and Graphene Oxide: History, Background and Structure .....	11
2.2 Graphene Properties .....	13
2.3 Graphene and Graphene-based materials Applications .....	14
2.4 Graphene-based electrodes .....	15
2.5 Biosensors and Graphene .....	16
2.5.1 Biosensors .....	16
2.5.2 Graphene-based biosensors .....	17
<b>CHAPTER 3 – CHARACTERIZATION TECHNIQUES</b> .....	<b>20</b>
3.1 Ultra-violet Visible Infrared Spectroscopy (UV-Vis) .....	20
3.2 Raman Spectroscopy .....	22
3.3 Fourier Transform Infrared Spectroscopy - Attenuated Total Reflectance (FTIR-ATR) .....	26
3.4 Optical Microscopy .....	29
3.5 Field Emission Scanning Electron Microscopy (FESEM) .....	31
3.6 Electrical Measurements .....	33
<b>CHAPTER 4 - EXPERIMENTAL METHODS, SET-UP AND PROCEDURE</b> .....	<b>35</b>
4.1 Experimental methods .....	35
4.2 Experimental set-up .....	37
4.3 Experimental procedure .....	38

<b>CHAPTER 5 – RESULTS AND DISCUSSION .....</b>	<b>40</b>
5.1 Vacuum filtration (on membranes and commercial glass substrates) .....	40
5.2 Spray gun (on commercial glass substrates) .....	43
5.3 Spray gun (on commercial glass and polymer substrates) .....	46
5.4 Optimized laser reduction conditions .....	56
5.4.1 Raman mapping .....	56
5.4.2 Electrical measurements .....	64
5.4.3 Optimization of the lower laser fluences .....	69
5.5 Fabrication of the electrodes – Laser reduction of Graphene Oxide (LrGO) ...	81
5.6 Characterization of both GO and the produced laser reduced GO electrodes ...	84
<b>CHAPTER 6 – CONCLUSIONS AND FUTURE WORK .....</b>	<b>91</b>
<b>REFERENCES .....</b>	<b>94</b>

## ABBREVIATIONS

<b>2D</b>	Two- dimensional
<b>NMs</b>	Nanomaterials
<b>GO</b>	Graphene Oxide
<b>rGO</b>	Reduced Graphene Oxide
<b>MRI</b>	Magnetic Resonance Imaging
<b>EEG</b>	Electroencephalogram
<b>LASER</b>	Light Amplification by Stimulated Emission of Radiation
<b>EM</b>	Electromagnetic
<b>CW</b>	Continuous Wave
<b>HAZ</b>	Heat-affected zone
<b>YAG</b>	Yttrium-Aluminium-Garnet
<b>IUPAC</b>	International Union of Pure and Applied Chemistry
<b>ITO</b>	Indium Tin Oxide
<b>LED</b>	Light Emission Diode
<b>FET</b>	Field-Effect Transistor
<b>AZO</b>	Aluminium-zinc Oxide
<b>CNTs</b>	Carbon Nanotubes
<b>PEDOT:PSS</b>	Poly(3,4-ethylenedioxythiophene) poly(styrenesulfonate)
<b>CVD</b>	Chemical Vapor Deposition
<b>H<sub>2</sub>O<sub>2</sub></b>	Hydrogen Peroxide
<b>DNA</b>	Deoxyribonucleic acid
<b>GO<sub>x</sub></b>	Glucose Oxidase
<b>NPs</b>	Nanoparticles
<b>OEIP</b>	Organic Electronic Ion Pump

<b>GABA</b>	Gamma- Aminobutyric Acid
<b>UV-Vis</b>	Ultraviolet-Visible or Ultraviolet-Visible Infrared
<b>HOMO</b>	Higher Occupied Molecular Orbital
<b>LUMO</b>	Lowest Unoccupied Molecular Orbital
<b>a.u.</b>	Arbitrary Units
<b>CCD</b>	Charge coupled device
<b>IR</b>	Infrared
<b>FWHM</b>	Full Width at Half Maximum
<b>FTIR-ATR</b>	Fourier-Transform Infrared – Attenuated Total Reflectance
<b>T</b>	Transmittance
<b>A</b>	Absorbance
<b>FE(SEM)</b>	Field-Emission (Scanning Electron Microscopy)
<b>I-V</b>	Current-Voltage
<b>SI</b>	System International
<b>MCE</b>	Mixed-Cellulose Ester
<b>Yb:KGW</b>	Ytterbium: Potassium Gadolinium Tungstate
<b>OM</b>	Optical Microscope
<b>LiU</b>	Linköping University
<b>EDS</b>	Energy-dispersive X-ray Spectroscopy
<b>EPI.SG</b>	Epigraph.Spray Gun
<b>TG</b>	Commercial glass
<b>LG</b>	LiU glass
<b>LrGO</b>	Laser reduced Graphene Oxide
<b>Rs</b>	Sheet Resistance

## ABSTRACT

During the last decades, the field of bioelectronics is becoming increasingly important due to the demand for clinical detection of various diseases. Epilepsy is a common neurological disorder, affecting millions of people around the world. It is known that metabolic disturbances are often associated with the seizures of epilepsy. According to preliminary studies, amongst other biomarkers, glucose levels can be used for the prediction of incoming seizures, therefore, the creation of specific bioelectronic devices, such as biomolecular sensors, is of great importance. For neurological disorder detection, there is a tremendous need for hydrophilic, biocompatible and highly conductive electrodes in biosensors. Two-dimensional (2D) graphene-based nanomaterials (NMs) exhibit promising physical, optical and electrochemical properties for ultrasensitive bioelectronic devices.

In this work, two dimensional (2D) reduced graphene oxide (rGO) based microelectrodes are developed for use in a biomolecular sensor. The graphene oxide (GO) films were mainly fabricated by spray gun technique. The topography and the composition of the GO films were studied by various microscopic and spectroscopic techniques, respectively. For the enhancement of the electronic properties, an ultrafast pulsed laser was used for the reduction of the GO material.

*Key words: bioelectronics, biosensors, microelectrodes, graphene-based materials, reduced graphene oxide, neurological disorders, Epilepsy.*

## ΠΕΡΙΛΗΨΗ

Τις τελευταίες δεκαετίες, το πεδίο της βιοηλεκτρονικής γίνεται όλο και πιο σημαντικό λόγω της ζήτησης για κλινική ανίχνευση διαφόρων ασθενειών. Η επιληψία είναι μια κοινή νευρολογική διαταραχή που πλήττει εκατομμύρια ανθρώπους σε όλο τον κόσμο. Είναι γνωστό ότι οι μεταβολικές διαταραχές συχνά συνδέονται με τις επιληπτικές κρίσεις. Σύμφωνα με προκαταρκτικές μελέτες, μεταξύ άλλων βιολογικών δεικτών, τα επίπεδα γλυκόζης μπορούν να χρησιμοποιηθούν για την πρόβλεψη επερχόμενων επιληπτικών κρίσεων, επομένως, χρήζει μεγάλης σημασίας η δημιουργία συγκεκριμένων βιοηλεκτρονικών συσκευών, όπως βιομοριακών αισθητήρων. Για την ανίχνευση νευρολογικών διαταραχών, υπάρχει μεγάλη ανάγκη για υδρόφιλα, βιοσυμβατά και εξαιρετικά αγωγίμα ηλεκτρόδια σε βιοαισθητήρες. Τα δισδιάστατα (2D) νανοϋλικά με βάση το γραφένιο εμφανίζουν πολλά υποσχόμενες φυσικές, οπτικές και ηλεκτροχημικές ιδιότητες για τις υπερευαίσθητες βιοηλεκτρονικές συσκευές.

Σε αυτή τη μεταπτυχιακή εργασία, αναπτύχθηκαν δισδιάστατα μικροηλεκτρόδια (μ-ηλεκτρόδια) ανηγμένου οξειδίου του γραφενίου (rGO) για χρήση σε έναν βιομοριακό αισθητήρα. Τα λεπτά υμένια οξειδίου του γραφενίου (GO) κατασκευάστηκαν κυρίως με τεχνική ψεκασμού μέσω αέρα (spray gun). Η τοπογραφία και η σύνθεση των λεπτών υμενίων GO μελετήθηκαν με διάφορες μικροσκοπικές και φασματοσκοπικές τεχνικές, αντίστοιχα. Για την ενίσχυση των ηλεκτρονικών ιδιοτήτων του οξειδίου του γραφενίου χρησιμοποιήθηκε ένα εξαιρετικά γρήγορο παλλόμενο λέιζερ για την αναγωγή του υλικού (rGO). Έρευνα για την ηλεκτρική αγωγιμότητα διεξήχθη προκειμένου να κατανοηθεί η ενίσχυση της ηλεκτρονικής συμπεριφοράς των κατασκευασμένων ηλεκτροδίων. Τέλος, τα μ-ηλεκτρόδια αναπτύχθηκαν μέσω απευθείας σχηματισμού με χρήση λέιζερ (femtosecond) προς την υλοποίηση του μικροηλεκτρονικού αισθητήρα.

*Λέξεις κλειδιά: βιο-ηλεκτρονικές διατάξεις, βιοαισθητήρες, μικροηλεκτρόδια, υλικά με βάση το γραφένιο, ανηγμένο οξείδιο γραφενίου, νευρολογικές διαταραχές, Επιληψία.*

## INTRODUCTION

In every body system the brain is the organ that plays the most important role, as it configures all the functions of body and mind [1]. It consists of neurons organized in networks that communicate with each other [2] and make the brain accomplish its activities and operations. In order for the brain to perform all its activities, from the most minor to the most major, it has to be healthy [3], thus the neurons and their networks need to function properly. However, this normal function of the brain can be disrupted due to strokes, genetic conditions (tuberous sclerosis), head trauma, brain tumours or central nervous system infections [4] or even sleep deprivation. According to new studies, the last one can lead to temporary lapses that have an impact to the memory and visual perception [5]. But in more severe cases, this normal brain function can have permanent lapses, leading to neurological disorders like Epilepsy, Alzheimer or Parkinson. Patients that face such diseases suffer from repeated episodes, called seizures, with sudden, excessive and abnormal discharge of cerebral neurons.

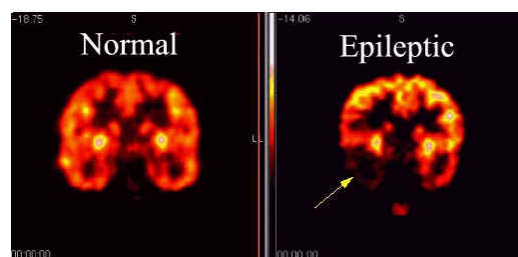


*Figure 1. Differences of a normal and an epileptic brain imaged by Magnetic Resonance Imaging (MRI)[6]*

Epilepsy is a chronic brain disorder affecting 1-2% of the world population [7]. It causes changes in the brain's electrical activity in a sudden and repeated way, with various types of symptoms. Although the symptoms of a seizure may affect any part of the body, like uncontrollable movements of arms and legs, staring blankly for a few seconds, loss of consciousness and confusion [8], the electrical events that produce the symptoms occur in the brain. For this reason, there are some important parameters, like the location and duration of a seizure, the way it spreads and the affected areas of the brain that can affect differently every patient. These factors determine the character of a seizure and its impact on the individual.

Having epilepsy, or any other neurological disorder, can definitely affect someone's life. These diseases influence patients' safety, relationships, work, driving and others as they affect the way a person behaves, moves, thinks or feels. Furthermore, having such diseases can be very costly. Just in Spain, the annual expenses for medications per epileptic person are about 1027.2 € and can reach the amount of 4936.4 € in more severe cases, where many and more expensive drugs are needed [9]. These costs do not include medical visits, diagnostic tests or hospitalizations, when, in general,

treatment can make up 30% of patients' income [9]. Thus, public perception and treatment of people with epilepsy can often be as problematic as the actual seizures [10].

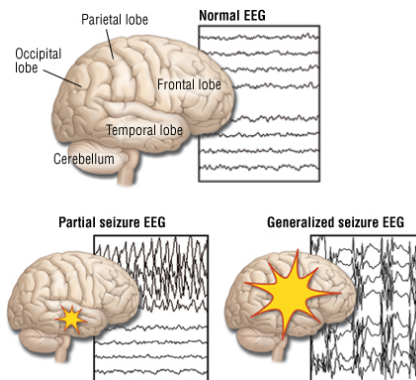


*Figure 2. Electroencephalogram (EEG) of normal and disrupted brain activity during seizures. The yellow star indicates the presence of a seizure in a random location of the brain, which can be either focal or generalized [11].*

For this reason, as it is important for the reassurance of patients' health and also widely needed for the psychological well-being of the patients among other people, there exists a tremendous need to find an effective and less expensive way to predict and control these seizures.

During the last decades, clinical doctors have tried to study the dysfunction of the brain by using electrophysiology [12] and brain imaging, such as Magnetic Resonance Imaging (MRI) [13], in order to measure the molecular activity and have an indirect view of the functions that occur into the brain of epileptic patients. For the control and treatment of epilepsy, clinical doctors prefer the oral administration by giving drugs to patients or deciding about surgeries or other invasive techniques in order to remove the brain area in which the seizure started. However, sometimes these surgeries fail or have side effects, like neurological/neuro-physiological and surgical complications [14]. On the other hand, many drugs can be toxic and therefore, do not reach the patients as they fail in pre-clinical or clinical tests [15], while the drugs that reach them, may still have undesirable secondary effects [16], especially to the healthy tissues [17,18] or the diseases can be drug resistant. Due to this, providing new and suitable drugs at the location (specific brain area) and the time (just before an incoming seizure) needed is the solution to the problem. For this reason, in recent times, scientific and medical community has focused its interest into more effective alternatives to control these disorders, like bioelectronic devices and biomolecular sensors that could be implanted in the human body.

Bioelectronics is a new field that combines electronics and biology. Scientist Luigi Galvani in 18<sup>th</sup> century was the one who gave genesis to the term of bioelectronics. He experimented with detached frog's legs to which he applied a voltage and as a result the legs moved [19]. A more recent example of bioelectronics is the creation of

the external artificial pacemaker, in 1950, by a Canadian electrical engineer named John Hopps [20].

Bioelectronic systems seem to be a promising technology for the treatment of neurological diseases as they can be implanted onto the brain, without penetrating it, which constitutes a non-invasive technique [21]. Furthermore, they are very effective as they can interact directly with the nervous system by using algorithms in order to record signals and control electrical activity [22, 23]. In that way, they can regulate the normal brain function and deal with the symptoms. Unfortunately, until recently, this was not successful; as molecular sensors used to be bulky, destroying the brain tissue and they had a short-lifetime. Furthermore, the electrodes of the sensor were made by metals, which are less transparent [24] and offer less electrical properties than the ones obtained nowadays by more effective materials, such as graphene and its derivatives. Also, depending on the quantity of the metal there is the possibility for it to be toxic [25]. Therefore, the selection of the materials utilized for such devices play a crucial role. The soft nature, flexibility, biocompatibility and mechanical properties of polymeric materials display clearly unique capabilities that match with the brain tissue flexibility and make them suitable substrates for interfacing with the brain [26]. In addition, the remarkable properties of graphene and the immense medical need to provide therapeutics, had already given rise to the first graphene-based biosensors for protein detection [27].

In this study, the goal was to create graphene-based electrodes for bioelectronic devices that improve the current state-of-the-art. More specifically, these electrodes were created by laser reduction of Graphene Oxide (GO) thin films as, besides conductivity, biocompatibility is also needed. The reduction was performed using a femtosecond laser. Femtosecond lasers are very fast lasers that reduce the thermal damage in the surrounding areas of the irradiated region and they can be controlled. Hence, laser patterning is a low-cost and a very precise and controllable technique that can also be used for more sensitive substrates like the polymeric ones. These graphene-based electrodes will be part of a biomolecular sensor for detecting glucose, lactate and glutamate, as preliminary evaluations have shown that changes in their levels assist in the prediction of seizures [28]. This biomolecular sensor will be integrated into a single device together with an electrophysiological sensor and an organic electronic ion pump and be implanted onto the brain of patients who suffer from epilepsy. Therefore, prediction and control of these seizures can pave the way for expanding the use of such device for other brain disorders as well [28].

## CHAPTER 1

# ULTRAFAST FEMTOSECOND LASER AND REDUCTION OF GRAPHENE OXIDE

### 1.1 Lasers

The term laser has its origin on the English acronym Light Amplification by Stimulated Emission of Radiation (LASER) [29], where light refers to the whole electromagnetic spectrum. Main components of lasers are the gain medium, an external source of energy and an optical cavity, which is a pair of mirrors at the two ends of the gain medium. The gain medium is used for the amplification of light, a mechanism like a pump light or a flash lamp or even a different laser is used for the activation of the medium and the optical cavity is necessary for offering optical feedback [30].

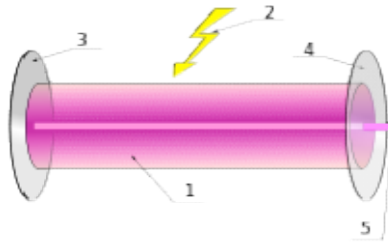


*Figure 1.1. Parts of a laser: 1. Gain medium, 2. Laser pumping energy, 3. Optical cavity, 4. Output coupler, 5. Laser beam [31]*

More precisely, the parts of a laser are [32]:

1. **Gain medium/Active material:** It can be either solid or liquid or gas or even plasma. It has certain shape, size, concentration and purity and amplifies the beam via stimulated emission.
2. **Pumping:** It activates the medium and it can be an electrical source or a flash lamp or any other laser source.
3. **Optical cavity:** It is an example of an oscillation cavity (two mirrors) that contains a beam of light between two reflecting surfaces, so that each photon passes through the gain medium at least twice before leaving the laser source outlet.
4. **Output coupler:** It is one of the two mirrors and it is transparent in some areas of its surface so that parts of the beam can escape from the cavity and form a new narrow beam.
5. **Light beam:** Spontaneous emission of light is what gives the first trigger for the activation of the gain medium. After that, the stimulated emission and the amplification in the optical cavity laser functioning takes place.

In order to achieve laser functioning, an external source transfers energy, in the form of light or electrical current, to the gain medium of the laser. The energy is absorbed by the medium exciting its atoms to higher energy levels. The average time an atom stays in an excited state is called the life time of the excited state. Depending on this life time, the atom will sooner or later decay from the upper energy level to a lower one, with a simultaneous emission of a photon. This photon has energy equal to the energy difference of the two states and thus, same wavelength with the initial photon that made the atom to carry out the opposite transition from the lower to the higher state. However, the wavelength is the only common characteristic between these two photons as the emitted photon has a completely random phase and directionality in comparison with the initial one. This type of transition with the emission of a photon with random characteristics is called spontaneous emission.

For laser operation, stimulated emission is needed, which is achieved by population inversion. When a photon of specific energy interacts with an excited atom, the atom drops to a lower level with energy difference equal to the energy of the photon. Simultaneously, as the atom decays to the lower level it emits a photon with the exact same characteristics (wavelength, phase, direction, frequency) as the photon that forced the transition. This process is called stimulated emission, as the transition does not occur spontaneously, due to the life time of the excited state, but it is forced due to the presence of a specific photon.

Population inversion occurs when the number of atoms in an excited state is higher than the number of atoms of a lower excited level or of the ground state. However, if the atoms follow the transitions governed by the life time of each excited state, population inversion will not be achieved, and therefore the laser will not function either. Hence, the atoms need to be excited to high energy levels, where fast transitions to a lower excited state will take place, so there are always a lot of remaining unoccupied positions in that higher level. The lower excited state needs to be a metastable state, so that the transitions from this lower excited state to the ground state will occur slowly. Due to the slow transitions, a large accumulation of atoms will be allowed in the lower excited state, as the probability of a spontaneous emission is relatively small. Hence, population inversion will be achieved.

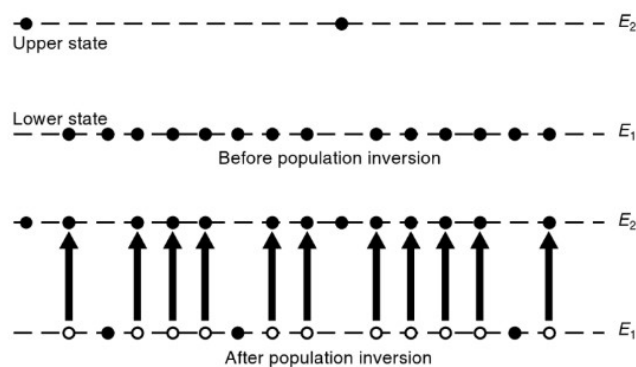


*Figure 1.2. Population inversion is needed for the achievement of laser light [33].*

When the atoms located at the metastable state are subjected to a photon with the same energy as the energy difference between the metastable state and a lower state, this photon stimulates the atoms to transit to the lower level. The consequence of this stimulated transition is the emission of photons with the same wavelength, frequency, direction and phase with the incident photon. This procedure is repeated due to the photons travelling along the axis of the gain medium between the two mirrors, resulting in generated photons with the same characteristics. Therefore, the radiation is amplified resulting in a reinforced laser beam.

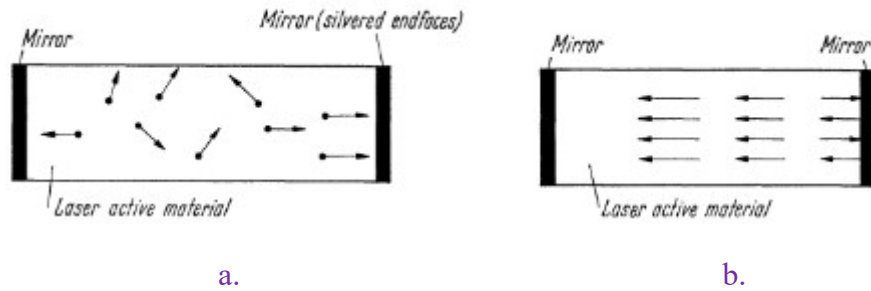


*Figure 1.3. a) Emission of photons spontaneously and b) Enhanced stimulated emission of photons traveling along the axis of the gain medium between the two mirrors [34].*

Laser light has the following very special properties [32]:

1. **Coherence:** Unlike common ordinary light sources, where atoms radiate spontaneously, without any correlation between them, in lasers all excitations are stimulated and the resulting photons are exact copies of the original photon in phase and frequency. That means that all the individual light waves corresponding to the emitted photons are in phase and produce a strong coherent electromagnetic (EM) wave.

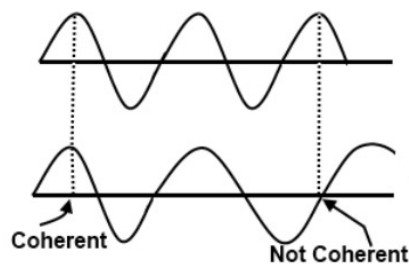


*Figure 1.4. Illustration of coherent and incoherent waves [35].*

2. **Directionality:** A direct consequence of the way the laser tube works and contrary to the properties of ordinary light, laser light has the ability of traveling for extremely long distances without spreading. The laser cavity only reinforces those of the original photons that are so aligned with their

axis that they can remain in it until they travel the full distance of the tube and reach the maximum possible intensity.

3. **Intensity:** Referring to the intensity of lasers the most important characteristic is that the light is transmitted through a very narrow range of spectrum; therefore, the intensity is much higher than in the usual light sources.
4. **Monochromaticity:** Lasers have light with a specific wavelength-color. This property has its origin on laser physics and stimulated emission. Typically, one atomic transition with a specific wavelength is responsible for the laser light. Therefore, laser light has a unique spectral color.

## 1.2 Laser Reduction

As mentioned in the introduction the aim of this study is to create electrodes with new and promising materials such as graphene and GO. Due to the fact that these electrodes will be incorporated to a molecular biosensor and then will be implanted on a human brain, materials are required to be, not just conductive, but also biocompatible and hydrophilic. Graphene is a highly conductive material, however it is also more hydrophobic than GO [36, 37]. This hydrophobicity is a consequence of the low amount of polarity in its surface charge [36, 37]. On the other hand, GO is a derivative of graphene with almost similar structure, as it also contains several hydroxyl, carboxyl, epoxy and carbonyl groups. Despite the absence of conductivity in GO, these oxygen-containing groups make it hydrophilic, due to its negative surface charge that produces electrostatic repulsion with each other [36, 38].

For biocompatibility reasons, GO is a suitable material and its reduction is the solution for recovering some conductivity as the partial removal of some functional groups can partially restore graphitic formation in monolayer. The reduced Graphene Oxide (rGO) can have superiorities over graphene as there is the possibility to control very easily the electrical conductivity, hydrophilicity and degree of reduction [39].

Reduction of GO can be performed in different ways, such as thermal, chemical, electrochemical, hydrothermal, photocatalytic treatment and laser reduction [36, 39-44]. All these approaches can produce rGO, however the efficiency and the advantages of each method are different. Thermal reduction gives great results, with high resemblance to pristine graphene. However, it is time-consuming as the reduction process can take several hours, while flexible substrates, required for the purposes of this project, cannot stand these very high temperatures [45]. Also, by thermal reduction GO disintegrates to rGO, CO and CO<sub>2</sub> gases due to its oxygen-containing groups and thus carbon atoms are removed from the GO layer as well. Hence, there is an additional deformation of the sp<sup>2</sup> carbon plane [39]. Chemical reduction typically utilizes a variety of reagents, like hydrazine, hydroiodic acid,

sodium borohydride or vitamin C [46]. Nonetheless, chemical agents are toxic for both environment and humans [40], while they can be invasive and affect negatively the substrate. Simultaneously, chemical reduction can leave behind other functional groups from the reducing agents, such as nitrogen groups, which makes it a non-pure reduction [39]. As for the other methods (electrochemical, hydrothermal and photocatalytic treatment), they are more complicated and they don't reveal such extraordinary reduction results as the previous techniques.

The last decades several laser-induced reduction methods have been reported [45, 47-49]. According to the literature, laser reduction is better than all the methods mentioned above, as it is easy and non-toxic, due to the absence of chemicals. Furthermore, its superiority is also a consequence of its remarkable reduction results, of the controllability, the low-cost and the fast repeatability (as it is not a time-consuming method) [50]. Finally, it is worth to mention that this technique is eco-friendly, as it does not require large energy consumption like in thermal reduction and it can be applied to substrates that are sensitive to high temperatures, valuable ability for the aim of this project.

Thus, laser reduction was the selected method for this thesis.

### **1.3 Ultrafast Femtosecond Laser vs. Long-pulsed and Continuous Wave Lasers**

When light interacts with matter, photon energy is transferred to the electrons and excites them to higher energy states. However, the amount of energy absorbed by the material is crucial as it is the important criterion that can lead to heating, melting or other phenomena. Pulsed and continuous wave (CW) lasers interact differently with matter and therefore, the energy transfer to each material differs as well.

In the case of pulsed lasers, laser pulse duration is an important factor for this issue. For laser material processing there are two types of laser pulse durations that are typically used. The first type is the long pulses, such as the nanosecond ones and the second type is the short or ultra-short pulses, like the femtosecond ones. For many years, researchers have performed experiments in order to find out which laser pulse is better for the laser-matter interaction. According to many scientific studies, femtosecond lasers produce better and high-precision results, while the nanosecond or in general the long-pulsed ones, create a heat-affected zone (HAZ). This is a consequence of the long duration of the pulse, which is longer than the thermalisation time of many materials [51] (usually a few picoseconds) [52, 53]. Thus, when a material is treated by a femtosecond laser, thermal effects will not be important as the

laser pulse is shorter than the time the lattice needs to absorb the energy and heating phenomena to appear.

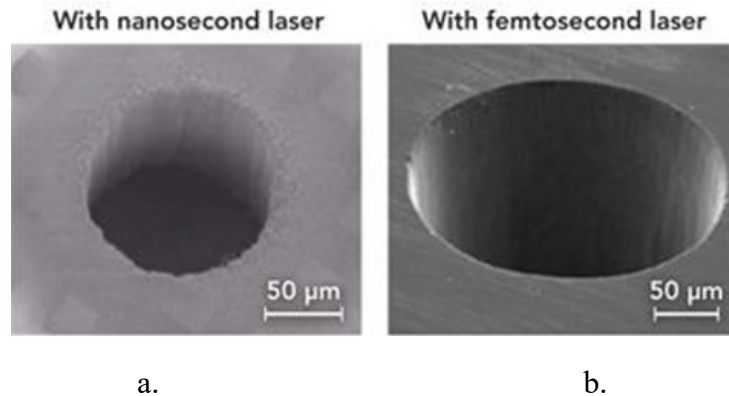


*Figure 1.5. Glass processed by a) nanosecond laser and b) femtosecond laser. The crater in the second case is uniform with minimized heating effects [51].*

Studies about film growth by nanosecond and femtosecond laser ablation displayed that, while films can be created by pulsed-laser deposition with both ways, the film produced by the femtosecond laser ablation had less stresses [52]. Kasaai *et al.* [54] mention that, in experiments on thin films and glasses with excimer and yttrium-aluminum-garnet (YAG) lasers, damage occurred via heating and melting, while the smallest crater that a nanosecond laser can create on top of glass is still larger than the one obtained by a femtosecond laser. Furthermore, their experiments resulted on expanded damage and heat-affected zones by nanosecond laser, but localized damage by the femtosecond one [54] while, in line with Zergioti *et al.* [55], ultra-short laser pulses diminish thermal effects and are suitable for microfabrication and micropatterning.

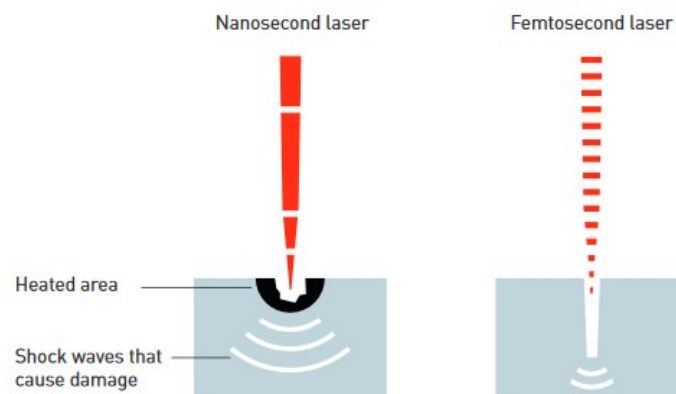


*Figure 1.6. Long-pulse laser created more heat affected areas and shock waves in comparison with the short-pulse laser [56].*

Regarding continuous wave (CW) lasers, they emit a continuous laser beam as opposed to pulsed lasers. In order to avoid generating extreme amounts of heat, they

require careful selection of parameters, such as intensity and duration of the beam; nonetheless, heat cannot be completely excluded. Several comparative studies [57-59] between CW and femtosecond lasers have taken place. In these studies, femtosecond lasers have an edge, as they provide better results with less heating in interactions with both materials and biological environments. For instance, Q. Zhang *et al.* reported changes on the non-linear refractive index of an As<sub>2</sub>S<sub>3</sub> thin film photodarkened by both CW and femtosecond laser light. The results indicated that the nonlinear refractive index had an increased efficiency of 50% when using femtosecond laser, while a decrease of its value by 60% was shown after irradiation with a CW laser [57]. In addition, Karu *et al.*, performed laser irradiation of E. coli bacteria using a femtosecond and a CW laser, in order to estimate how the light absorption triggers biochemical activity. According to their results, the modification of cells surface and their adhesive properties achieved by femtosecond laser offers only local heating and better cell attachment than the one achieved by CW laser [58]. Finally, Roy *et al.* [59] examined the sintering processing window for Cu NPs by using pulsed and CW lasers. In their paper, they stated that both types of lasers have advantages and disadvantages, however, irradiation with femtosecond laser minimizes the heat-affected zones of the sample, in contrast with the irradiation using a CW laser, where heat-diffusion in the sample is observed.

For all the reasons mentioned above, the laser used for this project is a femtosecond ultra-short pulsed laser.

## CHAPTER 2

# GRAPHENE AND GRAPHENE-BASED ELECTRODES FOR BIOSENSING

### 2.1 Graphene and Graphene Oxide: History, Background and Structure

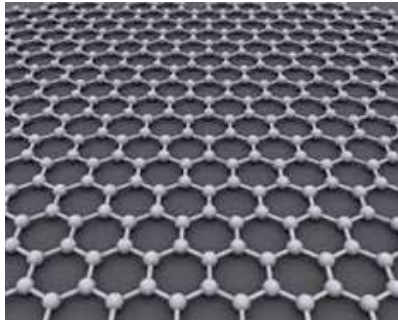
Nanomaterials are defined as the materials for which their dimensions are in the nanoscale, approximately from 1 nm to 100 nm, including both nano-objects and nanostructured materials [60]. According to studies, during the last years, the most mentioned and used nanomaterial world-wide is graphene.

Graphene, as a two-dimensional (2D) allotrope of carbon was at first thought and studied in a theoretically way for many years. However, free-standing graphene was believed not to exist [61]. Unexpectedly, the milestone year for science and technology was 2004, when Andre Geim and Konstantin Novoselov isolated a single-layer of graphite by peeling away graphite strips with adhesive tape [62]. This single atomic plane of graphite, graphene, made the scientific community focused on this material and lead to a Nobel Prize in Physics in 2010 [63]. Since its isolation as a monolayer, graphene has attracted a lot of interest due to its remarkable properties and its potential application in various scientific fields, such as supercapacitors, biosensors, organic photovoltaics etc [64].

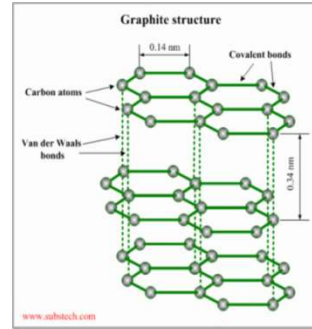


*Figure 2.1. Andre Geim and Konstantin Novoselov are the two scientists awarded the Nobel prize in Physics in 2010 "for groundbreaking experiments regarding the two-dimensional material graphene" [65].*

**Graphene** is an allotrope of carbon that forms a hexagonal lattice in two dimensions, in which an atom is at each top of the lattice. Each carbon atom has a distance of  $a = 1.42 \text{ \AA}$  from its neighbors with whom it shares a  $\sigma$  bond, while it also shares a fourth  $\pi$  bond with another neighbor, which is oriented in the z-direction, e.g. outside the plane. It is the basic building block of other allotropes such as graphite, fullerenes and carbon nanotubes [61], while it has many unusual properties. It has more strength than any other material even if it is not as heavy or bulky, it is almost transparent (97.7%) [66] and conducts heat efficiently. However, electrical conductivity is one of its most popular properties as it is used mostly in electronic applications.



a.



b.

*Figure 2.2. a. Structure of graphene: Monolayer of carbons that are tightly packed into a honeycomb lattice [67] and b. Intralayer and interlayer distances between C-C atoms in the hexagonal crystalline structure of graphite [68].*

Graphene is a very conductive material. The conductivity of a material depends on the energy gap between valence and conduction band. When these bands are very close to each other and the energy gap between them is very small, the excited electrons, due to heating or voltage application, can easily transit from the valence band to the conduction band, resulting into electrical current. If the energy gap between the energy zones is too large, then the electrons will not have the required energy to make the transition and thus, there will be no conduction (insulators). Graphene presents an uncommon behavior: its energy bands form two cones (Dirac cones), connected to each other at their extremities (edges) in two inequivalent points (K and K'), which are called Dirac points [61]. Hence, valence and conduction band degenerate and make graphene a zero-band gap semiconductor [61]. As there is no gap between the bands, graphene electrons can be easily transferred from the lower band to the upper band and vice versa, without requiring much more energy, resulting in graphene's high charge carrier mobility and high conductivity.

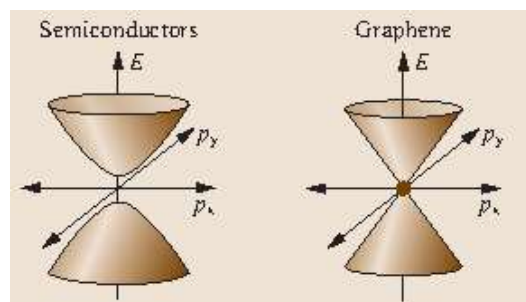


*Figure 2.3. The band structure of semiconducting materials (left) indicating the presence of a band gap between the parabolic valence and conduction bands and the band structure of graphene (right) indicating that the two Dirac cones, representing the energy bands, meet at the Dirac point [69].*

Due to all the incredible properties mentioned above and as graphene is considered as an exciting material and an impressive discovery [70], it has deservedly won the title of "miracle material".

The term graphene was recommended by the IUPAC (International Union of Pure and Applied Chemistry) commission in order to name the 2D layers of graphite, which is a 3D structure [71]. As a result, graphene refers to a 2D monolayer of carbon atoms and it is considered as the "mother" of graphitic materials.

Graphene oxide has a similar structure with graphene but it is also a different case. When graphite is oxidized, oxygenated functional groups are introduced in its structure. This offers not only an extension for the separation of the layers of the bulk oxidized graphite, but it also makes it hydrophilic. Hydrophilicity permits to oxidized graphite to be sonicated in ultrasonic water and to produce monolayers or few-layers of GO. Thus, graphite oxide is the bulk material, while the decrease in the number of sheets to some or only one layer gives GO.

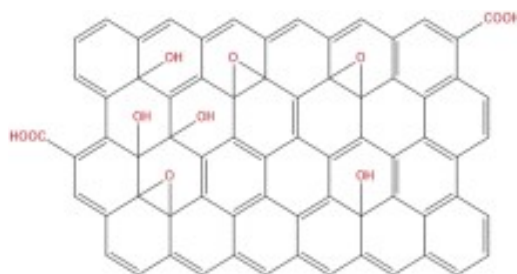


*Figure 2.4. Molecular structure of GO [72].*

## 2.2 Graphene Properties

The mechanical, electrical, thermal and optical responses of graphene and its derivatives are those that make it differ from other materials.

1. *Physical/Mechanical properties:* Graphene has the thickness of one atom ( $\approx 0.335$  nm) and it has a high surface area of  $2630$  m<sup>2</sup>/g. [73]. It has a strength of  $42$  N/m and it is 100 times stronger than steel, while it has a high stretch ability, up to 25%, which makes it a suitable candidate for flexible electronics [74, 75]. Moreover, a graphene sheet has stiffness similar to diamond with a value of Young modulus of about 1 TPa, while it can function as a barrier as it does not permit to be penetrated, not even from the smallest atom (helium).
2. *Electrical properties:* As it was mentioned above, the remarkable properties of graphene have their origin in its extended  $\pi$ - $\pi$  conjugation [76]. Graphene is the known material with the highest mobility ever discovered at about  $200,000$  cm<sup>2</sup>\*V<sup>-1</sup>\*s<sup>-1</sup>, which is 100 times higher than that of silicon [77]. However, scientific works of the last decades have shown that the mobility of graphene can even reach the value of  $230,000$  cm<sup>2</sup>\*V<sup>-1</sup>\*s<sup>-1</sup>, by annealing their samples

[78]. Furthermore, graphene has a very low electrical resistivity at room temperature (even lower than the copper) [77] and it is very conductive, which is a consequence of its structure, as the two conical energy bands of graphene connect to each other at their edges at the Dirac point. Its resistivity is about  $1 \cdot 10^{-8} \Omega \cdot m$  and its conductivity is related to its quality. This means that if graphene has not many defects it will be a better conductor. Pristine graphene is free from defects [61].

3. *Thermal properties*: Graphene is an isotropic conductor as it provides heat to all the directions. It is considered the most perfect conductor of heat, as the values of its thermal conductivity can exceed the ones of graphite, carbon nanotubes or diamond of the same size. According to literature, the value of thermal conductivity that corresponds to graphene is over 5,000 W/m/K [70].
4. *Optical properties*: Graphene is nearly transparent as it absorbs approximately 2.6% of green light [79] and in general an important fraction of white light ( $A = (1-T) = \pi\alpha \approx 2.3\%$ ) [80], where A is absorbance, T is transmittance,  $\pi$  equals to 3.14 and  $\alpha$ , is the fine-structure constant. This property makes graphene better than Indium Tin Oxide (ITO) [81] which is less transparent than graphene.
5. *Chemical properties*: Graphene is a material where its atoms usually do not react with other atoms, however it has the ability to absorb other atoms and molecules. This can lead to changes in its properties and to various applications. In addition, as it contains some surface-active functional moieties it is suitable for functionalization by many chemical groups. Characteristic examples are the functionalization of graphene with oxygen [82] or fluorine, resulting graphene oxide and fluorinated graphene, respectively.

### 2.3 Graphene and Graphene-Based Materials' Applications

As graphene is considered to be the magic material, it appears with many and promising applications almost in every field. In addition, its derivatives, such as rGO, can be used in the same ubiquitous applications due to the similarity in their structure and properties. These various applications are displayed in Figure 2.3 and are described better in the following lines [70]:

1. *Electronics*: Graphene and its composites can be used in optoelectronic, nanoelectronic and bioelectronic devices, as transistors or in general as flexible devices due to their structure and electronic properties.
2. *Sensors*: Graphene and Graphene-Based Materials are suitable for use as various kinds of sensors as each of their atoms is exposed to its environment. Therefore, they can be used as biomarker detectors (biosensors), gas sensors, explosive detectors and environmental monitors.

3. Composites and Coatings: Mechanical properties of graphene in combination with its low mass and load make graphene-based materials suitable for thin films, protectors and coatings for various devices.

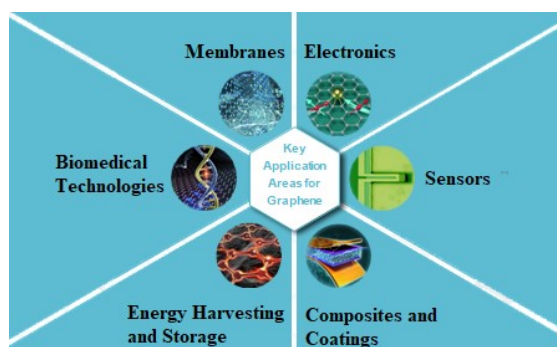


*Figure 2.5. Schematic representation of the variety of fields where graphene and graphene-based materials are applicable [83]*

4. Energy Harvesting and Storage: Graphene improves energy capacity and charge rates, that's why all graphene-based nanomaterials can be used as batteries, solar cells, supercapacitors etc.
5. Biomedical Technologies: Graphene-based materials like rGO can be used as biomaterials, biosensors and in general in the fields of bioelectronics and bioionics, bioimaging and targeted drug delivery. This ability is due to many of their properties, such as electron mobility, functionalization potential and hydrophilicity (rGO).
6. Membranes: Doping graphene with other materials can create the desired defects which will be used as transport mean for gas and liquids against graphene's impermeability. Thus, graphene-based materials can be used as membranes for water cleaning or as gas barriers in food packaging.

## 2.4 Graphene-Based Electrodes

Electrodes are conductors that let the current pass from one side to another or in general from one medium to another. Usually, the most common materials used as electrodes in the past decades were metals and their oxides. Especially Indium doped Tin Oxide (ITO) was the promising material for the production of sensors, solar cells, polymer-based electronics, Light Emission Diodes (LEDs), Field-Effect Transistors (FETs), photovoltaics, and other optoelectronic devices [84].

ITO was used as an electrode material due to its conductivity and transparency; however, it also has several important drawbacks. It is found rarely in nature and it is expensive, while it is also brittle, thus it can crack under low strains [85]. Therefore, its use in flexible electronics is very limited. Furthermore, its deposition has to take place in strict conditions [84] and it is very toxic for use in bioelectronic devices.

People exposed to ITO were found to have respiratory problems, pneumoconiosis, pulmonary fibrosis, granulomas etc. [86], while animals that ingested it for experimental purposes, had irritations and problems with many organs such as lung, heart and kidney [87]. Due to all the previous issues, the use of alternative materials with same properties as ITO, but without its disadvantages, was of great importance.

Such a possibility opened by doped compounds such as aluminium zinc-oxide (AZO), carbon nanotubes (CNTs), conductive polymers like poly(3,4-ethylenedioxythiophene) poly(styrenesulfonate) (PEDOT:PSS) and metallic nanowires [85]. PEDOT:PSS has higher sheet resistance than ITO, but is more flexible, eco-friendly and low-cost [88]. In addition, CNTs, metal nanowires and doped compounds are more conductive than ITO [89] and they can complement the requirements associated with it. Even if there were concerns about their rough surface [45], their use remained high enough. Especially in electrochemistry, carbon based materials such as carbon nanofibers, CNTs and fullerenes are commonly employed as electrodes [84]. Nonetheless, the vast majority of the alternatives mentioned above can be utilized in optoelectronic devices, but not in bioelectronic ones, as doped compounds, fullerenes and mostly CNTs and carbon nanofibers are potentially risky for health [90, 91]. According to Monteiro-Riviere, N.A *et al.* [92] and to Lam, C. *et al.* [93] these materials can possibly lead to skin irritation, inflammation and toxicological lung changes, regardless of their synthesis method.

Graphene, as the base from which carbon materials are derived has similar, if not better, properties. Thus, in combination with functionalization possibilities that make it even more biocompatible, such as GO, it paves the way for the new generation of electrodes of the last decade.

There are four ways to produce graphene-based electrodes [84]:

1. Pristine graphene
2. Chemical Vapor Deposition (CVD) method
3. Chemical Modification of graphene (GO and its reduction)
4. Graphene composites (eg. Graphene-metal nanoparticles electrodes)

In this work the third method is used, as GO is altered to rGO, by using laser irradiation.

## **2.5 Biosensors and Graphene**

### **2.5.1 Biosensors**

Biosensing is a very charming and up-coming field as it is interdisciplinary. It contains a variety of scientific domains, such as electronics and photonics, biology

and also chemical analysis for the monitoring of the occurred phenomena. Thus, a biosensor is a device of a physicochemical detector in combination with biological systems that can provide identification of changes in chemical substances [94]. Such definition could definitely comprise microelectrodes implanted in tissues, such as brain, so the detection of enzymes and biomolecules can be achieved.

The first real biosensor was created in 1956 by Leland C. Clark in order to detect oxygen, and that oxygen electrode was named 'Clark electrode' after him [95]. In 1962 Clark and Lyons, knowing that glucose can be oxidized in an enzymatic way to hydrogen peroxide ( $H_2O_2$ ), which could be electrochemically monitored, they used the Clark amperometric electrode as transducer and in combination with the enzyme glucose oxidase for sensing, they managed to have the first glucose monitoring [94].

In biosensing, receptors and transducers are very important as they are the recognition components and the measuring system, respectively. The receptors interact with analytes and the products of their interactions are measured by the transducers. The bioreceptors can be either enzymes or cells or nucleic acid and DNA [96], or antibody and antigens [97]. Transducers can be electrochemical, optical, electronic, piezoelectronic or other type of biosensors [98].

In this project, the goal is to create graphene-based electrodes for a graphene-based biomolecular sensor for glucose detection. Therefore, the receptors of the biosensors will be enzymes and the biotransducer will be an electrochemical biosensor. Electrochemical biosensors rely on enzymatic interactions that usually produce electrons. In this case (glucose monitoring), glucose reacts with glucose oxidase (GOx) enzyme catalyst and produce  $H_2O_2$ . The latter one reacts with the electrodes by redox reactions, resulting in negative charge carriers (electrons). The concentration of the charge of the chemical reaction depends on the amount of  $H_2O_2$  and these electrons cause the current flow, thus the detection by the electrochemical sensor [99, 100].

### **2.5.2 Graphene-based Biosensors**

During previous decades, metals, metal oxides, semiconductors, metal nanoparticles (NPs), CNTs, nanowires etc were used for the construction and enhancement of sensors and biosensors [101]. After the isolation of graphene from bulk graphite and the exploration of its properties, the field of sensors could not, but, be affected from this new discovery.

Due to its flexibility, large surface area, atomic thickness, high electron transfer rate and conductivity, graphene became a must material for the domain. Especially its structural properties (one-atom thickness and high surface-to-volume area), make it

extremely sensitive to locally changing conditions [102]. In addition, due to its electrochemical properties (high electron transfer), graphene and its derivatives, such as rGO, are utilized for electrochemical sensing, as they can serve as a direct electrical connection between the enzymes and the electrodes [101]. Among other reasons, rGO is utilized in graphene-based sensors, due to the chemical moieties and functional groups in its surface that offer higher biocompatibility and a functionalization possibility that provides advantages to the sensors [101].

Graphene can be typically functionalized with biomolecules for structural modification, with polymers for high conductivity and strength and with nanoparticles that enhance thermal stability, graphene's conductivity and the sensor's analytical response [102]. For electrochemical sensors and particularly for glucose monitoring, such kind of functionalizations take place, as it is proved that such nanocomposites improve the characteristics of each component separately [103]. Luo *et al.* [104] proposed an electrochemical sensor that relies on the combination of glassy carbon electrode (GCE) with metal NPs and graphene for glucose. The results showed more advanced characteristics of this sensor than a sensor without graphene and copper NPs. Similar conclusions were shown by Shi *et al.* [105], which, by using platinum (Pt) NPs with GO achieved to boost the electrocatalytic activity of the sensor up to 12 times. This is a consequence of the fact that Pt NPs on graphene-based surfaces can improve the detection signal [99], however this is a fact for all the metallic NPs. For example, Xue *et al.* [106] managed to improve the sensitivity and the electron transfer of the sensing system by incorporating conducting polymers and gold (Au) NPs into a rGO-based glucose biosensor. Furthermore, such nanocomposites can be promising for the fabrication of multilateral electrochemical biosensors by encapsulating biomolecules [102].

In general, combining graphene and its derivatives with polymers [107, 108] and metal NPs in biosensors, can improve dramatically the sensitivity, reproducibility and limit of detection [109]. Nonetheless, all these electrochemical biosensors for glucose monitoring with all the functionalizations mentioned above are typically used as a needle-free approach for diabetic patients. Therefore, the limitations that can face are extremely different with those associated with neurological disorders. For example, dealing with the extraction and detection of glucose through skin or hair follicles has not the same difficulties as the detection of glucose from a sensor implanted on brain tissues. In addition, the proper selection of the materials from which the biosensor will be composed of is crucial. For instance, metal NPs can enhance the electrical properties of the sensor; however when such a device is planned to be incorporated with such parts of the human body, the risks (eg. aggregations, large concentrations of NPs that could possibly be toxic or NPs dissolved or transferred through body fluids to healthy organs and cause inflammations) may overcome the advantages.

The most complex problem in disorders of the central nervous system (CNS) is that the drugs have to pass through the blood-brain barrier (BBB), before approaching their targets inside the brain [110]. Thus, many drugs end up in the blood flow

without having the opportunity to take action in the targeted area of the nervous system. Moreover, microfluidic systems, which typically are used for drug delivery, utilize solvents, facilitating the dissolution and spread of the drugs at different locations of the central nervous system. This spread can lead to deleterious side effects in healthy tissues or organs [111]. A solution to this issue was thought at first to be the use of optogenetics, a method that can intervene locally exactly at the time it is needed and it can be used for controlling epilepsy [112]. Nevertheless, this technique has still limitations in its 'transfer' to a clinical setting [113].

Williamson, A. *et al.* [114] proposed the use of an organic electronic ion pump (OEIP) for drug delivery in brain tissues in order to control the epileptic activity. Due to the field of organic (bio)electronics, organic materials are suitable candidates for interfacing with the brain. Their compatibility with soft and flexible substrates, like the brain's curvy surface make organic electronics long-last materials for use, while their nature matches brain's mechanical properties [115]. Suitable OEIPs for neuroscience engineering are based on stacked layers of anion- and cation-exchange membranes that form ion diodes and can add ions and charged biomolecules for stimulation and signaling of the neurons [114]. According to Williamson's *et al.* results, by delivering locally gamma-aminobutyric acid (GABA), which is a neurotransmitter, they managed to vanish abnormal neurological activity. Furthermore, they stated that this method could be used in clinic for patients who cannot undergo surgery, by integrating the pumps with the electrodes for long-lasting brain stimulated activity [114].

For this reason, in the project an OEIP will be used for delivery of neurotransmitters through an ion-exchange membrane of selective permeability [116]. This OEIP will lead to beyond the state of the art results, not only due to the drugs that will act at the specific time and the location needed, but also as it will deliver the drug without a solvent, making possible the targeted drug delivery using larger amounts of drug . Furthermore, the properties of organic electronics can be also useful for the brain recordings by the electrophysiological sensor fabricated for this project. Conjugative polymers are organic electronic materials, as they have a very high conductivity due to the existing p orbitals with  $\pi$  delocalized electrons in their structure. Their high mixed electronic/ionic conductivity leads to low impedance in the biotic/abiotic interface, resulting in richer recordings. Such a "signal amplification" allows to record brain signals from the surface of the brain, without any penetration. The fabrication of a device that will be less invasive, without penetrating the brain, is a breakthrough in the field.

Finally, the electrophysiological sensor, the biomolecular sensor- for which the graphene-based electrodes are developed- and the OEIP, will be incorporated into a single device for the prediction and control of epileptic seizures. However, it's worth mentioning that the creation of the OEIP and of the electrophysiological sensor is out of the scope of this master thesis, as the main purpose of this study is the fabrication of graphene-based electrodes.

## CHAPTER 3

### CHARACTERIZATION TECHNIQUES

#### 3.1 Ultra-violet Visible Infrared Spectroscopy (UV-Vis)

Ultra-violet visible infrared spectroscopy uses light in the visible and the adjacent near infrared and near ultraviolet regions. For practical reasons, the spectrum is divided in the following regions:

- A) Far ultraviolet (far UV) area below 200 nm
- B) The near UV range between 200 and 400 nm
- C) The visible area between 400 and 750 nm and
- D) The near Infrared (NIR) region between 750 and 2500 nm

In these wavelengths, when light interacts with materials, electronic transitions occur by materials' atoms and molecules. The transitions take place from the ground state to the excited states [117], which are higher energy levels, due to the absorption of the energy gained by the light irradiation. The easier the electrons are excited (thus, the energy gap is lower between Higher Occupied Molecular Orbital (HOMO) and Lowest Unoccupied Molecular Orbital (LUMO), the greater the wavelength of light they can absorb [118]. That means that it is the outer electrons that by lifting or falling from one orbit to another cause energy to be absorbed in discrete quantities.

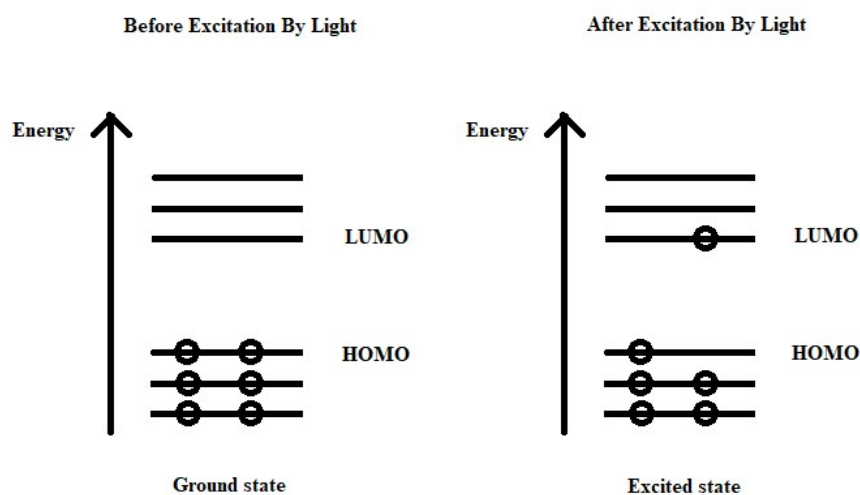


*Figure 3.1. Representation of transitions from the ground (HOMO) to the excited (LUMO) state.*

More specifically, electrons can exist in these conditions: either  $\sigma$  (sigma) in localized bonds with lower transition probabilities, or  $\pi$  (pi) with higher transition probabilities.

Chemical bonds can be created by atomic orbitals that overlap to each other and make either bonding molecular orbitals (low energy), or anti-bonding molecular orbitals (high energy) or non-bonding ones [119, 120]. The bonding ones are the  $\sigma$  and  $\pi$  and their corresponding anti-bonding ones are the  $\sigma^*$  and  $\pi^*$ . The non-bonding electrons,

n, have no corresponding anti-bonding orbitals [119], as they cannot create bonds [120]. The molecular orbitals with the lowest energies are  $\sigma$  orbitals, while the ones with higher energies are non-bonding n and  $\pi$ . Finally, the orbitals with the highest energy levels are the anti-bonding  $\pi^*$  and  $\sigma^*$  ones [119]. When a material is irradiated, electronic transitions from an occupied molecular orbital (that is mostly a non-bonding n or bonding  $\pi$  orbital) to an unoccupied molecular orbital (anti-bonding  $\pi^*$  or  $\sigma^*$  orbital) occur [119].

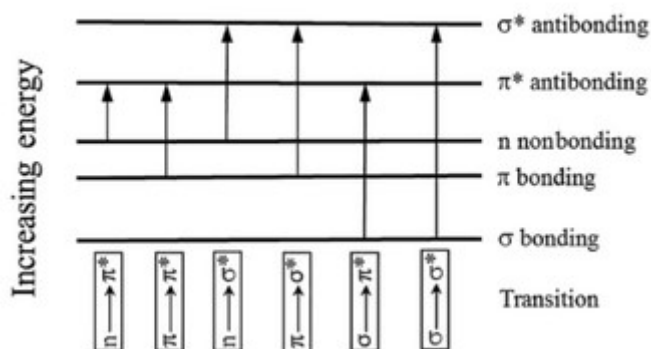


*Figure 3.2. Representation of the permitted electronic transitions from bonding and non-bonding molecular orbitals to the anti-bonding orbitals [119].*

The permitted electronic transitions in absorption are shown in Figure 3.2. The bonding  $\sigma$  and the non-bonding n to anti-bonding  $\sigma^*$  transitions need higher energies, thus they are correlated with ultraviolet irradiation and shorter wavelengths. The non-bonding n and the bonding  $\pi$  to anti-bonding  $\pi^*$  transitions need lower energy to occur, that's why they are correlated with wavelengths in ultraviolet and visible irradiation [119].

A typical UV-Vis spectrometer is observed in figure 3.3:

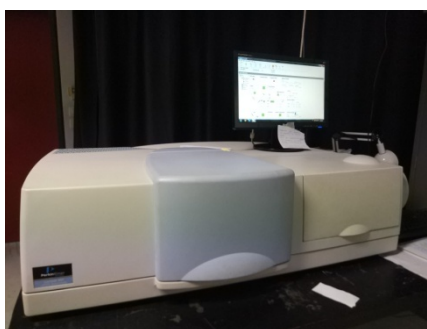


*Figure 3.3. A typical UV-Vis spectrometer. This spectrometer was used for the acquisition of the UV-Vis spectra of this work.*

In order to take the absorption spectra of substances in solutions, the most effective way is by using the Beer-Lambert law [118]:

$$A = \log_{10}(I_0/I) = \epsilon cL,$$

Where  $A$  is the absorbance measured in arbitrary units (a.u.),  $I_0$  is the initial intensity at a specific wavelength and  $I$  is the transmitted intensity,  $c$  is the concentration of the absorbing substance and  $L$  is the path length through the sample. The  $\epsilon$  factor is a constant for every material and wavelength, known as molar extinction coefficient. This factor shows how strong is a species' absorbance of light at a specific wavelength per molar concentration. Beer-Lambert law is very useful in order to find the absorption of many compounds, however is not suitable for all substances.

For the solid species it is better to measure their reflectance and transmittance and then calculate the absorbance as a percentage according to the equation below:

$$A = 100 - R - T,$$

Where  $A$  is the absorbance (%),  $R$  is the measured reflectance and  $T$  is the measured transmittance.

### 3.2 Raman Spectroscopy

Raman Spectroscopy, took its name by an Indian physicist called Raman, who was the first one that observed the phenomenon in 1928 [121]. Raman used sunlight, monochromatic light created by a narrow-band photographic filter and a monochromatic light blocker which was a "crossed filter". He found that a small amount of light had changed frequency and passed through the "crossed" filter [122], a discovery that led him to win the Nobel Prize in Physics in 1930.

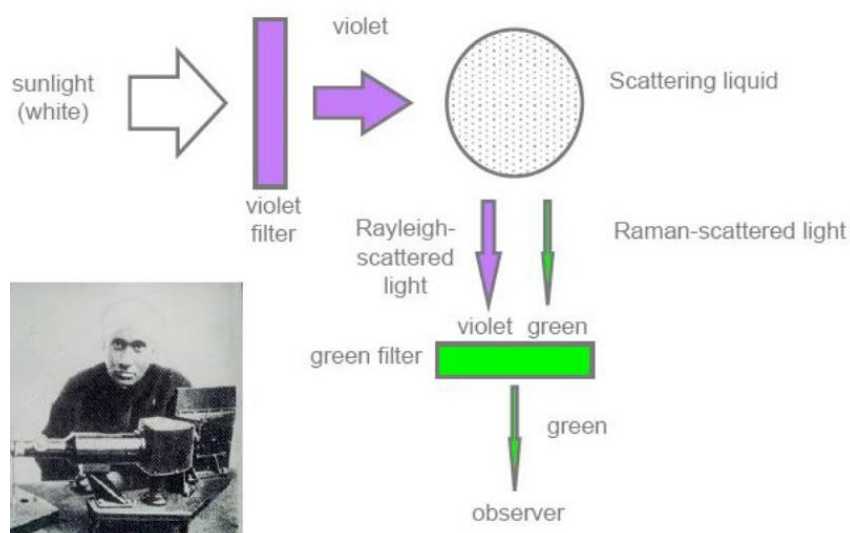


*Figure 3.4. Raman Experiment [123]*

Raman spectroscopy is used as a structural fingerprint as it can identify each molecule by the observation of the vibrational, rotational and any other low-frequency modes

[121]. The interaction of the laser light with matter results in the shifting, either up or down, of the laser photons' energy.

A laser beam is illuminating a sample and a lens is used to collect the irradiation from the illuminated spot and send it through a monochromator. Notch filters, edge pass filters or band pass filters filter out the elastic scattered radiation at the specific wavelength that corresponds to the laser line (Rayleigh scattering). The rest of the light is collected onto a detector, usually a Charge-coupled device (CCD). In the end a computer is used for data collection and curve fitting [124,125].

More specifically [124,125]:

Excitation source: It is usually a laser that produces input rays

Beam expander: Optical devices that may exist in the set up for expanding the size of the beam.

Rayleigh filters: They are placed in the Raman beam path and are used to selectively block the laser line (Rayleigh scatter) from the Raman scattered light through to the spectrometer and detector in order to obtain higher quality Raman spectrum.

Focusing optics: They are usually mirrors that focus the input and output light to Rayleigh filter.

Diffraction Grating: It has the ability of splitting a light beam into many beams that are driven in different directions.

Detector: The detectors are usually CCD cameras for UV, visible and near-infrared light.

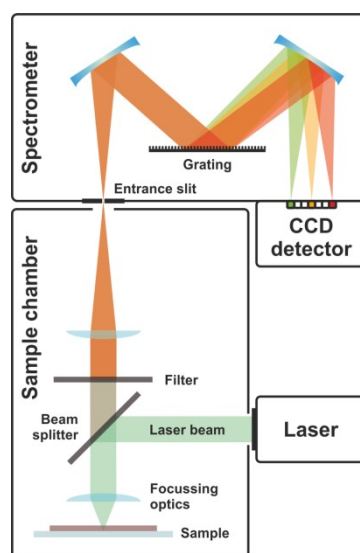


*Figure 3.5: Typical Raman spectrometer [126]*

It relies on the scattering effect of light. If a monochromatic radiation beam is used, then the scattered frequency is very similar to the one of the incident radiation beam (Rayleigh diffusion), but part of it consists of some distinct frequencies above and below the initial frequency. Spectral lines whose frequency is lower than the one of the incident beam are called Stokes lines and they are due to the collision of photons with molecules in the ground state. On the other hand, spectral lines whose frequency is higher than that of the incident beam are called anti-Stokes lines and they exist due to the collision of photons with molecules in the excited states [117, 127]. In this second case, the surplus energy is transferred to photons as the molecules return in their initial ground energy state.

Due to the equation  $E = hf$ , energy has the same behavior with the frequency. This means that if a photon (electromagnetic radiation of a particular wavelength) collides with a molecule, it will excite it either in its ground vibrational state or in its excited vibrational state. Thus, the molecule is located in a virtual energy level for a very short period of time. When it returns to its initial state a photon is emitted. This photon can be of lower energy (Stokes) or higher energy (anti-Stokes) than the incoming photon.

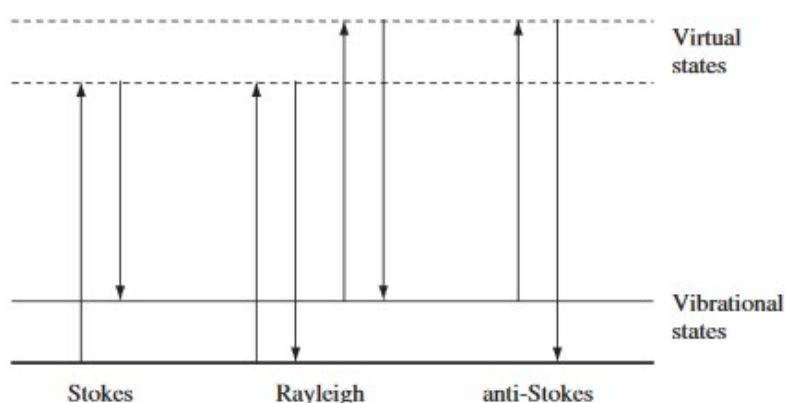


*Figure 3.6. Representation of the transitions for Rayleigh, Stokes and anti-Stokes scattering [128].*

According to the figure 3.6, maintaining of photon energy gives Rayleigh elastic scattering. If energy is not maintained, scattering is called inelastic Raman. In the Stokes area, the molecule returns to a higher energy level than the one it started, so the scattered photon loses energy and scatters at lower frequency than the initial one ( $\nu_0 - \nu_i$ ). In the anti-Stokes area, the molecule moves to a lower energy level than the one it started, so it gains energy and it scatters at a higher frequency than the incident ( $\nu_0 + \nu_i$ ).

Quantum mechanics describes the energy exchange when an inelastic collision occurs between a photon and a molecule. In that case the molecules will gain or lose energy, so that their final energy will be different from the initial one. Therefore, the wavelength of the incident beam is the base of Raman scattering, as the whole

phenomenon relies on it [129]. The energy difference,  $\Delta E$ , between two permitted states represents changes in the vibrational and / or rotational energy of the molecule. In the case of the Raman phenomenon, the changes of quantum energy are due to the ability of an atom or molecule to separate the positive and negative charge centers when it is affected by an electric field. This ability is called polarizability of the chemical molecule.

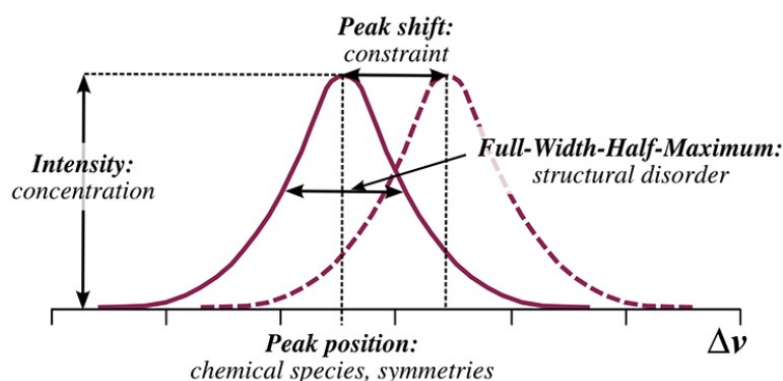


*Figure 3.7. Representation of the qualitative and quantitative information obtained by Raman spectra [130].*

As shown in Figure 3.7, a Raman spectrum can offer a lot of quantitative and qualitative information about the material under study [130]. The peaks of the spectrum correspond to vibrations of existing chemical bonds in the material, while a wider peak called Raman band, corresponds to several overlapping peaks originated from the same chemical bond but with slightly different surroundings. Therefore, by the peaks and their position the identification of each bond occurs (fingerprint of the molecules). Finally, the intensity of each peak is related to the concentration of the sample, while the Full Width at Half Maximum (FWHM) is a characteristic of structural ordering in the specimen.

In this study, the characterization of GO and rGO films took place using a Raman spectrometer at 473 nm wavelength. This wavelength was selected as it can provide a better relation between the  $sp^2$  and  $sp^3$  sites before and after the reduction of GO. According to Ferrari *et al.* [131], visible Raman spectroscopy allows the detection of the  $sp^2$  bonding, while UV Raman spectroscopy is sensitive to both  $sp^2$  and  $sp^3$  sites. As the Raman instrument that was in our disposal could use different wavelengths, with the lowest one and closer to UV region the one of 473 nm, it was decided that this wavelength will be utilized. Finally, the intensity ratios and the FWHM of the Raman bands were calculated using Lorentzian fitting. According to Ferrari *et al.* [131], especially for the intensity ratio of D and G band, Lorentzian fitting reports peak height ratios, while Gaussian fitting reports peak area ratios. The difference is not important in case the utilized material is disordered graphite, but it is important when the utilized material is amorphous carbon, as in the case of this study. Hence, as the information about the disordered aromatic rings depends on the height of the peak, Lorentzian was the most suitable fitting.

### 3.3 Fourier Transform Infrared Spectroscopy-Attenuated Total Reflectance (FTIR-ATR)

Infrared spectroscopy (Infra-Red, IR) is one of the fundamental techniques for characterizing materials. The information provided by this spectroscopy is about the chemical bonds of a substance and their nature and in general about the quality and quantity of various functional groups such as OH, C = O, NH<sub>2</sub>, COOH, CN, etc. Thus, in case of destruction of existent bonds or creation of new ones or in case of any other changes in the concentration of a substance, FTIR spectroscopy is able to give all the information concerning the alterations of the structure of different materials. It is often called the fingerprint technique because, exactly as a fingerprint, there are no two unique molecular structures with the same infrared spectrum.

FTIR offers accurate and reproducible measurements. This is due to its numerous advantages. Some of them are the high speed (all frequencies measured simultaneously, reducing the required time to mere seconds), the high sensitivity and the low noise in the output images, while this technique offers rich information and it is almost universal [132]. This makes FTIR a very reliable technique both for quality and quantity analysis.

The procedure followed for the infrared spectroscopy is described in the next lines:

When a light source irradiates a substance, its molecules absorb the energy from the irradiation, which affects the bonds of the molecules that start to oscillate in different ways. Afterwards, a diagram of the intensity-wave number is recorded, which is called the infrared spectrum. Infrared spectra can be captured either as transmittance (T) or absorbance (A) spectra. The wave number (or inverse wavelength in cm<sup>-1</sup>) is plotted in the horizontal axis, while in the vertical axis is plotted as transmittance or absorbance the amount of radiation that reaches the detector through the sample.

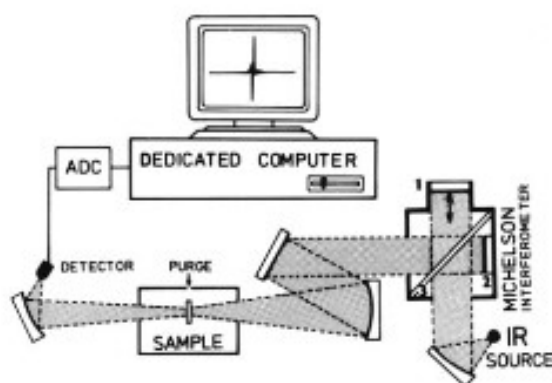


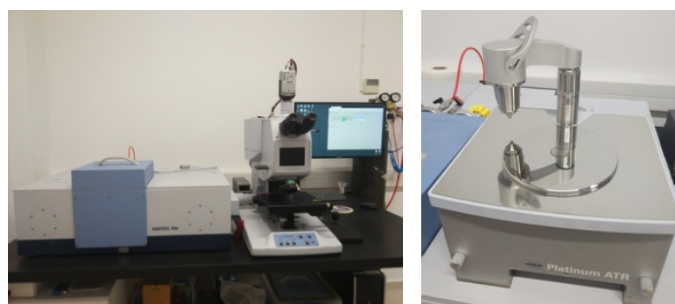
*Figure 3.8. FTIR spectrometer set up, where the interferogram with the use of computer is Fourier transformed in a typical IR spectrum [133].*

Transmittance (T) represents the fraction of the intensity of radiation that passed through the sample and reached the detector (called I), to the total intensity that

reached the sample (called  $I_0$ ). Thus,  $T=I/I_0$ . On the other hand, absorbance (A) represents the intensity of the radiation absorbed by the sample which is correlated with Transmittance as  $A = -\log T$ . So, even if Transmittance and Absorbance express opposite phenomena, they are not linear but logarithmic to each other [132].

In this work an FTIR instrument equipped with a A225/Q Platinum ATR unit with single reflection diamond crystal was used. This unit with the diamond crystal allows the infrared analysis of unevenly shaped solid samples and liquids through total reflection measurements. The FTIR-ATR instrument offers advantages in comparison with the traditional FTIR transmittance tool, such as the ability to measure samples in gas or liquid state without the need of any preparation, while specimens that are not transparent to IR irradiation can be easily measured as well.

In this study, the measurements are not performed in a transmittance mode, due to the glass substrate which is transparent in visible, but not in the IR range. For this reason, the reflection mode was used, in which a set of rays originated from all the directions strikes the sample and a set of reflected rays from all the directions are received in the detector. Thus, the resulting spectrum offers information about the sample's absorbance and therefore, the spectra received from the FTIR-ATR spectroscopy are absorbance spectra. In order to compare the resulting spectra with the literature, in which the majority of them are taken in the transmittance mode, the fingerprint of the vibration of each molecule can be utilized, as the wavenumber is the same both in absorbance and in transmittance spectrum, but appearing as a peak in the former and as a valley in the latter.



a.

b.

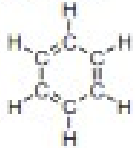
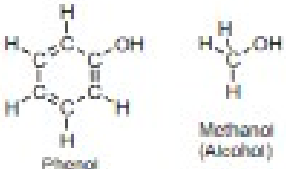
*Figure 3.9. The ATR-FTIR spectrometer used for the experiments of this study.*

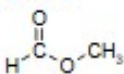
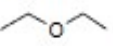
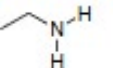
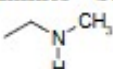
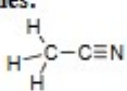
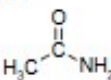
In an FTIR spectrum two large absorption families can be differentiated. The first family is in the  $4000-1300\text{ cm}^{-1}$  region, denominated as the characteristic group frequency region. In it, vibrations are usually of the stretching type and each peak demonstrates the presence of the corresponding moiety in the compound. The second family, located in  $1300-400\text{ cm}^{-1}$ , known as the fingerprint region, consists of a complex combination of peaks, usually of skeletal vibration type. In this area, vibrations can be bending, torsion etc.

Organic compounds are identified through FTIR spectrum which displays the existence of bonds such as: C-H (found in almost all organic compounds), C=O

(found in carboxylic acids, esters, ketones, aldehydes), C=C, C-C, O-H (found in alcohols, carboxylic acids) etc.

Table 3.1. Principal FTIR absorptions for some functional groups [134].

<b>Functional Group Names &amp; Example compounds</b>	<b>Absorption Ranges(<math>\text{cm}^{-1}</math>)</b> <small>[Look for a single absorption in these regions, unless stated otherwise.]</small>	<b>Type of Vibration causing IR absorption</b>
<b>Alkanes:</b>  Methane	<b>3000-2800</b> <small>(Note: The absorptions can be seen as several distinct peaks in this region.)</small>	H-C-H Asymmetric & Symmetric Stretch
	<b>1500-1440</b>	H-C-H Bend
<b>Alkenes:</b>  1-Propene	<b>3100-3000</b>	C=C-H Asymmetric Stretch
	<b>1675-1600</b>	C=C Symmetric Stretch
<b>Alkynes:</b>  Propyne	<b>3300-3200</b>	$\equiv\text{C}-\text{H}$ Stretch
	<b>2200-2100</b>	$\text{C}\equiv\text{C}$ Stretch
<b>Aromatic Rings:</b>  Benzene	<b>3100-3000</b>	C=C-H Asymmetric Stretch
	<b>1600-1580</b>	C=C Symmetric Stretch
	<b>1500-1450</b>	C=C Asymmetric Stretch
<b>Phenols &amp; Alcohols:</b>  Phenol      Methanol (Alcohol)	<b>3600-3100</b>  <small>(Note: Phenols <u>MUST</u> have Aromatic Ring Absorptions too.)</small>	Hydrogen-bonded O-H Stretch  <small>(This peak usually appears much broader than the other IR absorptions.)</small>
<b>Carboxylic Acids:</b>  Formic Acid	<b>3400-2400</b> <small>(This peak always covers the entire region with a <b>VERY BROAD</b> peak.)</small>	Hydrogen-bonded O-H Stretch  <small>(Note: This peak can obscure other peaks in this region.)</small>
	<b>1730-1650</b>	C=O Stretch
<b>Ketones:</b>  Acetone	<b>1750-1625</b>	C=O Stretch
<b>Aldehydes:</b>  Ethanal	<b>1750-1625</b>	C=O Stretch
	<b>2850-2800</b>	C-H Stretch off C=O
	<b>2750-2700</b>	C-H Stretch off C=O

<b>Functional Group Names</b> & <b>Example compounds</b>	<b>Absorption Ranges(<math>\text{cm}^{-1}</math>)</b> [Look for a single absorption in these regions, unless stated otherwise.]	<b>Type of Vibration</b> causing IR absorption
<b>Esters:</b>  Methyl Formate	<b>1755-1650</b>	C=O Stretch
	<b>(1300-1000)</b>	(C-O Stretch)
<b>Ethers:</b>  Diethyl Ether (aka-Ethyl Ether)	<b>(1300-1000)</b>	(C-O Stretch)
<b>Amines—Primary:</b>  Ethylamine	<b>3500-3100</b> <b>(TWO PEAKS!)</b>	N-H Stretch
	<b>1640-1560</b>	N-H Bend
<b>Amines—Secondary:</b>  N-Methylethylamine	<b>3500-3100</b> <b>(ONE PEAK!)</b>	N-H Stretch
	<b>1550-1450</b>	N-H Bend
<b>Nitriles:</b>  Methanenitrile	<b>2300-2200</b>	C≡N Stretch
<b>Nitro Groups:</b>  Nitromethane  (Note: Both peaks are <200 $\text{cm}^{-1}$ apart.)	<b>1600-1500</b>	N=O Stretch
	<b>1400-1300</b>	N=O Bend
<b>Amides:</b>  Methanamide	<b>3500-3100</b>	N-H Stretch (similar to amines)
	<b>1670-1600</b>	C=O Stretch
	<b>1640-1550</b>	N-H Bend

### 3.4 Optical Microscopy

Humans have always been curious to learn new things, to investigate unknown fields and to lead themselves to new discoveries. Therefore, it was always of great interest to be able to see and examine extremely small things as if they were bigger objects that people could normally see. For this reason, the concept of magnification was considered. At about 1267, Roger Bacon, an English philosopher wrote that “[We] may number the smallest particles of dust and sand by reason of the greatness of the angle under which we may see them”. Three centuries later, in 1538, an Italian physician named Girolamo Fracastoro had written that “If anyone should look through two spectacle glasses, one being superimposed on the other, he will see everything much larger” [135].

However, it is well-known that it is not possible for an object to be observed in a distance smaller than 25 cm from the eye, without losing its resolution. Therefore, the use of a lens was needed as a lens can give the eye the impression that the object is in 25 cm distance, while in fact the distance is shorter. In 18<sup>th</sup> century, Antony van Leeuwenhoek, who is considered the father of the microscope, by using a simple lens, had achieved magnifications up to 250 times. Hence, he was able to observe and, in the end, to discover bacteria. This was the beginning of the creation of the simple and later of the composite optical microscope [136].

A simple microscope uses a single lens and that's the main difference with a compound microscope that is composed by a system of lenses [137]. Thus, this system allows for higher magnification and larger final images. For research purposes, the microscopes usually utilized are the compound ones.

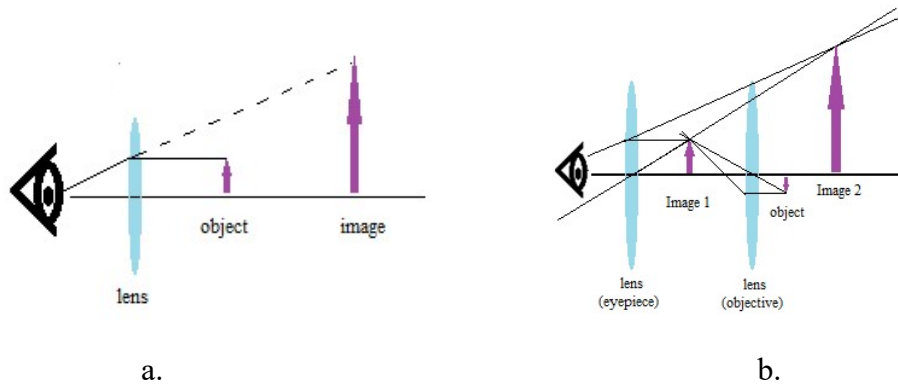


*Figure 3.10. Diagram of a. a Simple microscope and b. a Compound microscope.*

The majority of the microscopes have the following components [137]:



*Figure 3.11. The optical microscope used during this study and its components.*

1. Ocular lens: In other words called eyepiece, usually in four different types (Huygens, Ramsden, Kellner and compensators). The compensators are the most up-to-date and allow the observation without the eye being in contact with the lens. A camera can be mounted on top.

2. Objective turret: Used to hold multiple objective lenses. It usually has seats for 3-6 lenses.
3. Objective lenses: Their function is to collect light from the sample. There are typically 3-6 objective lenses screwed in a circular objective turret in order to select which magnification, thus objective lens is required.
4. Focus Knob: It moves the stage up and down (coarse adjustment).
5. Focus Knob: It moves the stage up and down (fine adjustment) for higher precision.
6. Specimen holder: It is usually a stage that can be either square and fixed or round and rotating (for polarizing microscopes), with a system of micrometric screws for moving the sample. The sample is located on top of a slide which is held by some arms on the stage, while in the center of the stage, underneath the slide, there is a hole in order the light to pass through it and to illuminate the sample.
7. Light source: Usually a halogen lamp, while nowadays LEDs and lasers can also be used. The simplest light source that can be used is the sunlight directed via a mirror.
8. Diaphragm and condenser: Diaphragm's (Iris') role is to limit the bright cone that radiates the specimen, so that it doesn't receive rays from diffraction or refraction. The condenser lens is used for focusing the light on the plane of the sample.
9. Mechanical stage: The stage is a platform connected with the specimen holder so that the sample can be moved to the left and to the right.

### **3.5 Field Emission Scanning Electron Microscopy (FESEM)**

The difference between an optical and a scanning electron microscope is that the latter one uses a high energy electron beam instead of light. The principle of function of the scanning electron microscopy (SEM) is the following one:

Initially, an electron gun produces an electron beam (of energy 1-50 keV) [136], which is accelerated by an electric field and passes through two concentrated lenses so that it is focused (diameter up to 10 nm) to a point of a specimen. This entire system is located inside a high-vacuum chamber. When the beam falls on a spot of the sample, it generates secondary electrons that are collected by an electron detector. The detector converts them into photons by using a suitable system and afterwards, the photons are driven to a photoconductor where they take the form of electric pulses. The pulses are amplified by a signal amplifier and they are used to modulate the brightness of a cathode ray tube (CRT). The brightness is determined by the intensity of the emitted secondary electrons in the region of the sample that is exposed to the electron beam and recorded by the probe. Therefore, the morphology of that region is the one determines the brightness. Hence, holes or recesses of the surface appear

black on the screen, as few of the produced secondary electrons reach the detector. On the other hand, ledges of the surface appear white-gray as many secondary electrons can reach the detector.

Field emission scanning electron microscopy (FESEM) is a special category of scanning electron microscopy. It can provide information about elements and topography with magnifications up to 300.000x with almost unlimited depth of field. In comparison with SEM, FESEM produces clearer and less electrostatically distorted images with spatial resolution up to 1 and  $\frac{1}{2}$  nm, which is three to six times better. Other advantages of FESEM include examination of smaller area contamination points, reduced penetration of detectors closer to the specimen surface, as well as high quality images with negligible electrical charge on the samples.

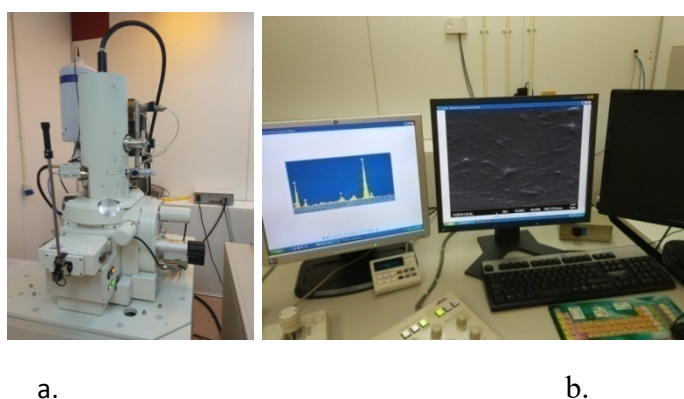


*Figure 3.12. a) The Field Emission Scanning Electron Microscope utilized during this work, b) Examination of the morphology and elemental analysis of a graphene oxide thin film on top of glass/parylene substrate.*

The principle of function of FESEM is the following one: Inside an electron gun of a scanning electron microscope there is a field emission cathode which provides closer detection of the beam at both low and high electron energy. This leads to a better spatial resolution and to less charge and damage of the sample. Similar to SEM, FESEM needs also a vacuum chamber.

The vacuum system of the electron microscopes aims to the removal of the molecules of air. This is necessary as [136]:

1. The electron beam will collide with the air molecules and will be scattered by them thus, a blurry image is created with reduced contrast.
2. Ionization and electrical discharges can be present due to air, therefore this can lead to instability of the electron beam.
3. The presence of air reduce the lifetime of the cathode filament and
4. It can carry dirt onto the sample.

### 3.6 Electrical Measurements

Electrical measurement is a principal tool for characterizing new materials like graphene or semiconductors or in general electronic devices. The relationship between the current passing through a material or device and the voltage across it is represented by a current-voltage characteristic or I-V curve. By obtaining the I-V curve a plethora of information can be provided by the current-voltage reaction to a stimulus. The simplest obtained curve is the one that obeys the Ohm's law and it is linear with a positive slope according to the equation:  $V=IR \rightarrow R = V/I$ , where R represents the Resistance, V the Voltage and I the current. By resistance it is meant the measurement of the opposition of a specimen or object to the flow of electric current. Its unit in System International (SI) is the ohm ( $\Omega$ ). Thus, information about resistance can be gained by the slope of the I-V curve as resistance is equal to the reciprocal of the slope.

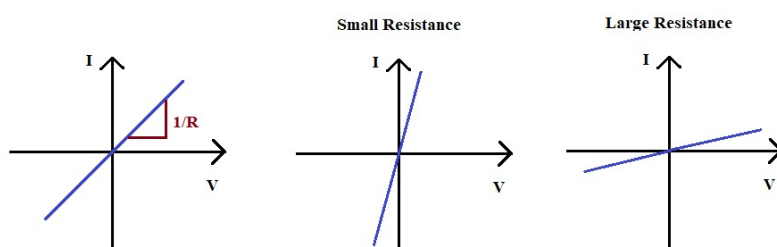


*Figure 3.13. Current-voltage characteristic of a resistor with large and small resistance according to Ohm's law  $V=I \cdot R$ .*

The shape of the curve presents a lot of information about the properties of the material or device. There are four different types of I-V curves [138]:

1. Active or passive: When the I-V curve is located in the first and third quadrant it is considered to consume electric power from the circuit, hence it is a passive component. On the other hand, when the I-V curve is located in the second or fourth quadrant of the graph it is considered to produce electric power, thus it is an active component. Resistors belong to the passive and batteries to the active category.
2. Linear or non-linear: When the I-V curve is a straight line it displays a linear circuit element and when it is curved it displays a non-linear one. The non-linear ones are usually diodes and transistors, while the linear ones are typically resistors and capacitors that obey Ohm's law.
3. Negative or positive resistance: When the I-V curve has peaks and valleys and a negative slope it shows a device with negative resistance. In contrast, an I-V curve with positive slope represents a material with positive resistance.
4. Hysteresis or single-valued: When the I-V curve is a closed loop, that means that the material or device has a hysteresis and it depends on both present and past inputs.

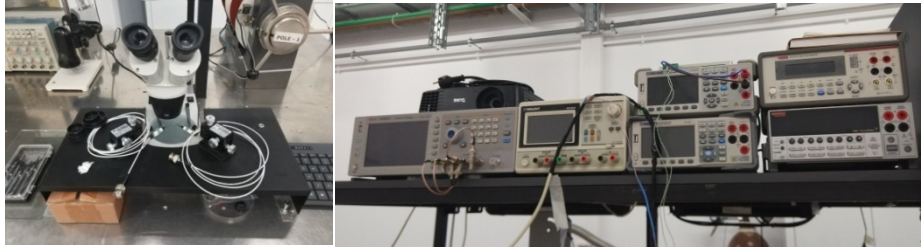


*Figure 3.14. The two-probe system used for the electrical measurements of this work.*

For the reduction of GO, the desired I-V curve is a linear one with small resistance. The resistance is calculated by the slope of the I-V characteristics and a small resistance indicates higher conductivity. Using the resistance from the I-V measurements it is easy to calculate the resistivity of the sample. Resistance is proportional to its resistivity and its length and inversely proportional to its area of cross section, according to the equation:  $R = \rho \frac{L}{A} = \rho \frac{L}{Wt}$ , where L is the length, A is the cross section and  $\rho$  the resistivity. The cross section can also be written as the width, w, of the sample multiplied by its thickness, t. Thus, resistivity can be written as  $\rho = R \frac{A}{L} = R \frac{Wt}{L}$ .

Resistivity, defines the dependence of an object on the material it is made of. For example, samples made of electrical conductors have very low resistance, while specimens made of electrical insulators have high resistance. By the resistivity one can calculate the conductivity which is the most important indicator of an electronic device or of a conductive material, as it shows how easily the current passes through it. Resistivity is inversely proportional to conductivity, according to the equation:  $\sigma = \frac{1}{\rho}$ , where  $\sigma$  is conductivity. Thus, the lower the resistivity the higher the conductivity will be. What is also worth mentioning is that by knowing the resistivity and the thickness, sheet resistance can also be calculated  $\rho = R_s t \rightarrow R_s = \frac{\rho}{t}$  or  $R_s = R \frac{W}{L}$ .

Sheet resistance is defined as a specific case of expressing resistivity for a uniform sheet thickness [138]. It is mostly used for 2D systems, like thin films and it is entailed that in such occasions the current is not measured perpendicular to the plane of the sheet but along to it. Its units in SI is  $\Omega/sq$ , which is equal to an ohm but used for sheet resistance in order not to misunderstand it with bulk resistance [120]. For example, a square sheet of  $1\Omega/sq$  sheet resistance has an actual resistance of 1 Ohm, independently of the size of the square. Sheet resistance is usually measured by a four-point probe or two-point probe device and it is considered to be very important.

In scientific papers, neither resistance nor resistivity, but sheet resistance is used in order to compare results. The reason for this is that, below the scaling of the contact of the film, sheet resistance is not fluctuating, thus, there is the ability to compare the electrical properties of objects, devices or samples with different sizes [138].

## CHAPTER 4

### EXPERIMENTAL METHODS, SET-UP AND PROCEDURE

#### 4.1 Experimental Methods

As graphene has such remarkable properties, its production in large scale was a tremendous need. However, just peeling away graphitic strips with the scotch tape would not lead to a massive production. For this reason, scientists had to find out other ways fabricate enough graphene for experimental purposes.

Graphene oxide and its reduction was a solution to this problem because it offers many advantages both in general and for this study. More specifically, as the main goal is to create graphene-based electrodes that will be implanted into the brain, the hydrophilicity and biocompatibility of GO play an important role. Thus, GO was the suitable material for this project.

The approach used in this master thesis involves GO thin films to be used as the coating where the electrodes will be produced. Vacuum filtration and spray coating methods were utilized for the deposition of GO on the substrates. Vacuum filtration is a method to separate liquids from solids. It has many advantages, as GO can be deposited as a thin film on top of mixed cellulose ester (MCE) membranes that are flexible and biocompatible or to be transferred from the membranes to glass, which is also biocompatible. As for the preparation of GO thin films on top of glass and glass with parylene on the top, substrates were provided by our partners from Linköping University in Sweden, and spray coating method was used. This technique was preferred over the traditional spin coating as it provides more benefits [139, 140]. First of all, in spin coating the quantity of the material used is usually large as there is a large loss of material and only a small quantity of it is deposited on the substrates. Furthermore, deposition via spin coating can create a non-flat film or in non-flat surfaces the film will definitely not be uniform. On the other hand, spray gun method offers uniform films on any kind of surface, even in surfaces with cavities. Finally, among its other advantages, the controlled size of the droplet and the spray nozzle parameters that can also be controlled give high quality results and repeatability in method.

The spray coating of GO was performed on top of glass, of glass covered with parylene and of glass treated with silane and then covered with parylene. The main goal for the use of these three substrates is to find out which is better for both the creation of the electrodes and for the implantation in the brain. Glass is already known as biocompatible material, but parylene-C also has many advantages both for its electrical properties and for implantation. It is a poly(p-xylylene) polymer that can be used as a dielectric. It has low dielectric constant and high dielectric strength; it is free from impurities and chemically and biologically inert. It is of low cost, while its soft

and flexible nature matches the flexibility of brain tissues. Thus, it is a very good and biocompatible candidate and it is already used as coating in implantable medical devices [141]. Silane was also used on the other specimen in order to treat the glass. Silane is an inorganic compound in a gas state. It is used as a stabilizing material as it can enhance bond strength; in this case, between glass and parylene-C. Therefore, in order to create beyond state-of-the-art free-standing electrodes it will be necessary to test GO film on parylene that can be detached from glass (without silane) and also GO on the whole system glass-parylene (glass treated with silane).

As mentioned, GO is biocompatible, however it is not conductive. But conductivity is a tremendous need as the purpose is to produce electrodes that will transfer electrical signals, similarly to the nervous system that functions as a network sending messages from the brain to the body. For that reason, reduction of GO is needed in order to reduce the amount of oxygen in GO, so that a moderate conductivity can be recovered [50].

The technique selected for the GO reduction was laser reduction, as it is the most suitable and advantageous technique, according to the analysis in paragraph 1.2. The laser used for the GO reduction was a femtosecond laser, whose pulse duration is shorter than the thermalization time of the material, as mentioned in paragraph 1.3. Therefore, it does not heat the whole sample, as the absorbed laser energy is not converted into diffused heat in the GO lattice. On the contrary, the chemical bonds between the carboxylic and hydroxylic groups of GO are broken due to the locally absorbed photon energy, exactly in the bonding area [142]. According to Wan *et. al* results [143], two mechanisms were found to govern the laser reduction using a femtosecond laser. The first mechanism is the photothermal effect, induced by the laser locally, which is responsible for the restoration of  $sp^2$  graphene structure and for the removal of oxygen containing groups by the localized higher temperatures. The second mechanism is the photochemical effect, which corresponds to the direct breakage of the bonds between the carbon and the oxygen atoms.



*Figure 4.1. GO reduction and breaking of the C- OH bonding due to a. Photothermal effects and b. Locally absorbed photon energy due to photochemical effects [142].*

Worth mentioning is also their statement [143] about the fluence range and the varied degree of reduction depending on the oxygen containing groups. Their results showed that in lower fluences the restoration of  $sp^2$  hybridization is dominant, as only a small

percentage of oxygen groups requires lower fluences in order to be removed, while in higher fluences the direct breakage of the bonds is mostly dominant, resulting in lower amounts of remaining oxygen groups. As a consequence of this photochemical effect (direct breakage of the chemical bonds) and of the removal of high percentages of the carbonyl-, carboxyl- and hydroxyl-groups, a mass loss occurs in the rGO film, resulting in lower thickness than the original GO film and shorter distances between the rGO sheets (Figure 4.2). Thus, electron transport is facilitated and conductivity is increased.

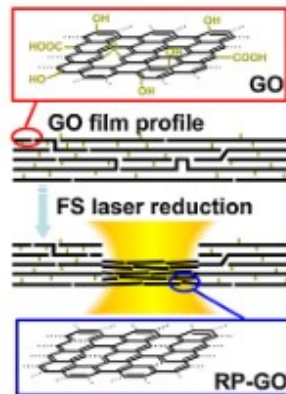


*Figure 4.2. GO reduction utilizing femtosecond laser irradiation in the NIR region. After the laser reduction the thickness of the rGO film is lower than the GO one, while the rGO sheets are less distant, due to the oxygen containing groups' removal [144].*

## 4.2 Experimental Set-Up

The set-up used for the experiments is shown in Figure 4.3. Initially, an  $\text{Yb}^{3+}:\text{KGd}(\text{WO}_4)_2$ , shortly known as Yb:KGW PHAROS laser was utilized at the wavelength of 513 nm, with repetition rate at 60 KHz for the reduction of the GO specimen. The laser beam was driven in the desired height with the help of two mirrors and then passed through an iris. Afterwards, another mirror turned the beam so that it can pass through a neutral density for controlling the power and then, through the center of a shutter, the beam fell onto the last mirror above the lens. The lens of focus at about 6 cm, focused the beam on the sample with a spot of 30  $\mu\text{m}$  diameter. The sample was located on top of an XYZ stage, which can move it to the desired place.

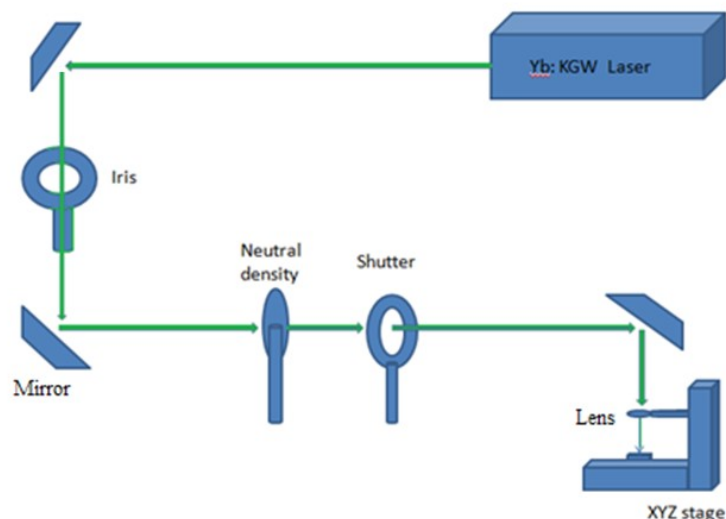


*Figure 4.3. Experimental set-up*

It is worth mentioning that Yb:KGW belongs to the latest and most modern laser technologies, offering very promising results. Its crystal has very long emission lifetime and it is considered as the successor of Nd:YAG and Yb:YAG crystals. According to the analysis held by Casalino *et al.* [145], this type of laser has a variety of advantages such as dimensional accuracy, minimization of both thermal defects and processing duration, control of the geometric parameters and variation of laser-matter interaction depending on the pulses or the wavelength.

In general, it is considered of a very high efficacy.

### 4.3 Experimental Procedure

Vacuum filtration and spray gun technique were the preferred methods for the preparation of GO films.

For the experiments of vacuum filtration, 4 ml of deionized water and 200  $\mu$ l of single-layer GO solution were used. This solution was sonicated at first, in order to avoid the existence of sediments or aggregation of GO flakes, and then it was put in the flask of the set-up on the top of a mixed cellulose ester membrane. This set-up was connected to a vacuum machine that absorbed the deionized water and the GO stayed as a thin film on top of the membrane. These thin films were transferred from the membrane to microscope's glass by wetting them using deionized water and stuck them upside down on the glass. After putting a load on them and waiting over night the membranes were then peeled off and the GO film was successfully transferred on the glass substrate. These glasses were at first cleaned with air, then sonicated in

deionized water, then in acetone and then in isopropanol for 10 min each. They were put then in the oven for 20-30 min and finally, they were UV-ozone treated for 15 min, before the transfer of GO film, so that their hydrophilicity is increased. In order to approach good transferring and nice and homogeneous films on glass optimized conditions for the sonicated solution had to be found. For that reason, the transferring of films was examined after varying the dispersion time of the GO solution in 5, 10, 15, 20 and 30 minutes sonication in order to examine which dispersion time displays the best results.

The second method for fabricating GO thin films was spray gun. Spray gun was used to create films on commercial glasses with 1.5 ml (30 cycles), 3 ml (60 cycles), 6 ml (120 cycles) and 9 ml (180 cycles), respectively. The glasses used for the deposition were first annealed at 85°C and plasma treated at 50 W for 3 min, in order to increase their hydrophilicity. The thickness and the homogeneity of the GO films were tested by varying the concentration of the GO solution until a desired thickness suitable for reduction was achieved.

UV-Vis, Raman and FTIR techniques followed for the identification of GO structure before laser irradiation, while SEM cross-section was performed in order to define the GO film thickness. When the required thickness was achieved, the preparation for the laser reduction was pursued. By tuning the laser parameters such as laser and scanning speed, it was possible to find out which conditions give the best result. Afterwards, Raman mapping and electrical measurements took place in order to complete the parametric study. In the end, the electrodes were produced with the optimized conditions that give good electrical results but that, also, do not destroy the polymeric substrate. Characterizations for the final electrodes followed.

## CHAPTER 5

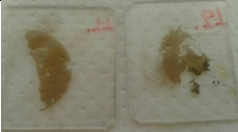
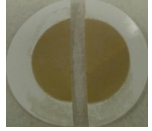
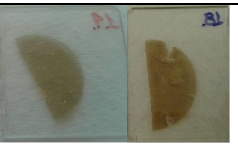
### RESULTS AND DISCUSSION

Two deposition methods were tested (Vacuum filtration and Spray gun technique) in order to conclude which one produces the best homogeneous films on top of the selected substrates.

#### 5.1 Vacuum filtration (on membranes and commercial glass)

For the experiments of vacuum filtration, dispersion time varied from 5 to 30 min. After the creation of the films on top of cellulose membranes, transferring of the film on glass substrates followed. Table 5.1 represents the optical images of vacuum filtrated GO films with varying dispersion times. It is observed that the sonication time affects the substrate adhesion of the film. The results showed that 10 minutes sonication gave the best transfer of the GO film from the membrane to the glass substrate.

**Table 5.1.** Optical images of the vacuum filtrated GO films created using different times of sonication of the GO solution.

Ultrasonication time	GO thin film on membrane	After transferring on glass
30 minutes		
20 minutes		
15 minutes		
10 minutes		
5 minutes		

Further spectroscopic and microscopic investigation took place, like UV-Vis, Raman, and FTIR, in order to define GO fingerprints and thickness of the films.

UV-Vis spectroscopy was used to study the electronic transitions from the ground state to the excited state. According to the literature [146], two absorption peaks should be observed, one at around 230 nm (5.39 eV) and another one at around 305 nm (4.07 eV). The first one corresponds to  $\pi$ - $\pi^*$  plasmon peak and the second one to  $n$ - $\pi^*$  plasmon peak [146]. The utilized UV-Vis spectrophotometer performs unreliable measurements below 300 nm due to noise. As such, in this work measurements are obtained from 290-300 nm and above. In Figure 5.1 a peak at around 305 nm is observed, which corresponds to the  $n$ - $\pi^*$  plasmon peak and is characteristic for GO.

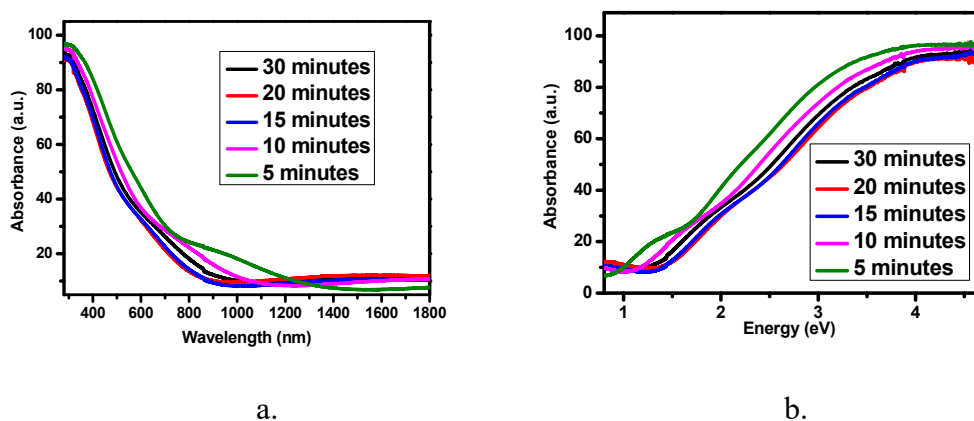


*Figure 5.1. UV-Vis spectra of vacuum filtrated GO films in different sonication times: a) according to the wavelength and b) according to the energy.*

The Raman spectra of GO films displayed five characteristic peaks (Figure 5.2). The Lorentz function was fitted in order to find the peak positions of the Raman spectra. The individual peak position of the GO films is tabulated in Table 5.2.

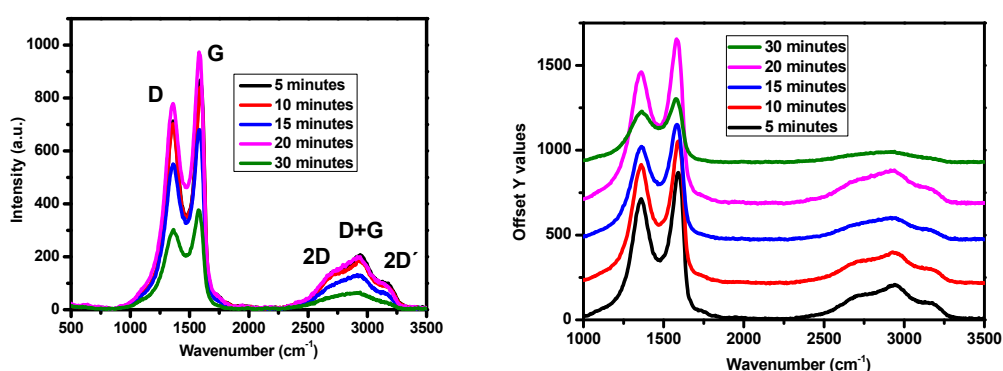


*Figure 5.2. Raman spectrum of vacuum filtrated GO films (using the 473 nm laser line).*

The peaks appeared at  $\sim 1365$ ,  $\sim 1580$ ,  $\sim 2711$ ,  $\sim 2944$ , and  $\sim 3170$   $\text{cm}^{-1}$  corresponding to D, G, 2D, D+G and 2D' modes, respectively [147]. The D band is associated with the disorder (introduced by vacancies or grain boundaries) in edge or amorphous carbon species [148,149]. The intensity ratio of the D and G bands ( $I_D/I_G$ ) is 0.82, 0.83, 0.80,

0.80, and 0.80 for 5, 10, 15, 20, 30 min, respectively. This indicates that dispersion time can affect the creation of films and their adhesion on membranes or glasses. Thus, sonication for longer time can affect the existence of functional groups, especially if by sonicating up to 30 min a small amount of heat can be created. The  $I_D/I_G$  ratios of the GO solutions sonicated for different amount of time do not show significant value difference, however the GO sonicated for 10 min had the highest  $I_D/I_G$  ratio. It seems that 10 min was the optimum condition for dispersion (no precipitates) and that it contained the majority of oxygen groups. Thus, its hydrophilicity is the reason for its better stacking on the glass (Table 5.1).

**Table 5.2.** Lorentzian fitted Raman spectral peak position of Vacuum filtrated GO films.

Film Number	Dispersion Time (minutes)	D band ( $cm^{-1}$ )	G band ( $cm^{-1}$ )	2D band ( $cm^{-1}$ )	D+G band ( $cm^{-1}$ )	2D' band ( $cm^{-1}$ )
17	5	1361	1585	2711	2944	3170
20	10	1361	1585	2713	2944	3169
32	15	1364	1577	2686	2925	3164
28	20	1361	1576	2687	2928	3163
15	30	1367	1574	2652	2910	3166

Fourier Transform Infrared- Attenuated Total Reflectance spectroscopy (FTIR-ATR) was utilized to study the molecular structure of each GO thin film, to identify the organic substances and to inform about any changes of the concentration of specific groups in the material. The FTIR-ATR spectrum, including all the dispersion times examined is shown in Figure 5.3. As the substrate on which the films are deposited is glass, and as glass is a very poor mid IR transmitter, the full spectrum was measured in reflectance. The peaks for GO appeared at  $1076\text{ cm}^{-1}$ ,  $1394\text{ cm}^{-1}$ ,  $1402\text{ cm}^{-1}$ ,  $1636\text{ cm}^{-1}$ ,  $1655\text{ cm}^{-1}$ ,  $1720\text{ cm}^{-1}$ ,  $2365\text{ cm}^{-1}$ ,  $2875\text{ cm}^{-1}$  and  $3370\text{-}3395\text{ cm}^{-1}$ . These peaks correspond to the vibration of the C-O and C-OH molecules, of the OH deformation, of the C=O, CO<sub>2</sub> and C-H molecules, while the peaks in the range  $3370\text{-}3395\text{ cm}^{-1}$  correspond to the elongation of the O-H bond [150-152]. There are also two peaks that appear at around  $765\text{ cm}^{-1}$  and  $895\text{ cm}^{-1}$  and which correspond to the bands of the glass substrate [153].

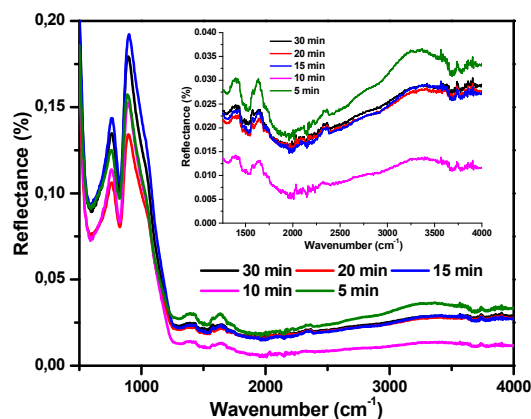


*Figure 5.3. FTIR-ATR spectrum of vacuum filtrated GO films (Inset: Magnified wavenumber range after 1200  $\text{cm}^{-1}$ ) in agreement with the references [150-152].*

However, there was an important drawback in this method. GO films were transferred successfully on glass, but they were not attached permanently. After a period ranging from several days to weeks, they were detached and peeled off from the glass. Therefore, they lacked required characteristics for brain implantation, such as physical integrity and long-lifetime. For this reason, research interest was focused on the spray gun technique.

## 5.2 Spray gun (on commercial glass substrates)

Spray gun method was used to create thin films on commercial glasses and substrates provided by our partners from LiU, by varying the volume of GO. Figure 5.4 represents the optical images of spray gunned GO films developed in different volumes on commercial glass.

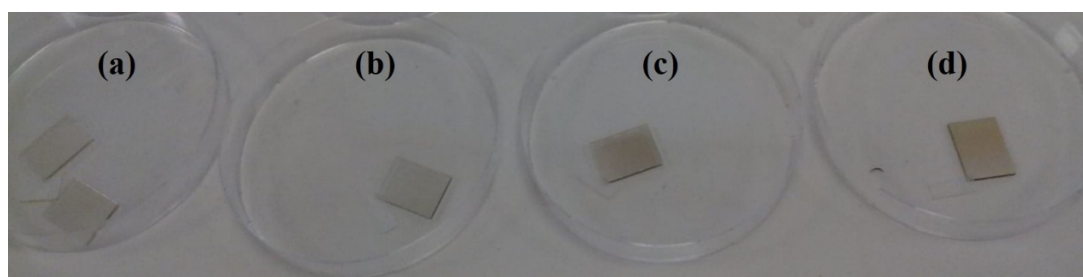


*Figure 5.4. Optical image of spray gunned GO films on glass. (a) 30 cycles- 1.5 ml, (b) 60 cycles- 3 ml, (c) 120 cycles - 6 ml and (d) 180 cycles - 9 ml.*

Afterwards, Raman and FTIR spectroscopies were performed in order to evaluate the quality and the molecular structure of GO films prepared by this technique.

The Raman spectra of GO films displayed five characteristic peaks (Figure 5.5). Lorentz function was fitted in order to find the peak positions of the Raman spectra. The individual peak position of the GO films is tabulated in Table 5.3. The peaks appeared at  $\sim 1350$ ,  $\sim 1591$ ,  $\sim 2711$ ,  $\sim 2925$ , and  $\sim 3155 \text{ cm}^{-1}$  corresponding to D, G, 2D, D+G and 2D' modes, respectively. The D band is associated with the disorders [149]. The G band is due to the doubly degenerate zone center  $E_{2g}$  mode, which is a primary component parallel to the vibrational level (in-plane) and the 2D band, is the second order of zone- boundary phonons (different parallel vibrational component) [154].

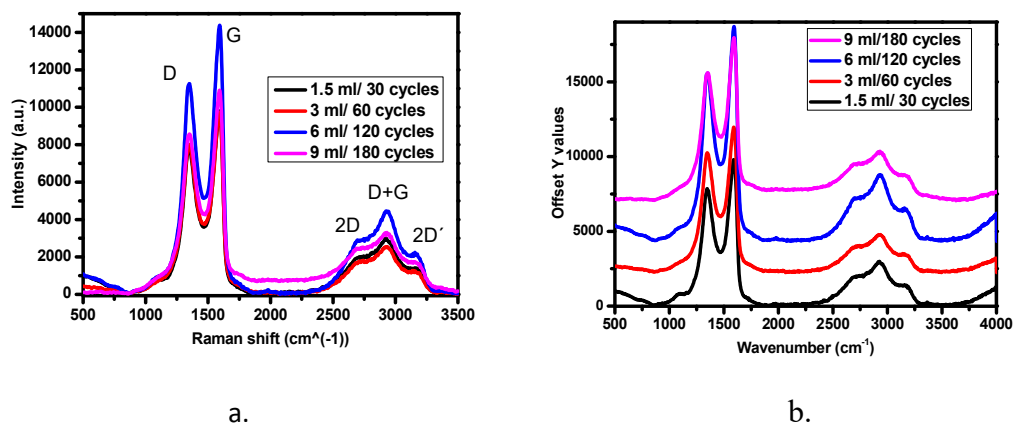


**Figure 5.5.** Raman spectrum of spray gunned GO films (using the 473 nm laser line) in both a. Line and b. Stacking format

The intensity ratio of the D and G bands ( $I_D/I_G$ ) is 0.802, 0.846, 0.847 and 0.849 for 30 cycles, 60 cycles, 120 cycles and 180 cycles, respectively. It is observed that the  $I_D/I_G$  ratio increases as the number of cycles increases. This increase could be due to the fact that the material as it has more volume (more /cycles) starts to behave more like a multilayer/bulk than a monolayer. The more material added (more ml of GO), the higher amount of the defects exist.

**Table 5.3.** Lorentzian fitted Raman spectral peak position of spray gunned GO films.

Number of cycles or ml value	D band ( $\text{cm}^{-1}$ )	G band ( $\text{cm}^{-1}$ )	2D band ( $\text{cm}^{-1}$ )	D+G band ( $\text{cm}^{-1}$ )	2D' band ( $\text{cm}^{-1}$ )
30 cycles or 1.5 ml	~1346	~1589	~2711	~2916	~3161
60 cycles or 3 ml	~1346	~1591	~2711	~2918	~3157
120 cycles or 6 ml	~1350	~1593	~2717	~2925	~3155
180 cycles or 9 ml	~1352	~1591	~2711	~2931	~3151

FTIR-ATR was also utilized, in order to study the molecular structure of each GO thin film, to identify the organic substances and to inform about any changes of the concentration of specific groups in the material. The FTIR-ATR spectrum, including all the cycles of the spray gun, is shown in Figure 5.6. Same as in vacuum filtration technique, the substrate on which the films are deposited is glass and as glass is a very poor mid IR transmitter, the full spectrum was measured in reflectance as well. There are some characteristic peaks of GO that were found at around  $1664 \text{ cm}^{-1}$  and  $2375 \text{ cm}^{-1}$ . These peaks correspond to the vibration of the OH deformation and of the C=O

stretching, respectively [150]. There are also two peaks appeared at around  $765\text{ cm}^{-1}$  and  $895\text{ cm}^{-1}$  that correspond to the bands of the glass substrate for the vibrations of O-Si-O and Si-O-B, respectively [153,155].

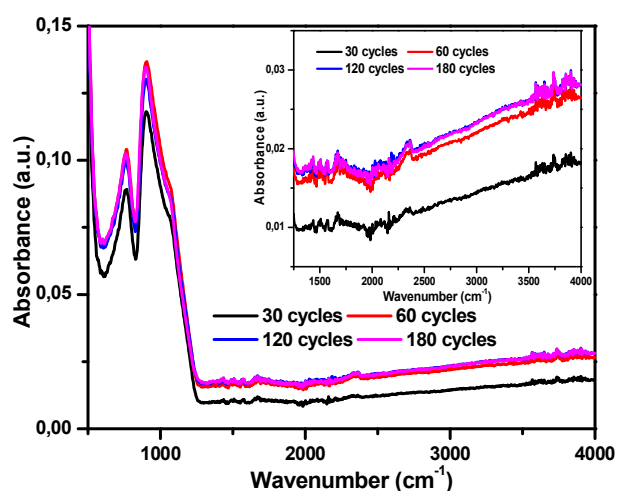


*Figure 5.6. FTIR-ATR spectrum of spray gunned GO films (Inset: Magnified wavenumber range after  $1200\text{ cm}^{-1}$ ).*

In order to investigate the surface topography of the films, an optical microscope (OM) was utilized. Figure 5.7 represents the OM images of GO films produced by spray gun method (different number of cycles 30, 60, 120, and 180 cycles). A clear deviation in surface morphology with the number of cycles appeared. A clearly inhomogeneous film was obtained both for 30 and 60 cycles. However, a more continuous and homogeneous film was observed both in 120 and 180 cycles.

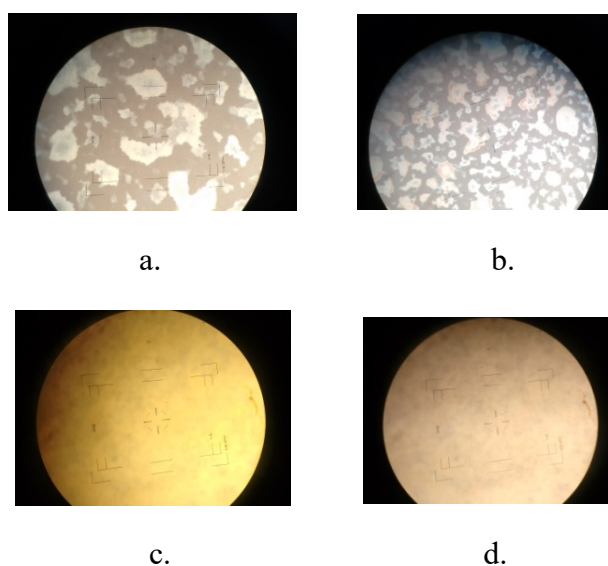


*Figure 5.7. Optical microscopic images of GO films produced by spray gun technique. a) 30 cycles, b) 60 cycles, c) 120 cycles and d) 180 cycles.*

Field Emission Scanning Electron Microscope (FESEM) was used to acquire the cross-sectional view of the films. The films were inhomogeneous in thickness (120 and 180 cycles) as it can be observed in the Figure 5.8. However, the cross sectional view of the films produced by 20 and 60 cycles was not measurable due to their very small and indistinguishable thickness.

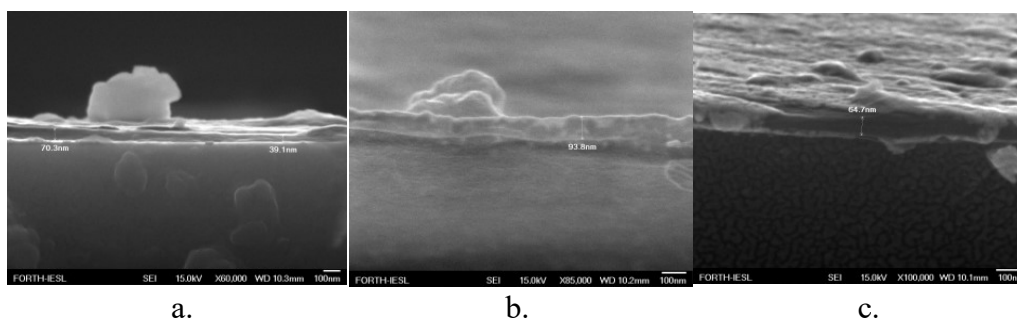


*Figure 5.8. Values for thickness in different locations of the same sample a) of the 120 cycles spray gunned GO films that vary from 39-70 nm and b), c) 180 cycles spray gunned GO films that vary from 64-93 nm.*

As it was confirmed by Raman, Optical and Scanning Electron Microscopy, the GO film prepared with 9 ml and 180 cycles was the best film fabricated by this method. However, as the creation of a uniform film had not been achieved yet, next step was to increase the volume of GO to 18 ml and investigate again the thickness and the uniformity of the films.

### 5.3 Spray gun (on commercial glass and on polymer substrates)

Preparation of GO thin films was performed with the spray gun technique, this time by using 18 ml of GO solution (360 cycles). Furthermore, besides the deposition of GO on commercial glass, deposition of GO on substrates of glass and glass with parylene provided by our partners from Linköping University in Sweden took place as well.



*Figure 5.9. Optical image of spray gunned GO film (18 ml of GO solution-360 cycles) on commercial glass.*

The spray coating of GO was performed on top of glass, on top of glass covered with parylene and on top of glass treated with silane and then covered with parylene.

UV-Vis and Raman spectroscopies were performed in order to characterize the new fabricated films on different substrates. The absorption spectra of the films exhibited a characteristic peak at  $\sim 305$  nm, corresponding to  $n-\pi^*$  band of GO [146].

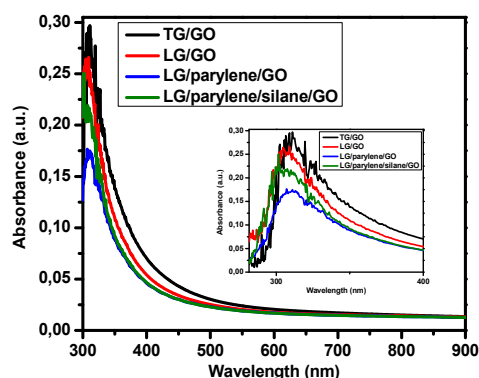


*Figure 5.10. Absorption spectra of GO film deposited on different substrates and adhesive layers. TG refers to commercial glass and LG to Glass provided by LiU. Inset: The absorption spectra of GO film in the wavelength region between 280 and 400 nm.*

Raman spectroscopy was employed to investigate the GO film quality on different adhesive layers. The impact of parylene and silane on the Raman spectra of GO film was investigated. Figure 5.11 represents the Raman spectra of GO films deposited on glass and adhesive layers (parylene and parylene/silane). The adhesive layer of parylene and silane exhibited their characteristic vibrational modes (Inset of Figure 5.11). However, the spectra taken by GO films displayed the characteristic vibrational modes of GO. Therefore, absence of any characteristic peak of parylene and silane confirms a more uniform coating of GO on the adhesive layers.

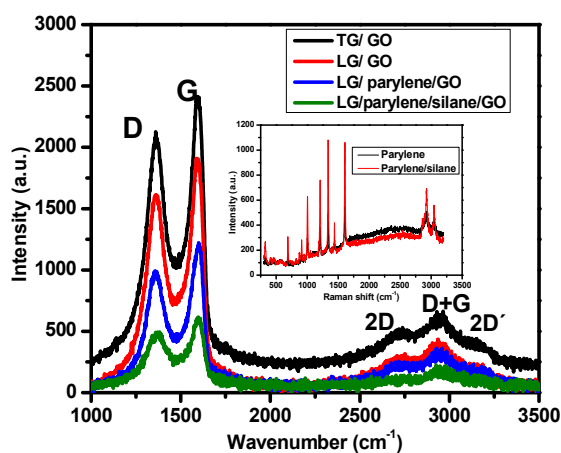


*Figure 5.11. Raman spectra of spray coated GO film on different adhesive layer coated glass substrates. Inset: Raman spectra of control substrates with adhesive layers (Glass/Parylene*

and Glass/Parylene/Silane –see also figure 5.17). TG refers to commercial glass and LG to Glass provided by LIU.

The spectra were fitted with the Lorentzian function to find the peak position (Table 5.4). The peaks appeared at ~1365, ~1580, ~2710, ~2944 and ~3143 corresponding to D, G, 2D, D+G and 2D' modes, respectively. The D band is associated with the disorders, while the G band indicates the decrease in size of the in-plane  $sp^2$  hybridization domains and formation of  $sp^3$  bonds due to oxidation of functional groups [48,156]. Hence, the intensity ratio of D and G bands ( $I_D/I_G$ ) used as a measure of the size of  $sp^2$  domains in a network of  $sp^3$  and  $sp^2$  bonded carbon atoms [157]. The intensity ratio of the D and G bands ( $I_D/I_G$ ) is 0.81, 0.81, 0.79 and 0.91 for TG/GO, LG/GO, LG/Parylene/GO and LG/Parylene/silane/GO, respectively. The intensity ratio is assuring the presence of defects or disorders in the GO films, which is independent of the adhesive layers. However, a significant change in Raman intensity of different modes appears, as the intensity of the D and G bands can be reduced or increased with the adhesive layer. This change of intensity in the Raman modes is possibly due to the interlayer coupling of GO film with the adhesive layers.

**Table 5.4.** Lorentzian fitted Raman spectral peak position and Intensity ratios of spray gunned GO films

Films	D Band ( $cm^{-1}$ )	G Band ( $cm^{-1}$ )	2D Band ( $cm^{-1}$ )	D+G Band ( $cm^{-1}$ )	$I_D/I_G$ ratio
TG/GO	~1362	~1591	~2717	~2943	0.81
LG/GO	~1364	~1586	~2713	~2941	0.81
LG/parylene/GO	~1371	~1590	~2727	~2951	0.79
LG/parylene/silane/GO	~1365	~1584	~2728	~2937	0.91

FESEM was also used to acquire the cross-sectional view of spray coated GO films. Figure 5.12 represents the cross-sectional view of a GO film on a commercial glass substrate. The average thickness of the GO film is  $200 \pm 60$  nm (average value resulted from measurements in 17 different locations on the same film). This large fluctuation of the GO thickness is a result of the spray gun instrument, as it is not a commercial tool but a handmade one. Thus, size of the droplets and spray nozzle parameters do not stay stable, resulting in this not uniform film.

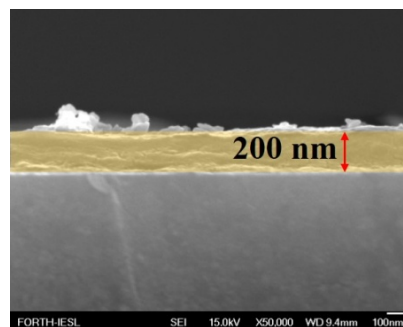


*Figure 5.12.* Cross-sectional view of a spray coated GO film on glass substrate.

However, as the films fabricated with such amount of volume were more regular and homogeneous and as the thickness of the films was quite good for the reduction of GO, the spray gun deposition conditions were optimized at 18 ml GO volume, 85°C annealing and 50 W plasma treatment for 3 min.

As GO is a biocompatible material [158] it is suitable for implantations. However it is not conductive. But conductivity is another tremendous need as the purpose of the project is to produce electrodes for bioelectronic devices. For that reason, reduction of GO was needed in order to reduce the amount of existing oxygen, so that a moderate conductivity can be recovered. Hence, a laser was utilized for the reduction realization.

A dedicated program that controlled the stage was created, so that the laser reduction would create electrodes with the desired shape. By utilizing a femtosecond laser with fluence  $1880 \pm 3 \text{ mJ} \cdot \text{cm}^{-2}$ , a lens with focal length at 6 cm and a silicon sample as a test substrate, the desired design of electrodes was finally achieved (width of each electrode = 100  $\mu\text{m}$ , diameter of patches = 400  $\mu\text{m}$ , length of short r-GO electrodes = 4 mm including patches, length of long r-GO electrodes = 8 mm including patches). The final results on top of silicon substrate are shown in Figures 5.13 a, b.

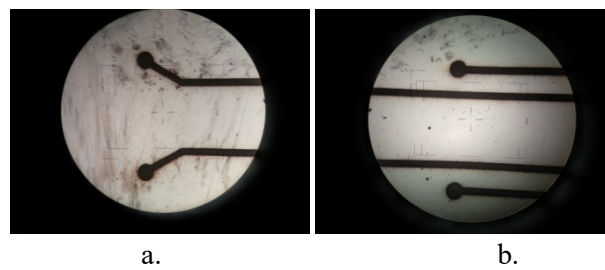


*Figure 5.13. Optical images illustrating the desired shape of the device electrodes. a) Picture of the long electrodes and b) picture of the short electrodes.*

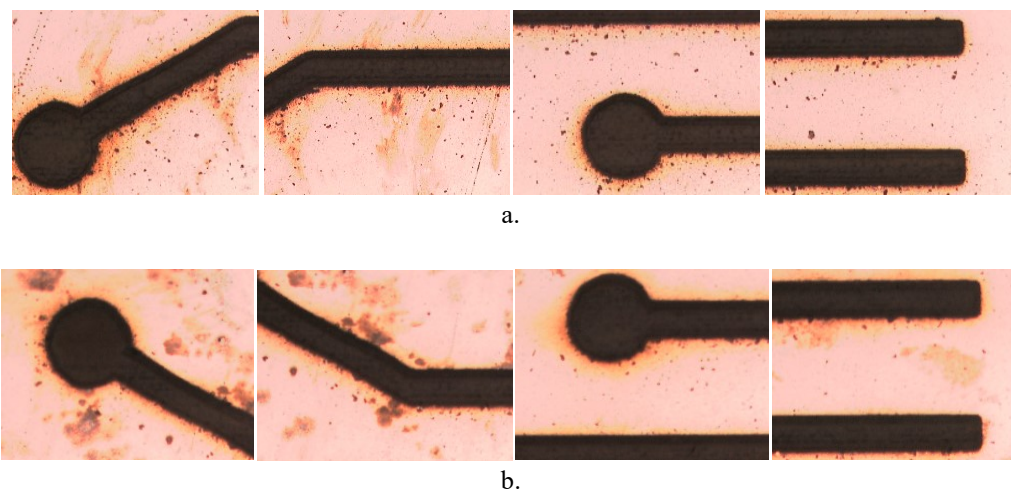


*Figure 5.14. Optical images of a) left and b) right side of the short and long electrodes*

Electrodes were fabricated on top of GO films by testing the most sensitive substrates (glass/parylene and glass/parylene/silane). These test electrodes were produced in

order to check in which range of fluences the fabrication shall take place taking into account the sensitivity of the parylene and also to examine the morphology of the reduced areas and measure their thickness. A convex lens with focal length of 6 cm was used to focus the beam to an elliptical spot size of about 15  $\mu\text{m}$  on GO samples, while the fluence was decreased to  $940 \pm 3 \text{ mJ}\cdot\text{cm}^{-2}$  and the scanning speed was kept stable at  $500 \mu\text{m}\cdot\text{s}^{-1}$ .

Despite the fact that the produced electrodes seemed to be burnt even though the fluence was lowered, a microscopic study (FESEM) was of great importance in order to define their morphology, the thickness of the reduced/burnt areas and the thickness of the parylene layer in each sample. However, there were difficulties in determining the thickness of parylene layers, and thus, Energy-dispersive spectroscopy (EDS) was performed whenever needed, to find out what each layer is composed of.

For the **LG/silane/parylene/GO** 360 cycles/18 ml sample (code **EPLSG.007**), the layer of GO was found at an average thickness of about  $207 \text{ nm} \pm 37 \text{ nm}$  (Figure 5.15 and 5.16a), which is in agreement with the previous measurements.

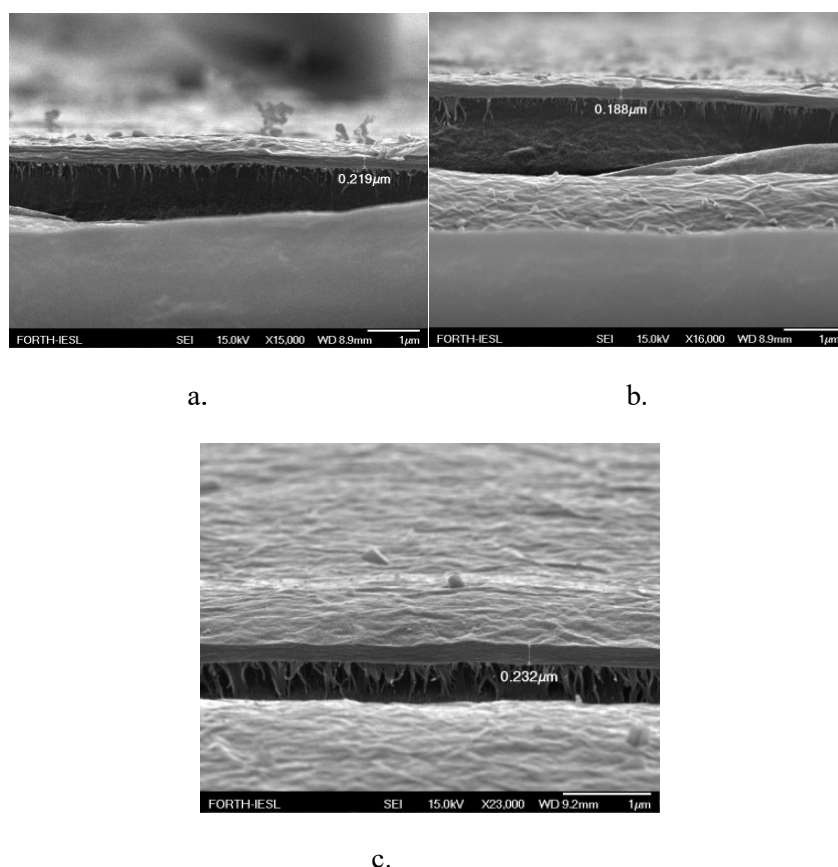


*Figure 5.15. GO layer measured in different places and defined with an average thickness of about  $207 \text{ nm} \pm 37 \text{ nm}$  (average value calculated from 7 different thickness values along the same film). Below the GO film some stacking fibers are observed due to the polymeric nature of parylene.*

As parylene is a polymer, it was sticky and it was reacting like an elastic rubber or plastic. The same behavior was seen from the scanning electron microscopy, as the polymeric material had stack on the glass and on GO film and had formed sticky fibers (Figure 5.15). In addition, it was elongated and swollen (Figure 5.16) with a measured thickness varying between 5 and 20  $\mu\text{m}$ . This stacking phenomenon is enhanced as it is the sample where the glass is treated with silane for better adhesion. For this reason, it was very difficult to distinguish the real thickness of parylene. The average thickness of the elongated parylene obtained by measuring 5 different regions of the same sample was about  $11 \pm 6 \mu\text{m}$ .

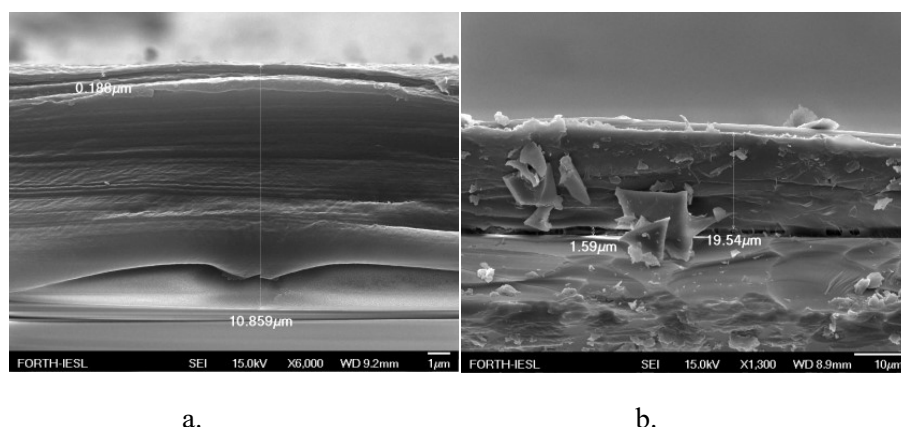


*Figure 5.16. Polymeric parylene layer. In some places it seems to be around 10  $\mu\text{m}$  (a) and in others around 20  $\mu\text{m}$  (b).*

It is also worth mentioning that a gap was created after the cutting process (Figure 5.16 b). Using EDS, it was possible to determine that Si, thus glass, was at the bottom and Chlorine (Cl), thus parylene-C, was at the top of the gap. Therefore, it was certain that this swollen layer was parylene and the gap existed between itself and glass was possibly due to the violent detachment of parylene film during the cutting process.

As for the electrodes patterned on top of the GO film on glass/silane/parylene substrate, FESEM images displayed that the high fluence has dug the material (Figure 5.17a) and it has affected even the glass (like in Figure 5.19a of the LG/parylene/GO). However, the thickness of the laser treated GO film could not be measured, as in this place the film was not uniform anymore, given that several strips of it have been detached (Figure 5.17b). Also, it is not known if the visible strips are the only ones that detached or if there are more that cannot be seen in the image.

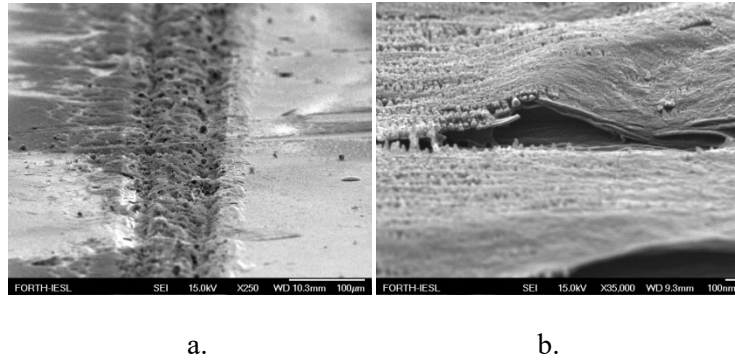


*Figure 5.17. a) Topography of the electrode produced with fluence of  $940 \pm 3 \text{ mJ} \cdot \text{cm}^{-2}$  and b) Detached strips of rGO film.*

Regarding the **LG/parylene/GO** sample (code **EPI.SG.006**), the layer of GO was found at an average thickness of about  $200 \pm 40 \text{ nm}$ , which is in agreement with the previous measurements. The thickness of the parylene was found to be at an average of  $870 \pm 421 \text{ nm}$  (Figure 5.18 and 5.19b).

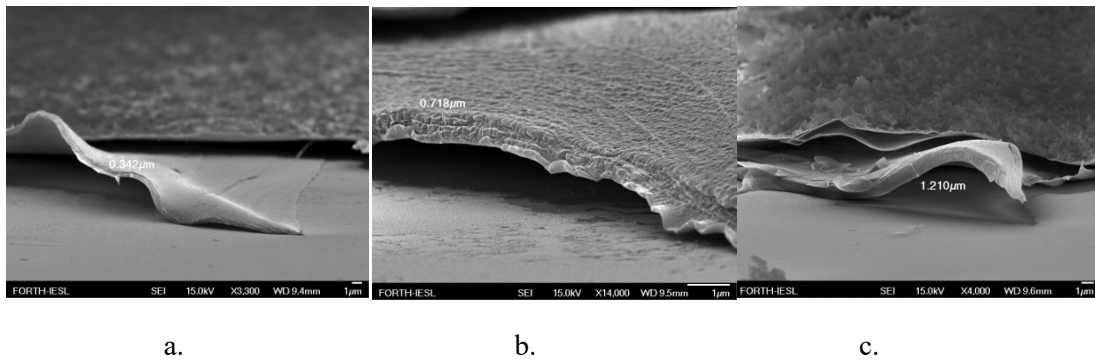
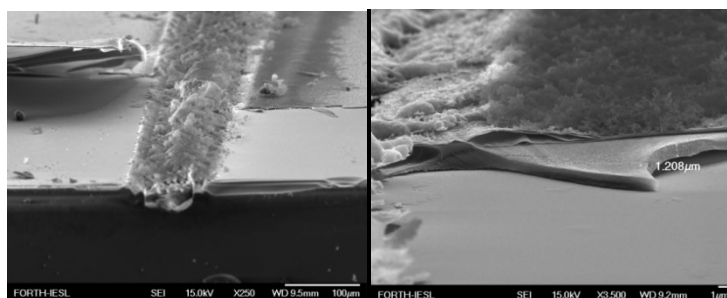


*Figure 5.18. Parylene layer measured in different places and defined at about  $870 \pm 421 \text{ nm}$  average thickness.*

Similar results as the ones for the LG/silane/parylene/GO specimen were also obtained for the electrodes patterned on glass/parylene/GO sample. As shown in Figure 5.19a, due to the high fluence, the material is dug and it has affected the glass, like it happened in the previous occasion as well. As the film was not uniform anymore, it was difficult to measure the thickness of the laser irradiated area. Finally, Figure 5.19b shows also that the laser has affected the topography of the rGO film both in the irradiated and the surrounding areas.



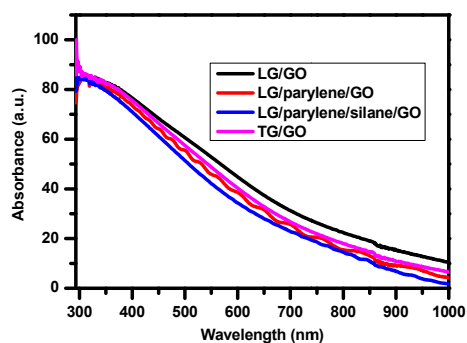
a.

b.

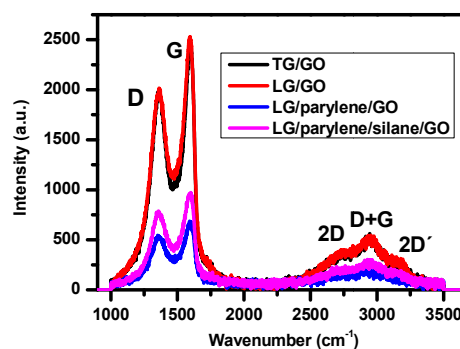
*Figure 5.19. a) Topography of the electrode produced with fluence  $940 \pm 3 \text{ mJ} \cdot \text{cm}^{-2}$  and b) Detached strips of the irradiated GO film and thickness of parylene layer.*

Consequently, a parametric study was needed with the decrease of the fluence to play a key role. Hence new spray coated films were created for that purpose. Nonetheless, even if the volume of GO solution used was the same, as the spray coating device is a homemade and not a commercial tool, the number of cycles can change. Thus, in this case the new films were created with 18 ml volume and 336 cycles.

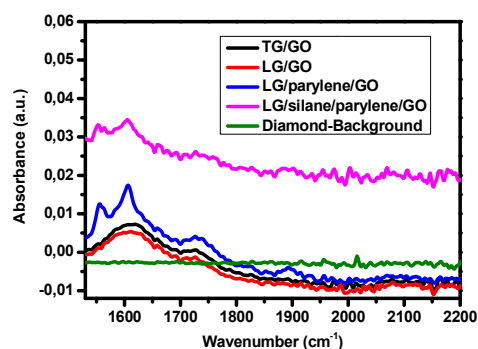
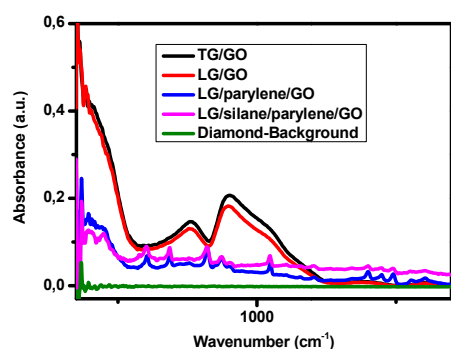
For the characterization of the new films, UV-Vis, Raman and FTIR-ATR spectroscopies were performed. The absorption and Raman spectra represented the characteristic GO peaks. FTIR-ATR spectrum illustrated the characteristic peaks of GO as well.



a.

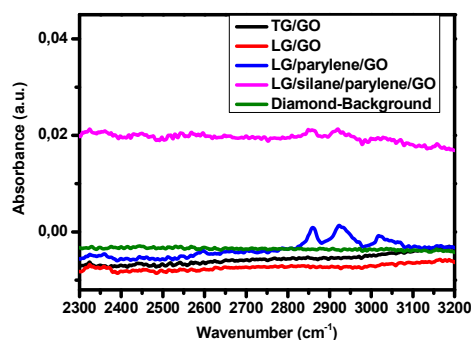


b.



c.

d.



e.

*Figure 5.20. a) UV-Vis spectra, b) Raman spectra and c,d,e) FTIR-ATR spectra of GO films on top of commercial glass, untreated glass with parylene on top and treated glass with silane having parylene on top of it, both latest provided by LiU.*

As it is shown in the graphs, the observed peaks at around  $353\text{ cm}^{-1}$ ,  $365\text{ cm}^{-1}$  and  $413\text{ cm}^{-1}$  are due to the background. Also, the analysis took place only till  $3500\text{ cm}^{-1}$  because after this wavenumber there are no significant peaks.

For the **TG/GO** sample, some peaks exist at around  $385\text{ cm}^{-1}$ ,  $472\text{ cm}^{-1}$ ,  $763\text{ cm}^{-1}$ ,  $891\text{ cm}^{-1}$ ,  $1050\text{ cm}^{-1}$ ,  $1158\text{ cm}^{-1}$ ,  $1380\text{ cm}^{-1}$ ,  $1617\text{ cm}^{-1}$ ,  $1727\text{ cm}^{-1}$ ,  $2081\text{ cm}^{-1}$ ,  $2299\text{ cm}^{-1}$ ,  $2323\text{ cm}^{-1}$ ,  $2362\text{ cm}^{-1}$ ,  $2852\text{ cm}^{-1}$  and a wide peak from  $3000\text{ cm}^{-1}$  to  $3600\text{ cm}^{-1}$  with highest intensity at around  $3335\text{ cm}^{-1}$ . From all these peaks, only the ones at  $1050\text{ cm}^{-1}$ ,  $1158\text{ cm}^{-1}$ ,  $1380\text{ cm}^{-1}$ ,  $1617\text{ cm}^{-1}$ ,  $1727\text{ cm}^{-1}$ ,  $2852\text{ cm}^{-1}$  and  $3335\text{ cm}^{-1}$  belong specifically to GO film. The peaks located at around  $385\text{ cm}^{-1}$ ,  $472\text{ cm}^{-1}$ ,  $763\text{ cm}^{-1}$ ,  $891\text{ cm}^{-1}$ ,  $2081\text{ cm}^{-1}$ ,  $2299\text{ cm}^{-1}$ ,  $2323\text{ cm}^{-1}$  and  $2362\text{ cm}^{-1}$  belong to the soda-lime glass (TG), according to the literature [153], which is the substrate used for the deposition of the GO film. Analyzing the GO peaks it was found that the bands located at  $1050\text{ cm}^{-1}$  and  $1150\text{ cm}^{-1}$  represent the C-O stretching vibration on the GO, revealing skeletal vibrations from graphitic origin [150]. Furthermore, the band at  $1380\text{ cm}^{-1}$  shows the presence of C-O bending vibrations, while the ones at  $1617$  and  $1727\text{ cm}^{-1}$  indicate the C=O stretching from the carboxylic groups. In the end, the bands positioned at  $2852\text{ cm}^{-1}$  and  $3335\text{ cm}^{-1}$ , identify the presence of C-H and the O-H stretching vibration, respectively.

With reference to **LG/GO** sample, the bands are located at  $383\text{ cm}^{-1}$ ,  $443\text{ cm}^{-1}$ ,  $466\text{ cm}^{-1}$ ,  $475\text{ cm}^{-1}$ ,  $760\text{ cm}^{-1}$ ,  $891\text{ cm}^{-1}$ ,  $1050\text{ cm}^{-1}$ ,  $1154\text{ cm}^{-1}$ ,  $1387\text{ cm}^{-1}$ ,  $1612\text{ cm}^{-1}$ ,  $1730\text{ cm}^{-1}$ ,  $2079\text{ cm}^{-1}$ ,  $2327\text{ cm}^{-1}$ ,  $2368\text{ cm}^{-1}$ ,  $2720\text{ cm}^{-1}$  and a wide peak is placed in the range  $3000\text{--}3600\text{ cm}^{-1}$ . The peaks at  $383\text{ cm}^{-1}$ ,  $443\text{ cm}^{-1}$ ,  $466\text{ cm}^{-1}$ ,  $475\text{ cm}^{-1}$ ,  $760\text{ cm}^{-1}$ ,  $891\text{ cm}^{-1}$ ,  $2079\text{ cm}^{-1}$ ,  $2327\text{ cm}^{-1}$ ,  $2368\text{ cm}^{-1}$  and  $2720\text{ cm}^{-1}$  are obtained from the LiU

glass and the rest from GO. In Figure 5.21, the FTIR spectrum of LiU glass (LG) is observed. The peaks of GO identify C-O stretching vibration on the GO, the presence of C-O bending vibrations, the C=O stretching from the carboxylic groups and the O-H stretching vibration, respectively.

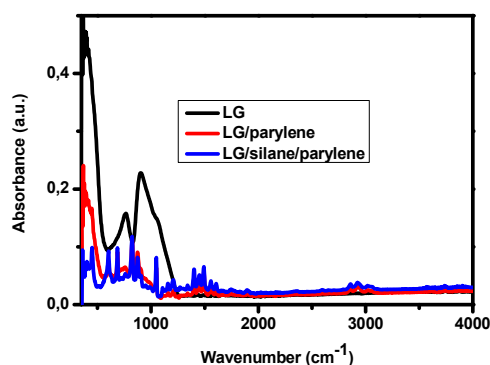


*Figure 5.21. FTIR spectra from LG, LG/parylene and LG/parylene/silane used as references.*

As for **LG/parylene/GO** sample, the peaks appeared at  $604\text{ cm}^{-1}$ ,  $687\text{ cm}^{-1}$ ,  $758\text{ cm}^{-1}$ ,  $820\text{ cm}^{-1}$ ,  $872\text{ cm}^{-1}$ ,  $901\text{ cm}^{-1}$ ,  $1048\text{ cm}^{-1}$ ,  $1109\text{ cm}^{-1}$ ,  $1157\text{ cm}^{-1}$ ,  $1203\text{ cm}^{-1}$ ,  $1400\text{ cm}^{-1}$ ,  $1450\text{ cm}^{-1}$ ,  $1491\text{ cm}^{-1}$ ,  $1552\text{ cm}^{-1}$ ,  $1605\text{ cm}^{-1}$ ,  $2361\text{ cm}^{-1}$ ,  $2595\text{ cm}^{-1}$ ,  $2711\text{ cm}^{-1}$ ,  $2788\text{ cm}^{-1}$ ,  $2860\text{ cm}^{-1}$ ,  $2922\text{ cm}^{-1}$ ,  $3018\text{ cm}^{-1}$ ,  $3066\text{ cm}^{-1}$  belong to the parylene [159] (see also Figure 5.21), while the ones at  $1046\text{ cm}^{-1}$ ,  $1109\text{ cm}^{-1}$ , belong to the GO too and show the C-O stretching vibrations. The rest of the peaks that don't belong to the LG/parylene, belong to the GO film and they display the same vibrations mentioned for GO in the previous paragraphs. As for the parylene peaks, the more characteristic ones are those at  $820$  and  $872\text{ cm}^{-1}$  that represent the C-H bending on benzene ring, at  $1048\text{ cm}^{-1}$  that indicates the aromatic C-H bend, the one at  $1400$  displaying the C deformation, at  $1450\text{ cm}^{-1}$  corresponding to the C-H bending and the ones at  $1490$ - $1605\text{ cm}^{-1}$  indicating the C-C stretching. Finally, very important peaks are also the ones located at  $2860$ ,  $2922$ ,  $3018$  and  $3066\text{ cm}^{-1}$  displaying the aliphatic stretching of methylene groups ( $\text{CH}_2$  : C-H stretch) [159].

Finally, on the subject of **LG/silane/parylene/GO** sample, the peaks appearing at  $387\text{ cm}^{-1}$ ,  $448\text{ cm}^{-1}$ ,  $463\text{ cm}^{-1}$ ,  $576\text{ cm}^{-1}$ ,  $784\text{ cm}^{-1}$ ,  $1432\text{ cm}^{-1}$  and  $1887\text{ cm}^{-1}$  belong to the glass and the ones at  $1824\text{ cm}^{-1}$  and  $2180\text{ cm}^{-1}$  belong to silane (see also reference diagram in Figure 5.21). The peaks that belong to the parylene and GO film are mentioned in the previous paragraphs.

In the end, cross section-SEM of the films on one of the commercial glass substrates was performed in order to investigate the thickness of GO films.

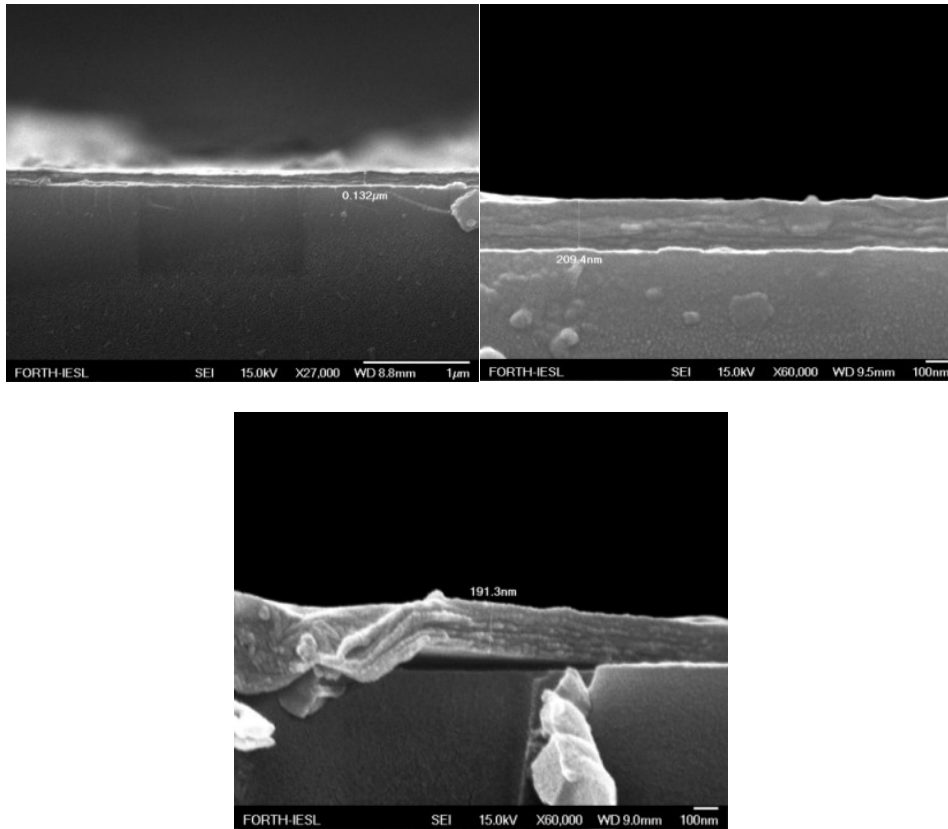


*Figure 5.22. Average thickness of GO films was about  $184 \text{ nm} \pm 45 \text{ nm}$  (measurements taken along the same sample).*

## 5.4 Optimized Laser reduction conditions

A GO film on top of glass substrate was used for the optimization of the reduction conditions. According to Wan *et al.* [143] by adjusting the laser power and scanning speed, the degree of reduction changes and tuning of the processes that take place in laser reduction can be achieved. For this reason, by keeping stable the scanning speed, different fluences were tested for the reduction of the GO, while by keeping stable the laser fluence, the GO film was reduced testing different scanning speeds. Raman mapping and electrical measurements followed in order to determine the optimum conditions for irradiation and therefore to a successful laser reduction.

### 5.4.1 Raman mapping

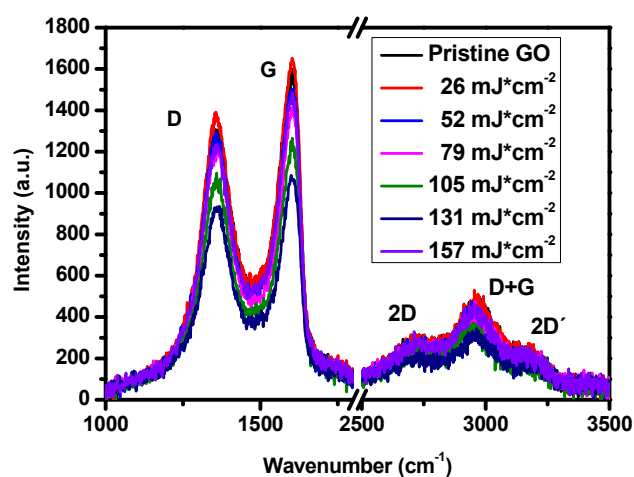
Raman spectroscopy was used in order to examine the structure and the uniformity of the GO and the reduced Graphene Oxide (rGO) films. Two measurements were taken from the non-irradiated areas (pristine GO) and four to ten measurements from the rGO produced using different fluences for mapping the irradiated GO. The  $I_D/I_G$  and the  $I_{2D}/I_G$  ratio for every measurement and an average for them were calculated for every different irradiated and non-irradiated area. The obtained spectra were baseline

corrected. All the spectra were fit with the Lorentzian peak function to obtain the peak position and the Full Width at Half Maximum (FWHM).

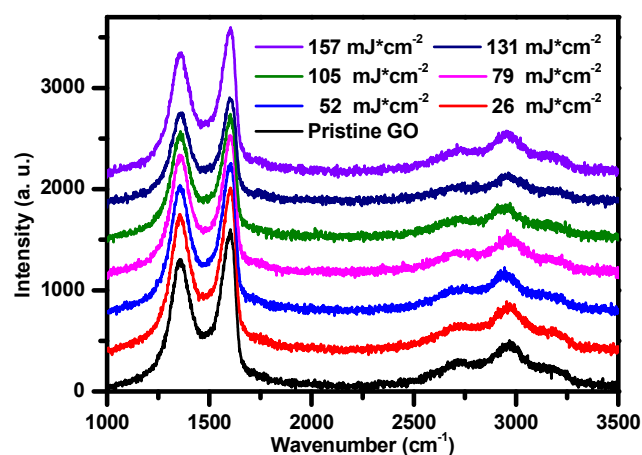
The sample labeled as TG/GO refers to the measurements from the non-irradiated areas (GO film), while the TG/rGO/3 mW, TG/ rGO/6 mW, TG/rGO/9 mW, TG/rGO/11 mW, TG/rGO/14 mW and TG/rGO/17 mW refer to the irradiated areas with different laser powers, respectively (laser power  $\pm$  0.3 mW). By TG labeling it is meant the commercial glass. The scanning speed was constant at  $500 \mu\text{m}^*\text{s}^{-1}$  and the spot size was  $15 \pm 0.8 \mu\text{m}$ . The results are shown in details in the tables 5.5 -5.7 and the graphs 5.23-5.27.

**Table 5.5.** Conditions of irradiation

Power (mW)	Corresponding Fluence ( $\text{mJ}^*\text{cm}^{-2}$ )	Spot size ( $\mu\text{m}$ )	Scanning Speed ( $\mu\text{m}^*\text{s}^{-1}$ )
Pristine TG/GO	-	-	-
TG/rGO/3	$26 \pm 0.4$	$15 \pm 0.8$	500
TG/rGO/6	$52 \pm 0.4$	$15 \pm 0.8$	500
TG/rGO/9	$79 \pm 0.4$	$15 \pm 0.8$	500
TG/rGO/11	$105 \pm 0.4$	$15 \pm 0.8$	500
TG/rGO/14	$131 \pm 0.4$	$15 \pm 0.8$	500
TG/rGO/17	$157 \pm 0.4$	$15 \pm 0.8$	500



a.



b.

*Figure 5.23. Micro-Raman spectra for pristine and irradiated GO film with different laser fluence a. Line format and b. Stack Line format.*

**Table 5.6.** Average intensity ratio of D and G band for pristine and irradiated GO films with various laser power/fluence at constant scan speed.

Fluence	AVERAGE $I_D/I_G$ ratio
Pristine TG/GO	$0.816 \pm 0.002$
TG/rGO/26 $\text{mJ} \cdot \text{cm}^{-2}$	$0.835 \pm 0.009$
TG/rGO/52 $\text{mJ} \cdot \text{cm}^{-2}$	$0.840 \pm 0.006$
TG/rGO/79 $\text{mJ} \cdot \text{cm}^{-2}$	$0.851 \pm 0.011$
TG/rGO/105 $\text{mJ} \cdot \text{cm}^{-2}$	$0.838 \pm 0.007$
TG/rGO/131 $\text{mJ} \cdot \text{cm}^{-2}$	$0.846 \pm 0.012$
TG/rGO/157 $\text{mJ} \cdot \text{cm}^{-2}$	$0.840 \pm 0.026$

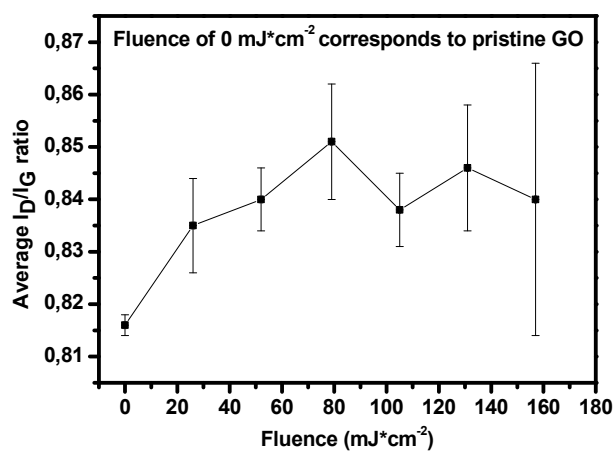


*Figure 5.24. Fluence dependent  $I_D/I_G$  ratio for pristine and irradiated GO.*

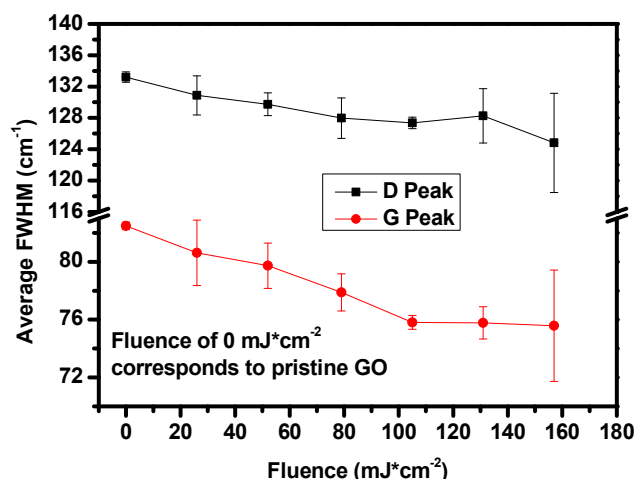


*Figure 5.25. Dependence of the D and G peaks FWHM on the laser fluence.*

The Raman spectra of pristine and irradiated GO films were recorded (Figure 5.23a and 5.23b). All spectra exhibited the characteristic peaks at  $\sim 1359$ ,  $\sim 1596$  and  $\sim 2716$   $cm^{-1}$ , corresponding to the D, G and 2D bands of GO, respectively. No significant shift in the band peak position appeared, however an intensity lowering was observed as the fluence increased, which is in agreement with the results of Ma *et al.* [39]. As the D-band is related to defects within the graphitic network [48,160], the D and G Raman intensities can be used as a measure of the size of the formed  $sp^2$  domains. In reduction processes, the  $I_D/I_G$  ratio is typically decreased due to the removal of defects, however depending on if more  $sp^2$  domains of smaller size are created after reduction, this ratio can be also increased. As shown in Figure 5.24, the  $I_D/I_G$  ratio of the irradiated areas (rGO) with different fluences is higher than the one of the pristine GO. This result agrees with the result of Zhang *et al.* [144], who found an increase in the  $I_D/I_G$  ratio of the rGO as well, said increase is associated with a smaller size of the reduced and patterned graphene domains. Furthermore, Shi *et al.* [161] mention a model about the behavior of rGO and the increase of the intensity ratio, according to which, pristine GO contains some carbon-oxygen groups that aggregate amorphously and form  $sp^3$  and  $sp^2$  domains. These  $sp^2$  domains are likened to isolated islands contained inside the  $sp^3$  domains. After reduction, these  $sp^2$  clusters do not change, however more  $sp^2$  domains of smaller size are formed, in their experiments either due to further reduction after annealing or due to the removal of carbon atoms, leading to creation of defects in the basal-plane of rGO. However, this creation of smaller sized  $sp^2$  domains results in an increased C:O ratio and higher conductivity. Thus, in this work, the progressive increasing in Raman intensity can be attributed to the removal of functional groups among GO sheets and the creation of smaller  $sp^2$  domains, which indicate the increase in ordering of amorphous carbon structures in GO [48]. Regarding Figure 5.25, a decrease in the FWHM for both the D and G band is observed with the increase of the laser fluence, as well as saturation after  $105$   $mJ*cm^{-2}$

<sup>2</sup>. This behavior is in agreement with the narrowing of the D and G bands of rGO mentioned by Trusovas *et al.* [48], assigned to structural defects created by evaporation of water molecules and other functional groups of GO at high temperatures. The overall observation of the behavior of G and D bands indicates a degree of reduction in irradiated GO films.

**Table 5.7.** Average  $I_{2D}/I_G$  ratio calculated by the  $I_{2D}/I_G$  ratio of all the ten spots from all the different fluences.

Fluence	AVERAGE $I_{2D}/I_G$ ratio
Pristine TG/GO	$0.134 \pm 0.007$
TG/rGO/26 $\text{mJ}\cdot\text{cm}^{-2}$	$0.138 \pm 0.009$
TG/rGO/52 $\text{mJ}\cdot\text{cm}^{-2}$	$0.134 \pm 0.008$
TG/rGO/79 $\text{mJ}\cdot\text{cm}^{-2}$	$0.132 \pm 0.007$
TG/rGO/105 $\text{mJ}\cdot\text{cm}^{-2}$	$0.127 \pm 0.006$
TG/rGO/131 $\text{mJ}\cdot\text{cm}^{-2}$	$0.126 \pm 0.004$
TG/rGO/157 $\text{mJ}\cdot\text{cm}^{-2}$	$0.131 \pm 0.011$

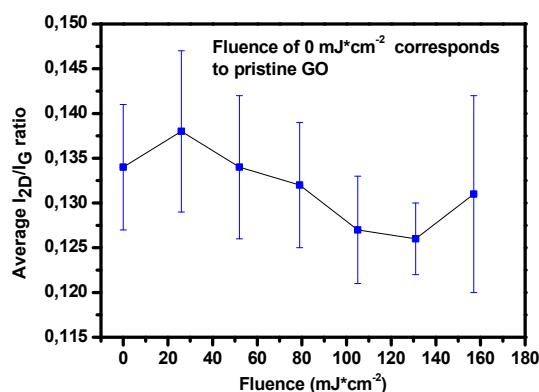


*Figure 5.26.* Dependence of the average  $I_{2D}/I_G$  ratio on fluence.

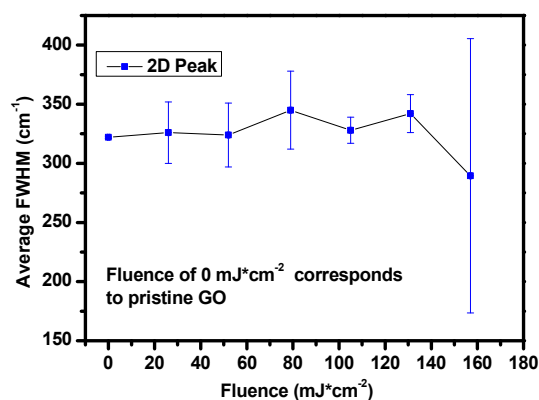


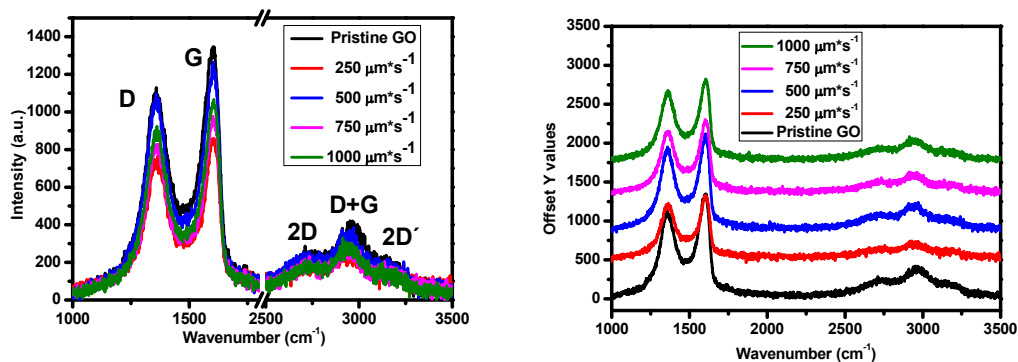
*Figure 5.27.* Dependence of the 2D peak average FWHM on laser fluence.

For the  $I_{2D}/I_G$  ratio (Figure 5.26), there is an increase for the laser irradiated area made using  $26 \text{ mJ}\cdot\text{cm}^{-2}$  and as the laser fluence increases, a decrease is observed with a possible saturation when laser fluence is greater than  $131 \text{ mJ}\cdot\text{cm}^{-2}$ . The 2D peak becomes also wider after the irradiation with  $52 \text{ mJ}\cdot\text{cm}^{-2}$  in comparison with the pristine GO and narrower after  $131 \text{ mJ}\cdot\text{cm}^{-2}$  of irradiation, seen in Figure 5.27 from the FWHM plot. According to the literature [48,162], the  $I_{2D}/I_G$  ratio should increase, due to a more graphitic structure formation, while the FWHM of the 2D peak should decrease. This narrowing can be due to the  $\text{sp}^2$  carbon reformation. A low intensity of 2D peak would be an indicator of disorders in rGO, while the FWHM of 2D is an indicator of the quality of the reduction, e.g. a reduced structure with higher or lower amount of defects [162].

A parametric study was also performed for different scanning speeds, by keeping the fluence constant at  $105 \pm 0.4 \text{ mJ}\cdot\text{cm}^{-2}$ . For the Raman characterization, two measurements were taken from the non-irradiated areas and ten measurements from the irradiated areas with different scanning speeds. Then the intensity ratios ( $I_D/I_G$  and the  $I_{2D}/I_G$ ) were calculated for each of the two-ten measurements and afterwards an average for each scanning speed was calculated as well. As in the case of different fluences, the sample labeled as TG/GO refers to the measurements from the non-irradiated areas (Pristine GO film), while the TG/rGO/ $250 \mu\text{m}\cdot\text{s}^{-1}$ , TG/rGO/ $500 \mu\text{m}\cdot\text{s}^{-1}$ , TG/rGO/ $750 \mu\text{m}\cdot\text{s}^{-1}$  and TG/rGO/ $1000 \mu\text{m}\cdot\text{s}^{-1}$  refer to the irradiated areas with different scanning speeds, respectively. The results are shown in details in the tables 5.8-5.10 and the graphs 5.28.-5.32.

**Table 5.8.** Conditions of irradiation

Scanning speed ( $\mu\text{m}\cdot\text{s}^{-1}$ )	Power (mW)	Spot size ( $\mu\text{m}$ )	Corresponding Fluence ( $\text{mJ}\cdot\text{cm}^{-2}$ )
Pristine TG/GO	-	-	-
250	$11 \pm 0.1$	$15 \pm 0.8$	$105 \pm 0.4$
500	$11 \pm 0.1$	$15 \pm 0.8$	$105 \pm 0.4$
750	$11 \pm 0.1$	$15 \pm 0.8$	$105 \pm 0.4$
1000	$11 \pm 0.1$	$15 \pm 0.8$	$105 \pm 0.4$



a.

b.

*Figure 5.28. Raman spectrum for the parametric study of different scanning speeds in a. Line and b. Stack line format.*

**Table 5.9.** Average  $I_D/I_G$  ratio calculated by the  $I_D/I_G$  ratio of all the ten spots from all the different scanning speeds

Different Scanning Speeds ( $\mu\text{m}^*\text{s}^{-1}$ )	AVERAGE $I_D/I_G$ ratio
Pristine TG/GO	$0.814 \pm 0.004$
250	$0.840 \pm 0.007$
500	$0.838 \pm 0.007$
750	$0.840 \pm 0.004$
1000	$0.832 \pm 0.005$

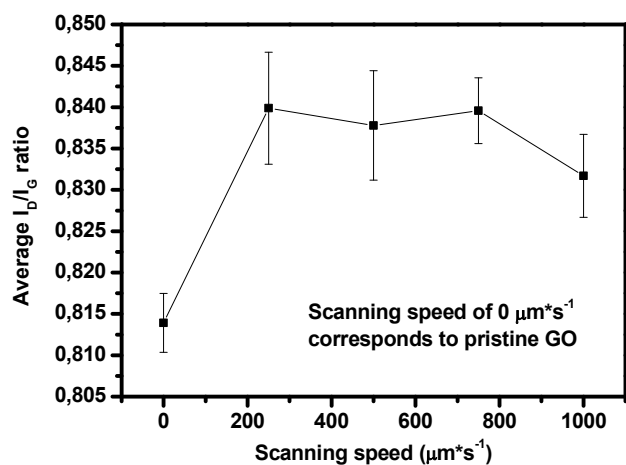


*Figure 5.29. Dependence of the average  $I_D/I_G$  ratio on the scanning speed.*

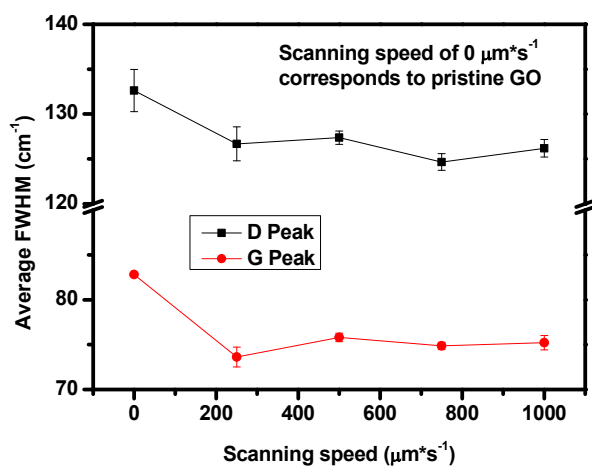


*Figure 5.30. Dependence of the D and G peaks average FWHM on scanning speed.*

In the Raman spectra (Figure 5.28), the D, G and 2D characteristic peaks are found at around  $1361$ ,  $1596$  and  $2709\text{ cm}^{-1}$ , respectively. The intensity of the G and D bands alternates from decreasing to increasing and from increasing to decreasing with the increase of the scanning speed. The  $I_D/I_G$  ratio of the irradiated areas (rGO) presented in Figure 5.29, is higher than the one of the pristine GO and increases from  $0.813$  to  $0.84$ , where it seems to have a tendency to saturate. This increase is due to the formation of smaller size of  $sp^2$  domains, which still remains an indicator of a successful reduction of GO in an amorphous environment [144,161]. Furthermore, both D and G bands become narrower (Figure 5.30), as shown in the FWHM plot, related to the  $sp^2$  carbon reformation.

**Table 5.10.** Average  $I_{2D}/I_G$  ratio calculated by the  $I_{2D}/I_G$  ratio of all the ten spots from all the different scanning speeds.

Scanning Speed ( $\mu\text{m}^*\text{s}^{-1}$ )	AVERAGE $I_{2D}/I_G$ ratio
Pristine TG/GO	$0.133 \pm 0.001$
250	$0.118 \pm 0.008$
500	$0.127 \pm 0.006$
750	$0.121 \pm 0.005$
1000	$0.120 \pm 0.003$

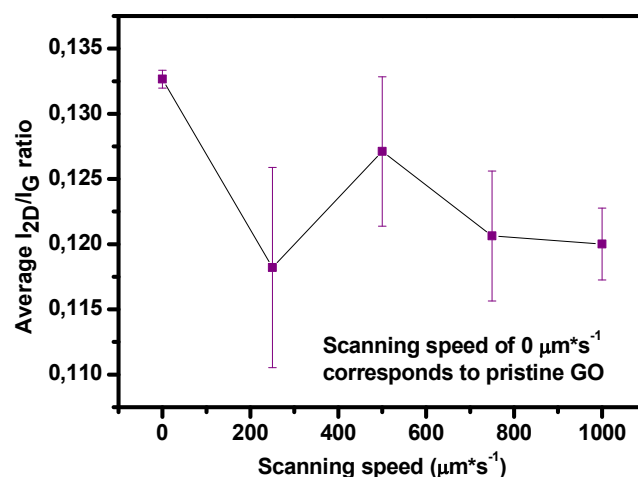


*Figure 5.31. Dependence of the average  $I_{2D}/I_G$  ratio on scanning speed.*

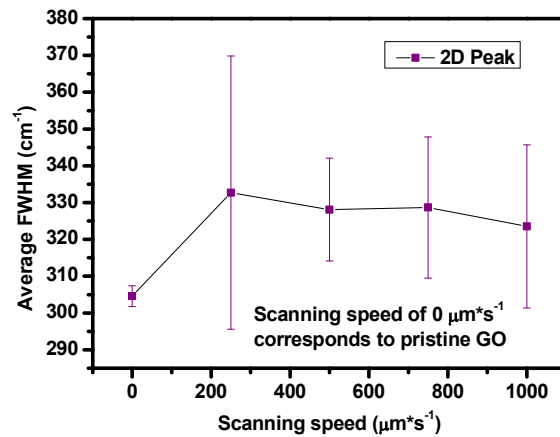


*Figure 5.32. Dependence of the 2D peak average FWHM on scanning speed.*

For the  $I_{2D}/I_G$  ratio, there is a decrease as the scanning speed increases in comparison with the pristine GO (Figure 5.31). Moreover, 2D peak is not sharp and its FWHM is increased compared to the pristine GO (Figure 5.32). According to the literature, this means that there is reduction, but in a lower degree and with a high amount of defects. This is confirmed by Shi *et al.* [161], who found a 2D peak that is almost not obvious after reduction of GO with annealing, however the electrical measurements display the successful reduction by the increase of conductivity. Furthermore, Wan *et al.* [143] who irradiated a GO film using a 780 nm femtosecond laser (70 fs pulse width and 50 MHz repetition rate), state that in their Raman experiments, a 2D peak is not appearing after laser irradiation, indicating that femtosecond reduction is localized without creating a large planar graphene sheet.

#### 5.4.2 Electrical measurements

In order to investigate the effectiveness of laser reduction on GO films with varying power/fluence, the I-V characteristics of laser irradiated samples were performed. Figure 5.33 shows the I-V characteristics of GO films. The current slope varies with the applied voltage. Further, the laser fluence strongly affects the sheet resistance of the laser irradiated GO films (Figure 5.35).

For the parametric study with different fluences the voltage used was 21 Volt for the reduced areas with  $26 \pm 0.4 \text{ mJ}\cdot\text{cm}^{-2}$ ,  $52 \pm 0.4 \text{ mJ}\cdot\text{cm}^{-2}$ ,  $79 \pm 0.4 \text{ mJ}\cdot\text{cm}^{-2}$ ,  $105 \pm 0.4 \text{ mJ}\cdot\text{cm}^{-2}$  and  $131 \pm 0.4 \text{ mJ}\cdot\text{cm}^{-2}$  and 3 Volt for the reduced area with  $157 \pm 0.4 \text{ mJ}\cdot\text{cm}^{-2}$ .

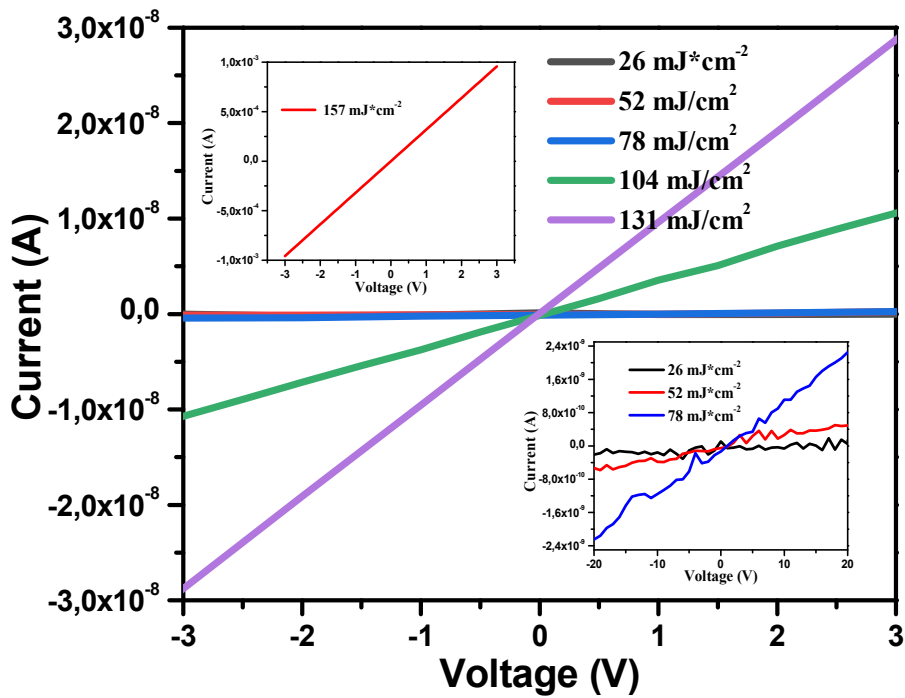


*Figure 5.33. Current-voltage characteristics of laser irradiated GO films. Inset is the I-V curve for 157  $\text{mJ}/\text{cm}^2$  (left top panel) and 26, 52 and 79  $\text{mJ}/\text{cm}^2$  (bottom right panel) laser fluence.*

From the slope of the plots it is easy to calculate the resistance for all the different fluencies. According to Ohm's law  $V = I \cdot R \rightarrow R = \frac{V}{I}$ , where R: resistance, V: voltage and I: current, by using 2 points from the plots and their coordinates for voltage and current, resistance can be found.

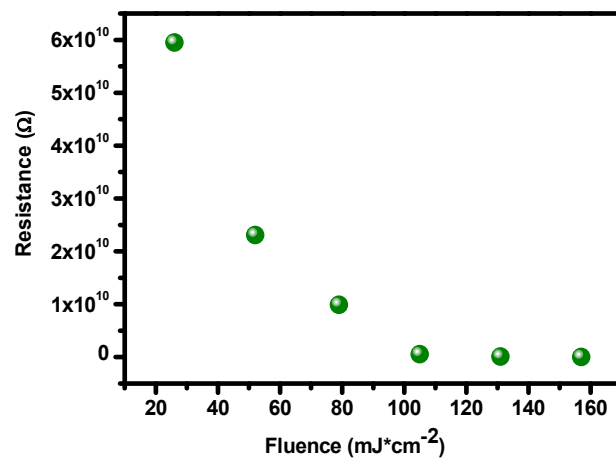


*Figure 5.34. Dependence of the resistance on laser fluence.*

**Table 5.11.** General table with Voltage, Resistance, Length, Width and Sheet Resistance values.

Fluence (mJ*cm <sup>-2</sup> )	Voltage	Resistance (KΩ)	Length (mm) ± 0.001	Width (mm) ± 0.001	Sheet Resistance (KΩ/sq)
TG/rGO/26	21 V	595×10 <sup>5</sup>	1.6	0.5	(184 ± 0.4) x 10 <sup>5</sup>
TG/rGO/52	21 V	231 ×10 <sup>5</sup>	1.5	0.5	(76 ± 0.2) x 10 <sup>5</sup>
TG/rGO/79	21 V	99 ×10 <sup>5</sup>	1.4	0.5	(36 ± 0.1) x 10 <sup>5</sup>
TG/rGO/105	21 V	6 ×10 <sup>5</sup>	1.3	0.5	(2 ± 0.005) x10 <sup>5</sup>
TG/rGO/131	21 V	1 ×10 <sup>5</sup>	1.0	0.5	(1 x10 <sup>5</sup> )± 112
TG/rGO/157	3 V	31	1.2	0.5	13 ± 0.03

According to the equation  $R = \rho \frac{L}{A} = \rho \frac{L}{W*t}$ , where R is the resistance, ρ is the resistivity, A is the cross-sectional area and L is the length. The cross-sectional area can be split into the width W and the sheet thickness t. By combining the resistivity with the thickness, the resistance can be written as  $R = \frac{\rho}{t} \frac{L}{W} = R_s \frac{L}{W}$ , where R<sub>s</sub> is the Sheet Resistance. Thus,  $R_s = R \frac{W}{L}$ . The error for sheet resistance was calculated using only the errors of length and width as, by taking only two points from the I-V curve in order to calculate the resistance, there was not known error for resistance.

Figure 5.35 represents the dependence of the rGO sheet resistance (R<sub>s</sub>), as a function of the laser fluence.

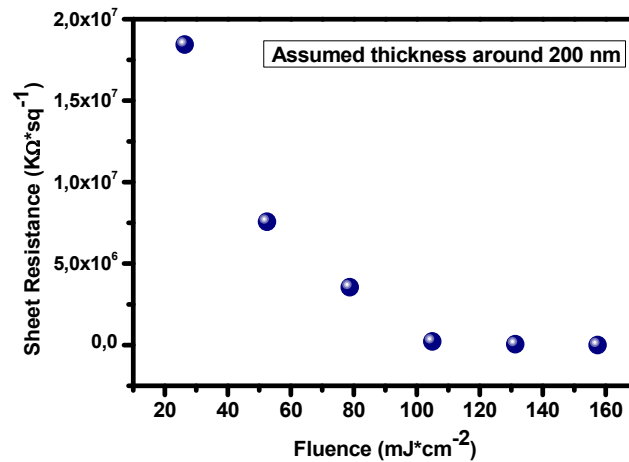


*Figure 5.35. Sheet resistance dependence on fluence.*

One can observe that the sheet resistance is reduced upon increasing laser fluence, until it reaches fluences higher than the 105 mJ\*cm<sup>-2</sup>, where it seems to saturate. The lowest sheet resistance, 13 KΩ/Sq, is obtained for the highest laser fluence and it is very close to the sheet resistance found by Kymakis et al. [49] for a 4.5-nm thick laser rGO (LrGO) film. The value of the sheet resistance calculated by their group was 18 KΩ/sq.

In order to calculate the electrical resistivity and its reverse, electrical conductivity, the equations used are  $\rho = R \frac{A}{L} = R \frac{W*t}{L}$  and  $\sigma = \frac{1}{\rho}$ . Thus, using the table 5.12 and an assumed value of about 200 nm for the thickness of the reduced film, resistivity and conductivity can be calculated.

**Table 5.12.** General table with Resistance, Length, Width, Resistivity and Conductivity values

Fluence (mJ*cm <sup>-2</sup> ) ± 0.4	Resistance (KΩ)	Length (mm) ± 0.001	Width (mm) ± 0.001	Resistivity (Ω*mm)	Conductivity (S/mm)
TG/rGO/26	595 x 10 <sup>5</sup>	1.6	0.5	(3.7 ± 1.1) x 10 <sup>6</sup>	(3 ± 0.8) x 10 <sup>-7</sup>
TG/rGO/52	231 x 10 <sup>5</sup>	1.5	0.5	(1.5 ± 0.5) x 10 <sup>6</sup>	(7 ± 2.2) x 10 <sup>-7</sup>
TG/rGO/79	99 x 10 <sup>5</sup>	1.4	0.5	(0.7 ± 0.2) x 10 <sup>6</sup>	(1 ± 0.4) x 10 <sup>-6</sup>
TG/rGO/105	6 x 10 <sup>5</sup>	1.3	0.5	(0.4 ± 0.1) x 10 <sup>5</sup>	(23 ± 6) x 10 <sup>-6</sup>
TG/rGO/131	1 x 10 <sup>5</sup>	1.0	0.5	(0.1 ± 0.03) x 10 <sup>5</sup>	(91 ± 30) x 10 <sup>-6</sup>
TG/rGO/157	31	1.2	0.5	2.6 ± 0.03	0.4 ± 0.004

As it is shown on table 5.12 the most conductive reduced GO area is produced using the highest laser fluence (157 mJ\*cm<sup>-2</sup>). It can be noticed that the conductivity of the rGO films has been increased by 6 orders of magnitude from using a laser fluence of 26 mJ\*cm<sup>-2</sup> to 157 mJ\*cm<sup>-2</sup>. However, this takes place on the sample composed by commercial glass and GO film. Such high laser fluences and powers cannot be applied to GO deposited on parylene since the substrate will be damaged.

For the parametric study with different scanning speeds the voltage used was 10 Volt for the reduced areas with speeds 250 μm\*s<sup>-1</sup>, 500 μm\*s<sup>-1</sup>, 750 μm\*s<sup>-1</sup> and 1000 μm\*s<sup>-1</sup>. The results are shown in details in the tables 5.13-5.14 and the graphs 5.36.-5.38.

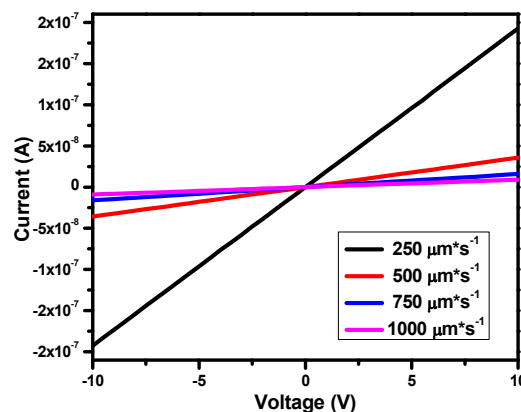


*Figure 5.36. I-V measurements for the parametric study with different scanning speeds.*

From the slope of the plots it is easy to calculate the resistance for all the different speeds.

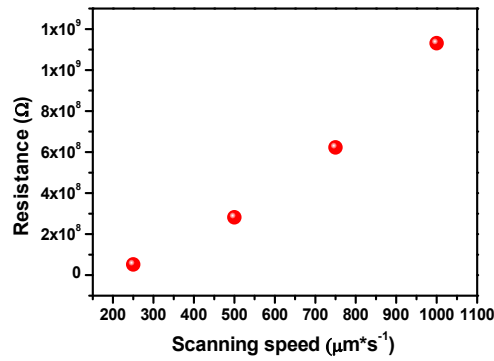


Figure 5.37. Dependence of the resistance (ohms) on the different scanning speeds.

Table 5.13. Summary table of Voltage, Resistance, Length, Width and Sheet Resistance values of rGO films.

Scanning speed ( $\mu\text{m}\cdot\text{s}^{-1}$ )	Voltage	Resistance ( $\text{K}\Omega$ )	Length (mm) $\pm 0.001$	Width (mm) $\pm 0.001$	Sheet Resistance ( $\text{K}\Omega / \text{sq}$ )
250	10 V	$5 \times 10^4$	1.2	0.5	$(2 \pm 0.005) \times 10^4$
500	10 V	$28 \times 10^4$	1.3	0.5	$(1 \pm 0.001) \times 10^5$
750	10 V	$62 \times 10^4$	1.6	0.5	$(2 \pm 0.004) \times 10^5$
1000	10 V	$113 \times 10^4$	1.4	0.5	$(4 \pm 0.009) \times 10^5$

As mentioned in previous paragraphs as well, according to the equation  $R = \rho \frac{L}{A} = \rho \frac{L}{W \cdot t}$  and by combining the resistivity with the thickness, the sheet resistance can be written as  $R_s = R \frac{W}{L}$ . The error for the sheet resistance is also calculated as mentioned in previous paragraphs.

Figure 5.38 represents the dependence of the rGO sheet resistance,  $R_s$ , as a function of the scanning speed.

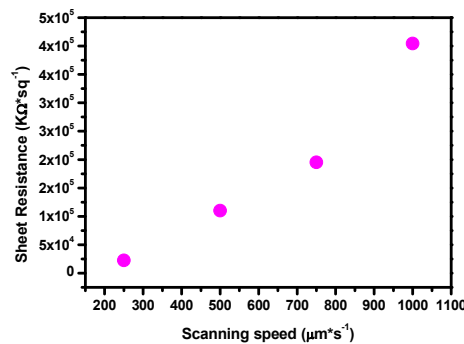


Figure 5.38. Sheet resistance for various speeds.

It can be noticed that for constant incident fluence/laser power, the sample's sheet resistance increases upon increasing the scanning speed (see Figure 5.38).

**Table 5.14.** General table with Resistance, Length, Width, Resistivity and Conductivity values

Scanning speeds ( $\mu\text{m}^*\text{s}^{-1}$ )	Resistance ( $\text{K}\Omega$ )	Length (mm) $\pm 0.001$	Width (mm) $\pm 0.001$	Resistivity ( $\Omega^*\text{mm}$ )	Conductivity (S/mm)
250	$5.2 \times 10^4$	1.2	0.5	$4333 \pm 1300$	$(2 \pm 0.7) \times 10^{-4}$
500	$28.2 \times 10^4$	1.3	0.5	$21692 \pm 6508$	$(0.5 \pm 0.1) \times 10^{-4}$
750	$62.3 \times 10^4$	1.6	0.5	$38938 \pm 11682$	$(0.3 \pm 0.07) \times 10^{-4}$
1000	$113.1 \times 10^4$	1.4	0.5	$80786 \pm 24236$	$(0.1 \pm 0.04) \times 10^{-4}$

As the table 5.14 shows, the most conductive reduced area is the one produced with the slowest scanning speed resulting to more effective reduction. This is also visible from the I-V plots and sheet resistance plots. The conductivity is increased by one order of magnitude by using a speed of  $250 \mu\text{m}^*\text{s}^{-1}$ . Literature also confirms that the lowest scanning speed increases the efficiency of reduction [48, 143] as GO is heated to higher temperatures [48].

#### 5.4.3 Optimization of the lower laser fluences

The first parametric study for fluences was carried out in order to estimate which is the range of the fluence values for which this study shall focus on. After optimizing the scanning speeds and realizing that with a  $15 \mu\text{m}$  spot and high fluences there is a high possibility of burning or destroying both the GO film and the parylene substrate, it was decided to defocus and increase the spot size from  $\sim 15 \mu\text{m}$  to  $\sim 30 \mu\text{m}$ . The optimum fluences to use on top of sensitive substrates, according to the previous parametric study for fluences, were the lower ones, between  $26$  and  $79 \text{mJ}^*\text{cm}^{-2}$  and therefore, a new parametric study with fluences between these values took place. Laser reduced graphene oxide (LrGO) rectangles were fabricated by using fluences of  $26$ ,  $39$ ,  $52$  and  $79 \text{mJ}^*\text{cm}^{-2}$ , a spot size  $\sim 30 \mu\text{m}$  and a scanning speed of  $250 \mu\text{m}^*\text{s}^{-1}$ . An intermediate laser fluence of  $39 \text{mJ}^*\text{cm}^{-2}$  was also added as the spray coating machine was homemade and the thickness of the produced films was not uniform. As such, sometimes the higher fluences were giving ablated results instead of a reduction. Therefore, in such a case there was a need to have at least two fluences to compare for this new parametric study.

Raman spectra of pristine and irradiated GO films were recorded. In Figure 5.39 the Raman spectra obtained from pristine GO and LrGO samples are shown. The spectra of GO featured the characteristic peaks at  $\sim 1364 \text{cm}^{-1}$ ,  $\sim 1590 \text{cm}^{-1}$ ,  $\sim 2723 \text{cm}^{-1}$ ,  $\sim 2952 \text{cm}^{-1}$  and  $\sim 3172 \text{cm}^{-1}$ , which correspond to the D, G, 2D, D+G and 2D' bands of the GO, respectively. All the Raman band peak positions were determined by Lorentzian

function fitting. The Raman spectra of LrGO displayed characteristic peaks at an average position of  $\sim 1364\text{ cm}^{-1}$ ,  $\sim 1595\text{ cm}^{-1}$ ,  $\sim 2716\text{ cm}^{-1}$ ,  $\sim 2960\text{ cm}^{-1}$  and  $\sim 3164\text{ cm}^{-1}$ , corresponding to D, G, 2D, D+G and 2D' bands, respectively for the rectangles made using 26, 39 and 52  $\text{mJ}\cdot\text{cm}^{-2}$ . For the rectangle produced using 79  $\text{mJ}\cdot\text{cm}^{-2}$  fluence there are no rGO characteristic peaks, but a peak around  $1100\text{ cm}^{-1}$ , which corresponds possibly to the glass substrate [163]. A possible explanation for this rectangle is that a lot of material has been removed due to ablation and the Raman beam can detect the glass substrate underneath.

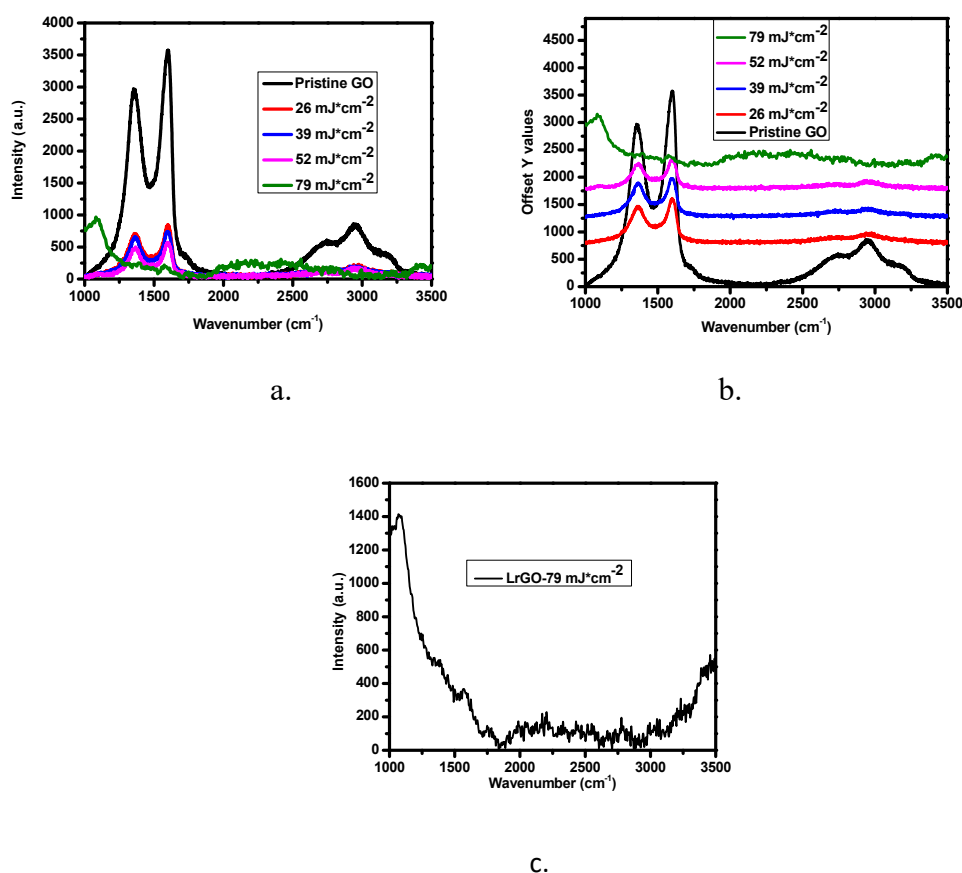
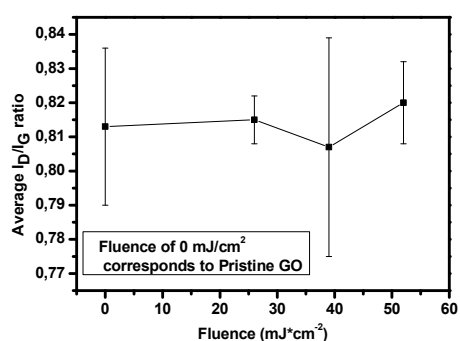


*Figure 5.39. Raman spectra of GO and LrGO areas on glass substrate in a) Line and b) Stack line format and c) separate Raman spectrum of LrGO area produced using 79  $\text{mJ}\cdot\text{cm}^{-2}$  fluence.*

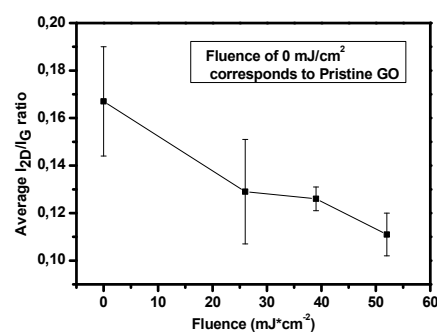
The intensity ratio of D and G bands ( $I_D/I_G$ ) is used as a measure of the size of  $\text{sp}^2$  domains in a network of  $\text{sp}^3$  and  $\text{sp}^2$  bonded carbon atoms. Table 5.15 represents the values obtained from the Raman spectra of pristine and irradiated GO. The rectangles made using 79  $\text{mJ}\cdot\text{cm}^{-2}$  is not shown here due to detection of only the glass substrate and not of any peaks from graphene oxide or reduced graphene oxide.

**Table 5.15.** Average ratios and FWHM of Lorentzian fitted results for D, G and 2D bands.

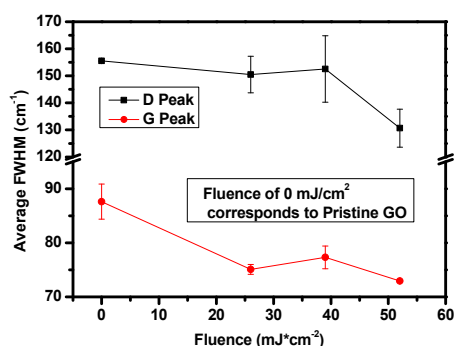
	$(I_D/I_G)$ Average	$(I_{2D}/I_G)$ Average	(D FWHM) Average	(G FWHM) Average	(2D FWHM) Average
<b>Pristine GO</b>	$0.813 \pm 0.023$	$0.167 \pm 0.023$	$155 \pm 0.2$	$88 \pm 3$	$363 \pm 46$
<b>LrGO-26</b> $\text{mJ} \cdot \text{cm}^{-2}$	$0.815 \pm 0.007$	$0.129 \pm 0.022$	$151 \pm 7$	$75 \pm 1$	$616 \pm 116$
<b>LrGO-39</b> $\text{mJ} \cdot \text{cm}^{-2}$	$0.807 \pm 0.032$	$0.126 \pm 0.005$	$153 \pm 12$	$77 \pm 2$	$471 \pm 32$
<b>LrGO-52</b> $\text{mJ} \cdot \text{cm}^{-2}$	$0.820 \pm 0.012$	$0.111 \pm 0.009$	$131 \pm 7$	$73 \pm 0.3$	$530 \pm 44$



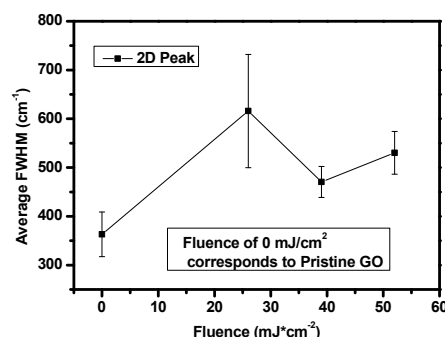
a.



b.



c.



d.

*Figure 5.40. a) Intensity ratio of D and G bands for GO and rectangles produced using 26, 39 and 52  $\text{mJ} \cdot \text{cm}^{-2}$ , b) Intensity ratio of 2D and G bands for GO and rectangles made utilizing 26, 39 and 52  $\text{mJ} \cdot \text{cm}^{-2}$ , c) FWHM for D and G bands for GO and rectangles produced using 26, 39 and 52  $\text{mJ} \cdot \text{cm}^{-2}$  and d) FWHM for D and G bands for GO and rectangles made utilizing 26, 39 and 52  $\text{mJ} \cdot \text{cm}^{-2}$ .*

After laser reduction, the  $I_D/I_G$  ratio remains almost at the same levels with a tendency to increase, while a decrease in the irradiated area with a fluence of 39  $\text{mJ} \cdot \text{cm}^{-2}$  appears. This indicates that in this specific fluence there is a higher amount of

removal of defects than the irradiated areas produced using other fluences, which can be an indicator of a successful reduction as the D peak is associated with the disorders and the G band indicates the  $E_{2g}$  vibration mode of  $sp^2$  carbon domains. Furthermore, the FWHM of the D and G peaks show a narrowing after reduction, while the FWHM of the 2D peak is increasing after the laser treatment. The absence of an intense and strong 2D band after laser irradiation is not an optimal result; however the possibility of sufficient laser reduction with a lower degree of graphitization [44] and consequently the increase of conductivity cannot be excluded. Ma *et al.* [39] mentioned that after laser irradiation at 532 nm a long and sharp 2D peak does not appear in the Raman characterizations, however the conductivity of their rGO film had increased dramatically after the laser treatment, displaying a sufficient reduction. It is also worth mentioning the fact that the FWHM of 2D peak of the rectangle made utilizing  $39 \text{ mJ}\cdot\text{cm}^{-2}$  is lower compared to the FWHM of 2D peaks of the rectangles made using 26 and  $52 \text{ mJ}\cdot\text{cm}^{-2}$  and therefore, it shows that in this fluence a more narrow and sharp 2D peak appears. Moreover, the intensity ratio of the 2D and G bands decrease in general when compared to the intensity ratio of the 2D and G bands of GO. However, from all the irradiated areas with different fluences the one irradiated with  $39 \text{ mJ}\cdot\text{cm}^{-2}$  is higher than the ratios of the areas irradiated utilizing other fluence values, especially as the  $I_{2D}/I_G$  ratio of  $26 \text{ mJ}\cdot\text{cm}^{-2}$  has a large standard deviation. Consequently, the intermediate fluence shows a more intense and strong 2D band, which is an indicator of more crystallization. This result is in agreement with the literature [48], as it is mentioned that medium laser power/fluence gives a more than sufficient reduction. This is a consequence of the smooth laser lines on the samples due to the medium laser fluence, which are smoother than these of the high fluence. Simultaneously, low laser fluence leads to smooth but irregular lines. As the overlapping of the scribing lines is important for the achievement of an efficient reduction, the medium laser fluence is the optimum one. In this work, the medium laser fluence of  $39 \text{ mJ}\cdot\text{cm}^{-2}$  seems to be the best one for irradiation according to Raman spectroscopy; however more characterizations are needed for the indication of a sufficient reduction.

For this reason, the field emission scanning electron microscope (FE-SEM) was used to acquire the cross-sectional view of spray gun coated GO and LrGO films. Figure 5.41a represents the cross-sectional view of a GO film on glass substrate. The average thickness of the GO film is  $190 \pm 45 \text{ nm}$  (average value measured using the thickness values from 12 different locations along the length of the film). Figure 5.41b,c show the cross-sectional view of a LrGO film on glass substrate irradiated with 39 and  $52 \text{ mJ}\cdot\text{cm}^{-2}$ , respectively. The average thickness of the LrGO area fabricated utilizing  $39 \text{ mJ}\cdot\text{cm}^{-2}$  is  $76 \pm 20 \text{ nm}$  (average value measured using the thickness values from 16 different locations along the length of the reduced area) and the average thickness of the LrGO area fabricated using  $52 \text{ mJ}\cdot\text{cm}^{-2}$  is  $56 \pm 20 \text{ nm}$  (average thickness measured by using values from 17 different locations along the length of the reduced

area). The thickness of the LrGO films created with fluences of 26 and 79  $\text{mJ}\cdot\text{cm}^{-2}$  was not easily measurable, especially for the  $\text{mJ}\cdot\text{cm}^{-2}$ , which in the end, was not acquired. The value of 26  $\text{mJ}\cdot\text{cm}^{-2}$  is not a very high fluence value and therefore the thicknesses of the irradiated area and of the pristine GO can be similar. Hence, as the GO film is also not uniform it is more difficult to distinguish if any small difference in thickness is due to the reduction or due to the non-uniformity of the film. However, for the rectangle irradiated with 79  $\text{mJ}\cdot\text{cm}^{-2}$ , only some areas on the reduced film were measured and from these areas the average calculated thickness was at about  $42 \pm 16$  nm (average thickness measured by using values from 7 different locations along the length of the reduced area) (Figure 5.41d). All these thickness results are in agreement with the work of Wan *et al.* [143], who stated that in their experiments, by irradiating with higher laser fluences the thickness of the rGO film is decreased, reaching up to 80% of its original thickness.

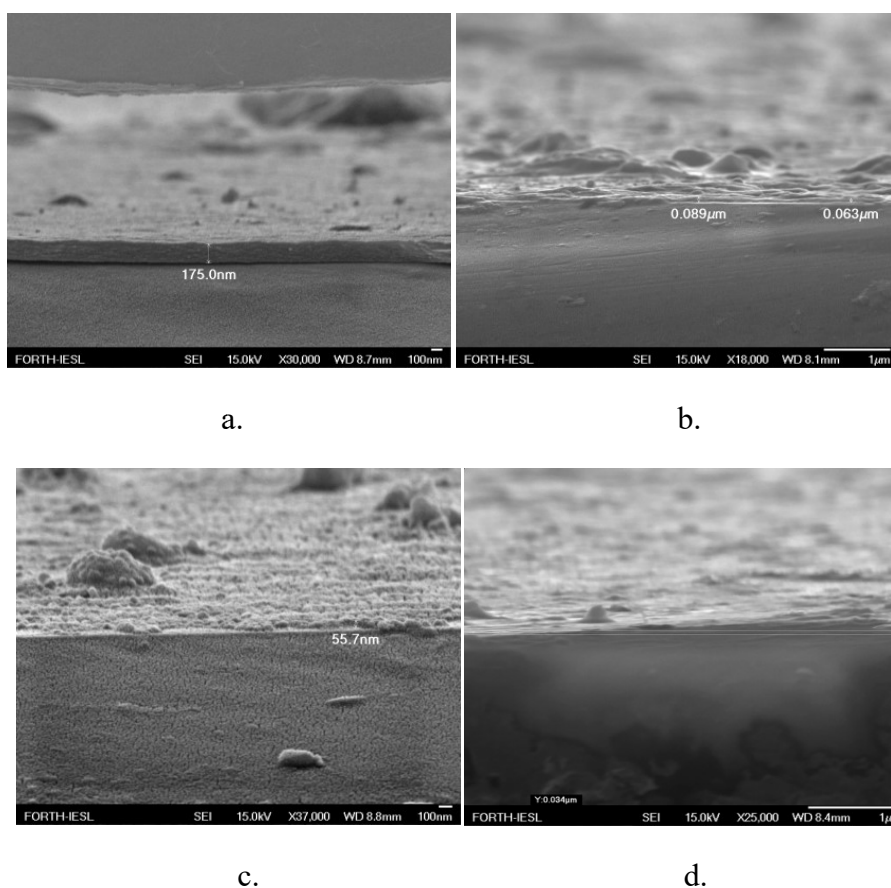


*Figure 5.41. Cross-sectional view of a) GO film on glass substrate, b) LrGO film irradiated with 39  $\text{mJ}\cdot\text{cm}^{-2}$  on glass substrate, c) LrGO film produced using 52  $\text{mJ}\cdot\text{cm}^{-2}$  and d) LrGO film fabricated utilizing 79  $\text{mJ}\cdot\text{cm}^{-2}$  on glass substrate.*

Electrical characterization of the laser reduced area and the recording of the I-V measurements were performed, in order to investigate the effectiveness of laser reduction on GO film. Figure 5.42a shows the current-voltage (I-V) characteristics of LrGO areas and Figure 5.42b displays the calculated sheet resistance.

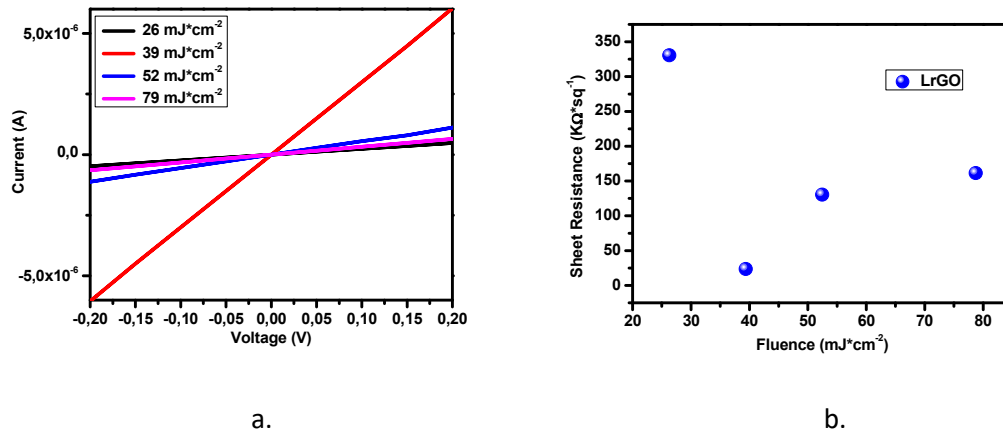


Figure 5.42. a) Current-voltage characteristics of laser irradiated GO films made using different fluences on top of commercial glass substrate and b) Sheet resistance calculated for the laser irradiated GO areas with different fluences on top of glass substrate

To calculate sheet resistance, the thickness of the LrGO films is needed, in order to be used in the equation  $R_s = \rho/t$ , where  $\rho$ : resistivity and  $t$ : thickness. However, as the thickness of the fluences of  $26 \text{ mJ} \cdot \text{cm}^{-2}$  was not acquired, another equation for the calculation of sheet resistance will be used.  $R_s = (R \cdot W)/L$ , where  $R$ : Resistance,  $W$ : Width and  $L$ : Length of the rectangles made (Table 5.16).

Table 5.16. Resistance and Sheet Resistance values for pristine GO and LrGO areas.

Fluence ( $\text{mJ} \cdot \text{cm}^{-2}$ ) $\pm 0.4$	Resistance ( $\text{K}\Omega$ )	Width (mm) $\pm 0.001$	Length (mm) $\pm 0.001$	Sheet Resistance ( $\text{K}\Omega/\text{sq}$ )
Pristine GO	-	-	-	$\sim 10^9$ [164]
26	415	1	1.3	$331 \pm 0.4$
39	33	1	1.4	$23 \pm 0.03$
52	179	1.5	2.1	$130 \pm 0.1$
79	308	1	1.9	$161 \pm 0.2$

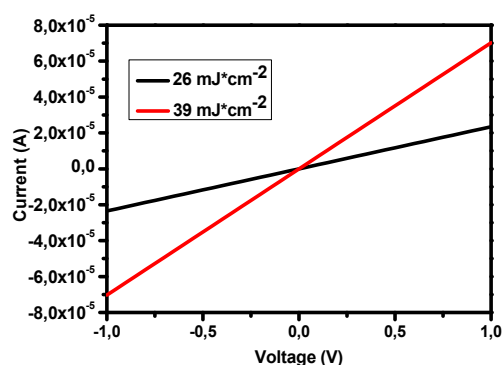
Figure 5.42a displays linear I-V curves for all the fluences, however the fluence of  $39 \text{ mJ} \cdot \text{cm}^{-2}$  is the most conductive (see Figure 5.42a and Table 5.16, Resistance column that is calculated directly from the I-V curves through the Ohm's law  $R = V/I$ , where  $R$ : Resistance,  $V$ : Voltage and  $I$ : Current). Furthermore, the comparison between the sheet resistance value for pristine GO [164] and the sheet resistance values for LrGO areas show a significant decrease for the laser irradiated areas (Table 5.16 and Figure 5.42b). Therefore, the I-V characteristics prove the successful laser reduction and conductivity of the electrodes for the fluence of  $39 \text{ mJ} \cdot \text{cm}^{-2}$ , as the lowest sheet resistance and therefore the highest conductivity is achieved.

Furthermore, there was the need to find out whether the fluence of  $39 \text{ mJ} \cdot \text{cm}^{-2}$  was the optimum fluence not only for GO reduction on top of glass but also on top of glass with parylene substrate. Thus, new rectangles were created on top of glass/parylene/GO substrates made by 26 and  $39 \text{ mJ} \cdot \text{cm}^{-2}$ . The higher fluences of 52

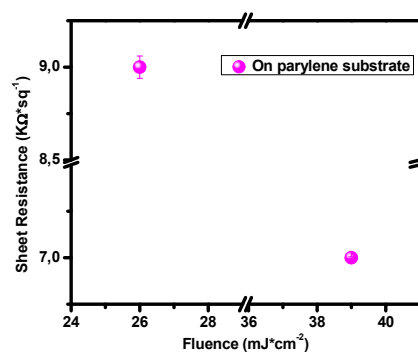
and  $79 \text{ mJ}\cdot\text{cm}^{-2}$  were not used in this case as it was observed that even with just  $52 \text{ mJ}\cdot\text{cm}^{-2}$  the GO film was partially reduced and partially ablated. This is possibly due to the non uniformity of the parylene film as well, which makes the successful reduction even more difficult in this substrate. After the creation of the rectangles using the fluences of  $26$  and  $39 \text{ mJ}\cdot\text{cm}^{-2}$ , electrical characterization followed, in order to investigate the effectiveness of laser reduction on GO film on top of parylene substrate. The average thickness of the rectangle irradiated with  $26 \text{ mJ}\cdot\text{cm}^{-2}$  was not obtained but assumed to be around  $200 \text{ nm}$  (average thickness of the pristine GO), in order to be able to calculate the sheet resistance.

**Table 5.17.** Comparison of the I-V results on different fluences on parylene substrate.

Fluence ( $\text{mJ}\cdot\text{cm}^{-2}$ ) $\pm 0.4$	Voltage (Volt)	Resistance ( $\text{K}\Omega$ )	Length (mm) $\pm 0.01$	Width (mm) $\pm 0.01$	Average Thickness (nm)	Resistivity ( $\Omega\cdot\text{mm}$ )	Sheet Resistance ( $\text{K}\Omega/\text{sq}$ )
26	1	42.7	2.4	0.5	$200 \pm 60$	$1.8 \pm 0.5$	$9 \pm 0.06$
39	1	17.5	3.8	1.5	$76 \pm 20$	$0.5 \pm 0.1$	$7 \pm 0.005$



a.



b.

*Figure 5.43. a) Current-voltage characteristics of laser irradiated GO films with different fluences on top of LiU glass with parylene on top substrate and b) Sheet resistance calculated for the laser irradiated GO areas made using different fluences on top of the same parylene substrate.*

As shown in Figure 5.43a,b the highest conductivity and thus the lowest sheet resistance appears with the fluence of  $39 \text{ mJ}\cdot\text{cm}^{-2}$  on top of parylene substrate as well. Therefore, this is the fluence with which the electrodes will be created both on glass and parylene substrates.

However, despite the optimization of the fluences both on glass and glass/parylene substrate, it should be noted that, in the irradiated areas of GO on top of parylene

some formations that looked like bubbles were visible using optical microscopy (Figure 5.44).



*Figure 5.44. Formations that look like bubbles on top of irradiated LG/parylene/GO films. The darker parts at the left and right corners are the silver paste placed for the electrical measurements.*

According to Ortigoza-Diaz *et al.* [165], working with parylene can be sometimes challenging due to its thermoplastic nature as a polymer. In high heat and irradiation exposure, parylene can be heated and, due to its low thermal threshold, to appear bubbles and cracks on its surface or even to be burnt.

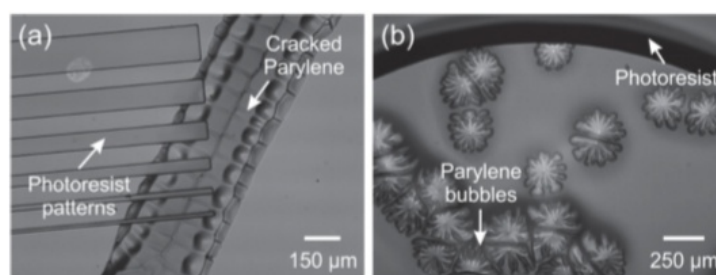


*Figure 5.45. Parylene a) cracked due to high heat and b) with bubbles during heating after exposure to UV-light [164].*

For this reason, an experiment was held in order to identify the cause of the creation of these formations that look like bubbles. As these configurations were observed only on the rGO samples on top of glass-parylene substrates and not on the rGO on top of glass as substrate, initially it was assumed that they were formed due to parylene. Therefore, a parylene-C sample on top of glass was irradiated with fluences lower ( $26 \text{ mJ}\cdot\text{cm}^{-2}$ ) than, same ( $39 \text{ mJ}\cdot\text{cm}^{-2}$ ) as and higher ( $52 \text{ mJ}\cdot\text{cm}^{-2}$ ) than the optimum laser fluence for the fabrication of the electrodes. However, there were no formations at all in the irradiated parylene areas. This result indicates that the explanation for the development of configurations like bubbles, might lay in the molecular coexistence of parylene with GO after laser irradiation and reduction. Golda-Cepa *et al.* [166] in their review paper stated that depending on the fabrication procedure, parylene-C can have imperfections either as a coating on top of different types of materials or as a substrate coated by another material. This is a consequence of its difficult adhesion to materials in general. According to Huang *et al.* [167], some properties of graphene such as flexibility and impermeability, especially for gas

molecules [168], can comfort the formation of bubbles on graphene sheets. More precisely, they observed the presence of bubbles, due to adsorbed molecules on the SiO<sub>2</sub> substrate, which evaporate after laser heating. The origin of such kind of bubbles is not known yet. Meanwhile Georgiou *et al.* [169] comment on the probability of air and hydrocarbon residuals trapped between graphene sheet and their silicon substrate, while Ramirez-Jimenez *et al.* [170] mention that, as they used Cu as a catalyst agent in the chemical vapor deposition of graphene, the bubbles they observe are formed due to the inhomogeneous Cu oxidation, producing discontinuous Cu<sub>2</sub>O films that trap the atmospheric molecules with the impermeable graphene sheets. Another possible explanation could be that, during the fabrication procedure of parylene and of its deposition on top of glass substrate, there were some water or air molecules trapped in this specific bunch of parylene substrates, as there were also some irradiated parylene/GO samples without the presence of any specific formation.

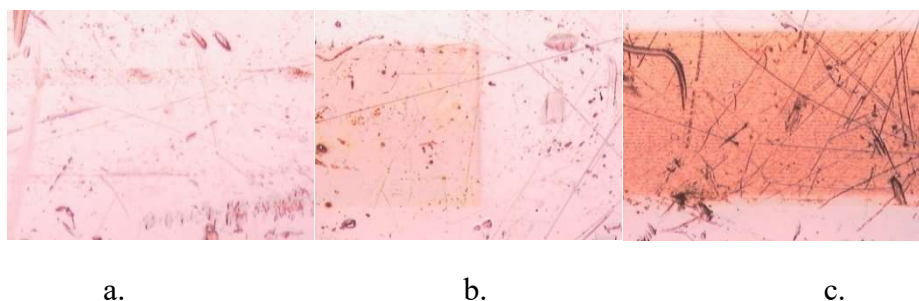


*Figure 5.46. Parylene irradiated with fluence a) 26 mJ\*cm<sup>-2</sup>, b) 39 mJ\*cm<sup>-2</sup> and c) 52 mJ\*cm<sup>-2</sup>. Formations that look like bubbles didn't appear in any of the irradiated areas.*

As these formations looked like bubbles but there was no certainty that they are bubbles indeed and as in the parylene substrates no such configurations were formed after direct laser irradiation on top of them, the rectangles made using 26 and 39 mJ\*cm<sup>-2</sup>, already used for the electrical measurements, were also used for FE-SEM microscopy.

For GO non-irradiated areas, the non uniformity of the film was confirmed due to the existence of some irregularities on top of GO surface. These irregularities look like incorporated particles or like bumps (Figure 5.47a,b).

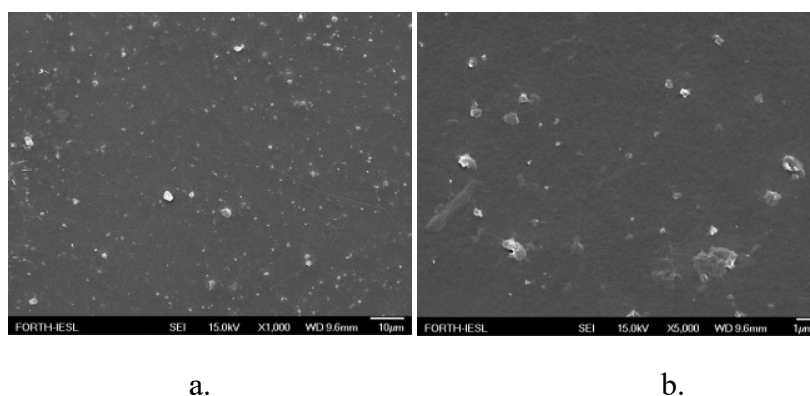


*Figure 5.47. Irregularities on top of GO film confirming its non- uniformity.*

EDS analysis was performed and it showed that C, O, Cl, Si, Ca, Na, Mg and Au were the detected elements (Figure 5.48). C and O are due to the GO film (carbon and carbonyl-, carboxyl-, hydroxyl-groups), while the Cl is due to the parylene underneath GO. However, the EDS also displayed the elements that belong to the glass substrate (Si, Ca, Na, and Mg) (Figure 5.49). The penetration depth of the EDS analysis depends strongly on how heavy an element is (its atomic number). As all the elements that belong to GO and parylene are not heavy that means that the EDS can penetrate further and detect the glass as well. Finally, Au is due to the sputtering performed before the FE-SEM microscopy and EDS analysis in order to avoid the charging of the material inside the microscope.

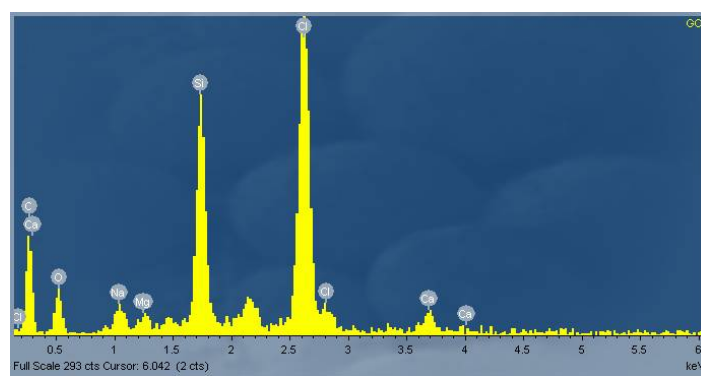


*Figure 5.48. EDS analysis for non-irradiated GO film.*

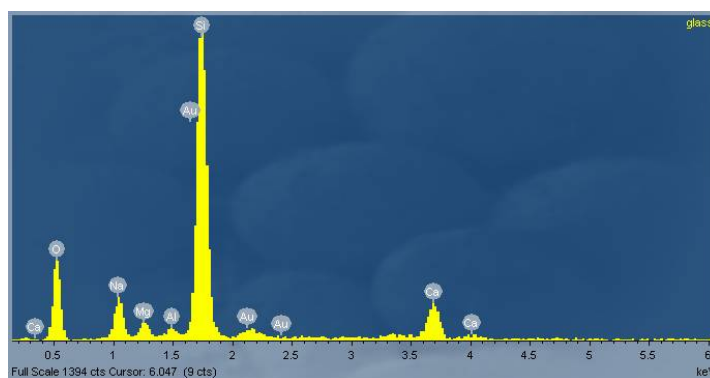


*Figure 5.49. EDS analysis for glass substrate.*

EDS took also place for the bumps that exist on top of GO film. According to the elemental analysis, carbon and functional groups of GO film are detected, with a high intensity peak for oxygen, while parylene (Cl) and a bit of glass (Si) are also indicated in the spectrum. In comparison with the spectrum 2 of the flat GO surface (Figure 5.50a,b) the glass is the only thing detected more than that on the bumps as the beam beam has less material to penetrate. However, oxygen intensity peak is lower on the flat surface than on the bumps, displaying that the bumps are oxygen containing groups.

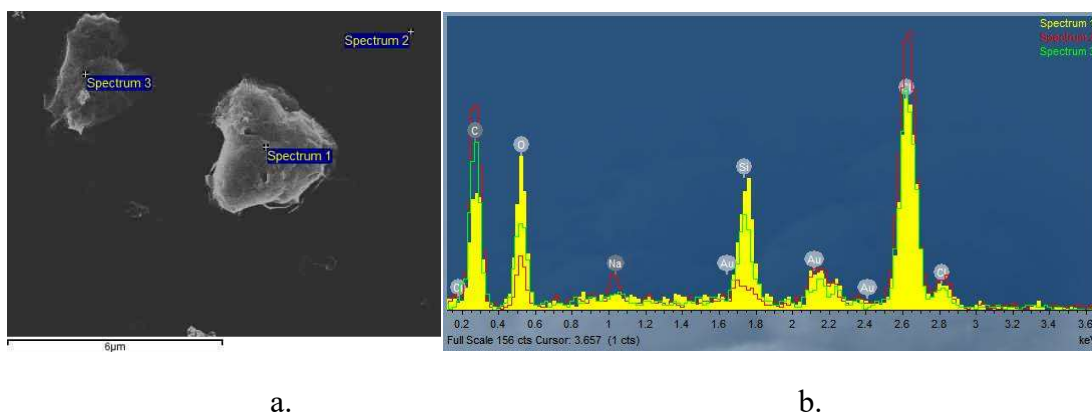


*Figure 5.50. EDS analysis of GO film and of the bumps on top of its surface.*

For rGO irradiated area with  $26 \text{ mJ} \cdot \text{cm}^{-2}$ , the irregularities mentioned above seem to be removed by the laser irradiation, resulting in some flakes and holes in the rGO film (Figure 5.51a). Therefore, the formations that looked like bubbles are possibly the holes created after the removal of the bumps by laser irradiation. Figure 5.51b represents the interface between the non-irradiated (bottom) and the irradiated area with  $26 \text{ mJ} \cdot \text{cm}^{-2}$  (top), displaying the irregularities on the GO film (bottom) and the removed bumps with their holes on the irradiated area (top). The laser reduced area appears brighter than the GO area in SEM images, due to the high amount of the emitted secondary electrons [143].

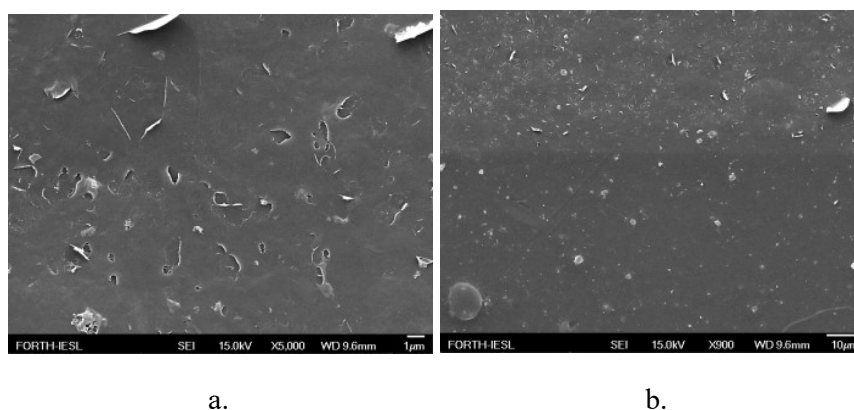


*Figure 5.51. a) Reduced Graphene oxide flakes and holes possibly created by the removal of the bumps of the GO film after the laser irradiation with  $26 \text{ mJ} \cdot \text{cm}^{-2}$ . This indicates that the surface is discontinuous in some places and b) Interface between the rGO (top) and GO (bottom) film.*

For the irradiated areas with the lowest fluence, EDS spectrum (Figure 5.52) displayed peaks that correspond to the elements of C, O, Cl, Si, Ca, Na, Mg and Au. C and O are due to the GO film, however it is worth mentioning the fact that the peak of the detected oxygen is decreased and therefore this is a sign of reduction. The rest of the peaks belong to parylene and glass substrate as mentioned in the previous paragraph, while gold is due to the sputtering procedure.

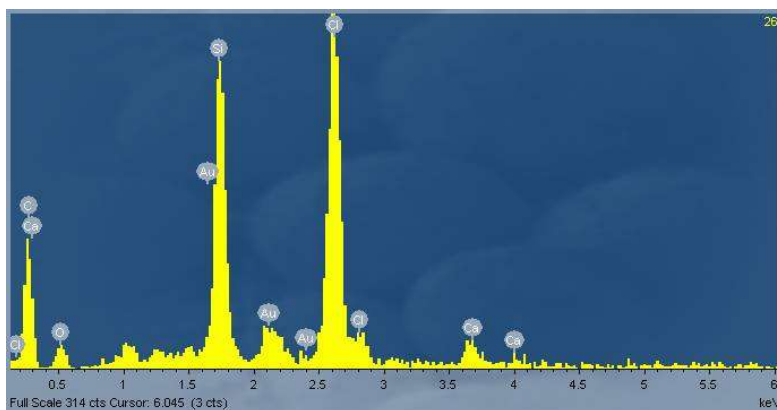


*Figure 5.52. EDS analysis for irradiated GO film with 26 mJ\*cm<sup>-2</sup>.*

For the rGO irradiated area with 39 mJ\*cm<sup>-2</sup> the irregularities seem to be removed by the laser irradiation, but it looks like this higher laser fluence has softened the rGO surface, resulting in no flakes and less holes on the rGO film, as it is confirmed by Figure 5.53a and the interface image (Figure 5.53b). The fact that this film is not as discontinuous as the rGO film produced using 26 mJ\*cm<sup>-2</sup> may be one of the reasons for higher electrical conductivity measurements.

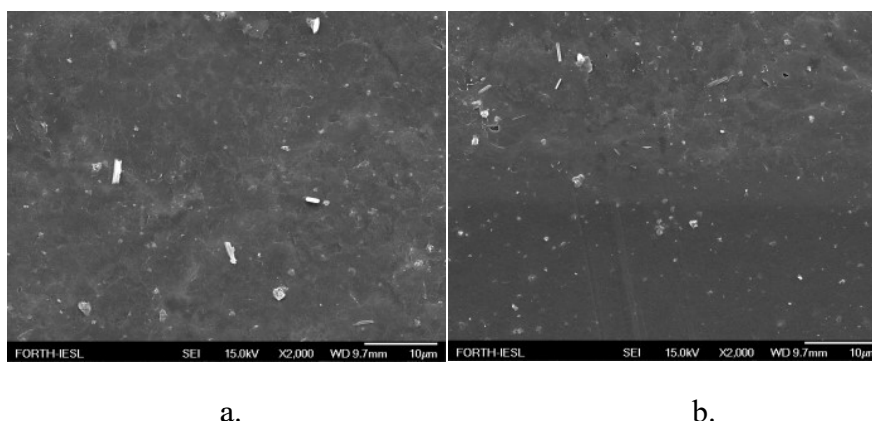


*Figure 5.53. a) A more continuous and less rough rGO surface without flakes and a lot of holes, possibly due to the irradiation with higher laser fluence and b) Interface between the rGO (top) and GO (bottom) film.*

The EDS spectrum for this reduced area displayed peaks that correspond to the elements of C, O, Cl, Si, Ca, Na, Mg and Au, exactly as the irradiated area with 26 mJ\*cm<sup>-2</sup>. It is also worth mentioning the fact that the intensity of the oxygen peak is a bit lower than that of the irradiated area with 26 mJ\*cm<sup>-2</sup>, which is an indicator of a higher efficiency of the reduction using the fluence of 39 mJ\*cm<sup>-2</sup>.

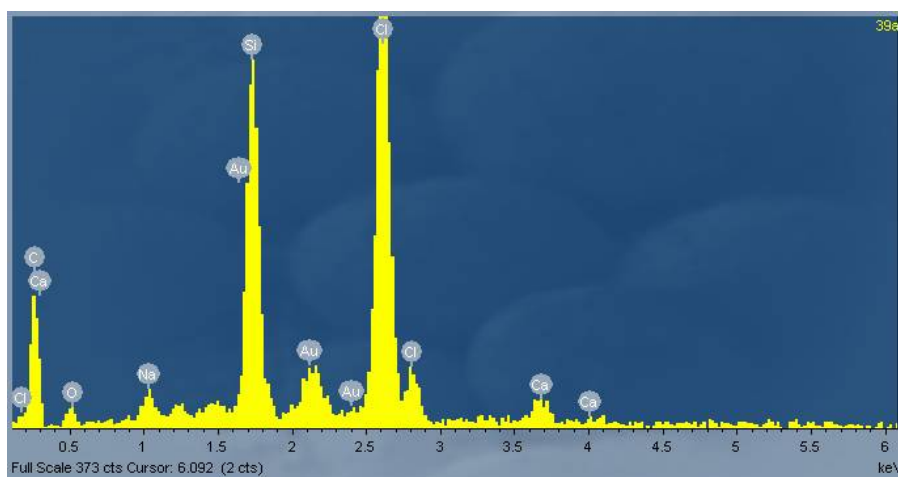


*Figure 5.54. EDS analysis for irradiated GO film with  $39 \text{ mJ} \cdot \text{cm}^{-2}$ .*

### 5.5 Fabrication of the electrodes-Laser reduction of GO (LrGO)

After optimizing the deposition and the reduction conditions the fabrication of the electrodes took place. Four samples were used, with LiU and commercial glass substrates and GO on top, as well as glass substrate with parylene on top or glass treated at first with silane and then coated with parylene. The spot size used was  $30 \pm 0.8 \mu\text{m}$  and the irradiation took place by using the optimum fluence of  $39 \pm 0.4 \text{ mJ} \cdot \text{cm}^{-2}$  (corresponding power  $17 \pm 0.1 \text{ mW}$ ).

**Table 5.18.** Irradiation Conditions

Code	Description	Fluence ( $\text{mJ} \cdot \text{cm}^{-2}$ ) $\pm 0.4$	Power (mW) $\pm 0.1$	Spot size ( $\mu\text{m}$ ) $\pm 0.8$	Outcome
EPI.SG.014	LG/GO 18 ml/336 cycles	39	17	30	Dark under microscope
EPI.SG.016	LG/paryl/silane/GO 18 ml /336 cycles	39	17	30	Bright under microscope
EPI.SG.021	LG/parylene/GO 18 ml/540 cycles	39	17	30	Dark under microscope
EPI.SG.022	LG/paryl/silane/GO 18 ml/540 cycles	39	17	30	Bright under microscope

For **LG/GO 18 ml/336 cycles** the obtained results are shown in the following Figures.

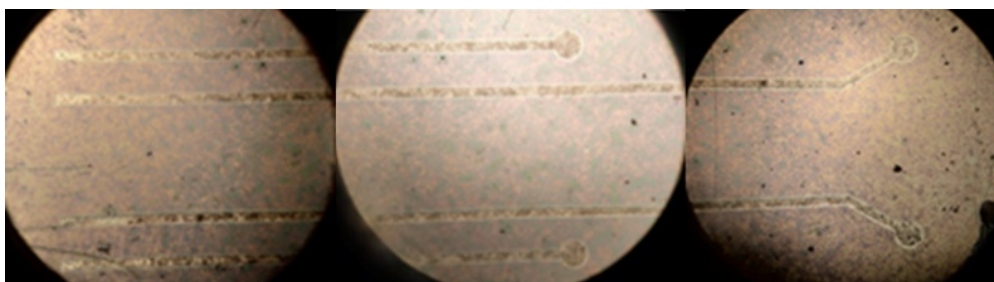
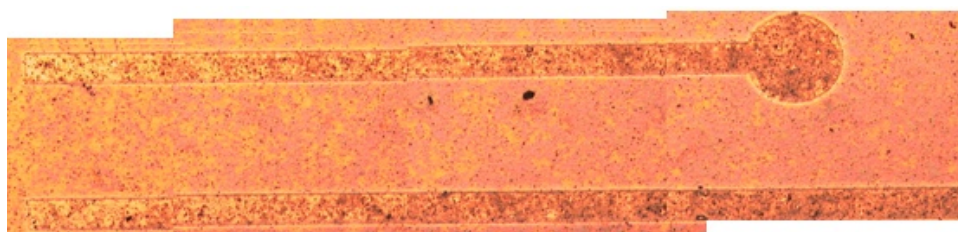
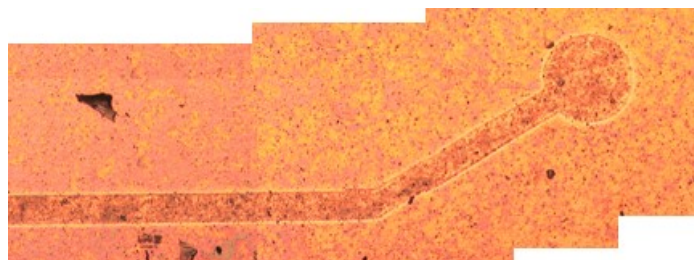


*Figure 5.55. Optical microscope image of the electrodes on top of LG/GO 18ml/336 cycles sample, created with a fluence of  $39 \pm 0.4 \text{ mJ} \cdot \text{cm}^{-2}$ .*

The electrodes seemed reduced in the eye (dark colour), thus under microscope should be bright in order to show that the material is reduced. However, under microscope were dark too, that's why Raman and I-V characteristics are needed to confirm or not the reduction.



a.



b.

*Figure 5.56. Electrodes on top of LG/GO 18ml/336 cycles sample, created with a fluence of  $39 \pm 0.4 \text{ mJ} \cdot \text{cm}^{-2}$  and seen under the optical microscope. a. Short electrode and b. Long electrode.*

For **LG/parylene/silane/GO 18 ml/336 cycles** the obtained results are shown in the following Figures.

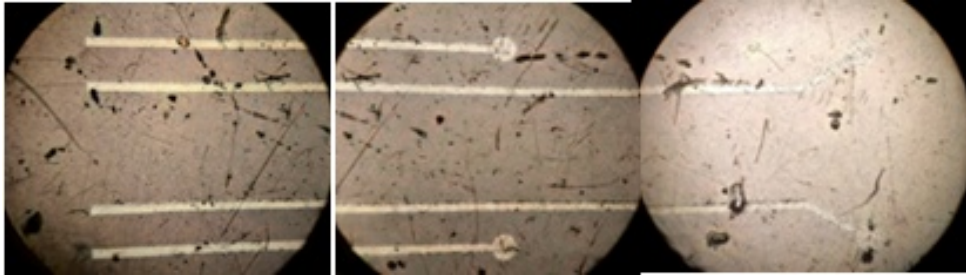


*Figure 5.57. Optical microscope image of the electrodes on top of LG/parylene/silane/GO 18ml/336 cycles sample, created with a fluence of  $39 \pm 0.4 \text{ mJ} \cdot \text{cm}^{-2}$ .*

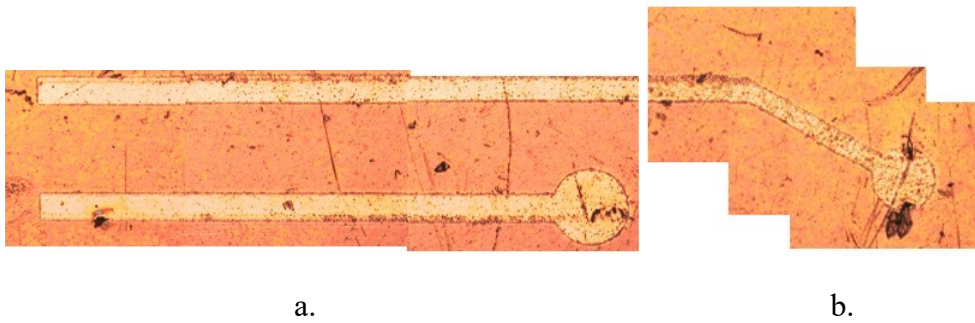
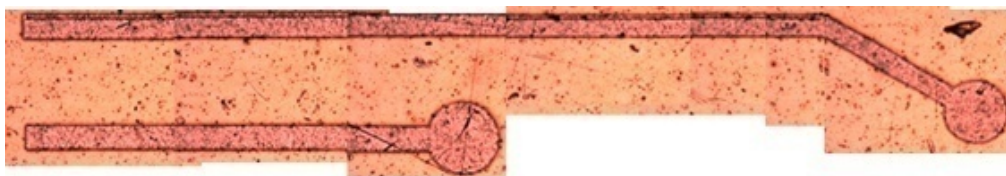


*Figure 5.58. Electrodes on top of LG/parylene/silane/GO 18ml/336 cycles sample, created with a fluence of  $39 \pm 0.4 \text{ mJ} \cdot \text{cm}^{-2}$  and seen under the optical microscope. a. Short electrode and b. Long electrode.*

For **LG/parylene/GO 18 ml/540 cycles** the obtained results are shown in the following Figures.

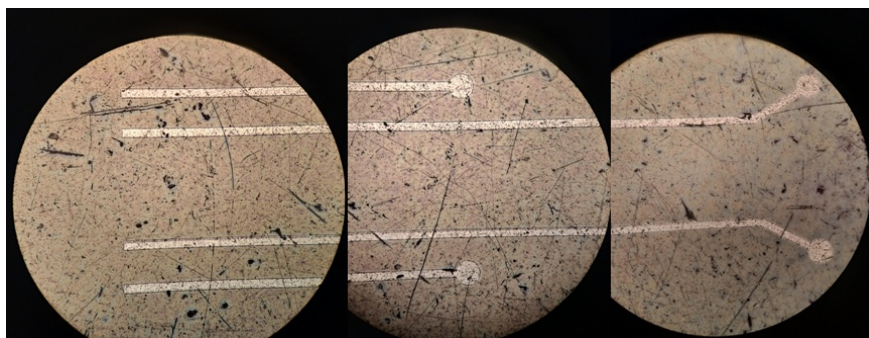


*Figure 5.59. Optical microscope image of the electrodes on top of LG/parylene/GO 18ml/540 cycles sample, created with a fluence of  $39 \pm 0.4 \text{ mJ} \cdot \text{cm}^{-2}$ .*



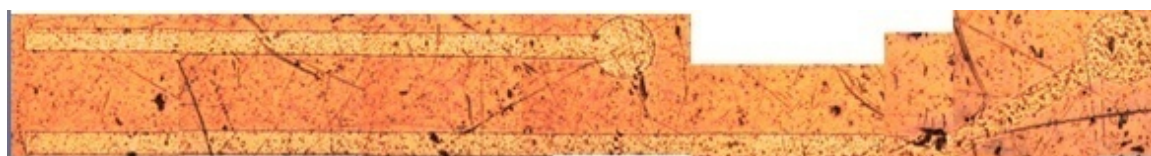
*Figure 5.60. Electrodes on top of LG/parylene/GO 18ml/540 cycles sample, created with a fluence of  $39 \pm 0.4 \text{ mJ} \cdot \text{cm}^{-2}$  and seen under the optical microscope. Short electrode and long electrode.*

For **LG/parylene/silane/GO 18 ml/540 cycles** the obtained results are shown in the following figures.



*Figure 5.61. Optical microscope image of the electrodes on top of LG/parylene/silane/GO 18ml/540 cycles sample, created with a fluence of  $39 \pm 0.4 \text{ mJ} \cdot \text{cm}^{-2}$ .*

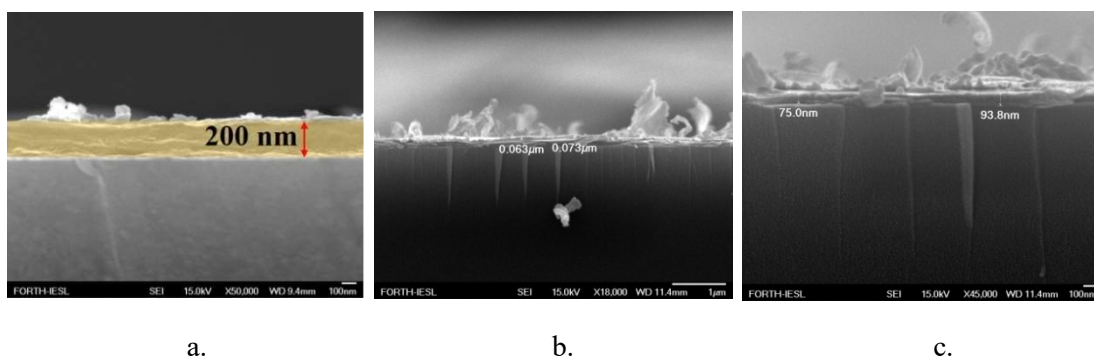
The electrodes seemed reduced in the eye (dark colour) and under microscope were bright. This is a first indication of reduction as the material is not destroyed or burnt but reduced. However, more characterizations are needed for the confirmation of the reduction.



*Figure 5.62. Electrodes on top of LG/parylene/silane/GO 18ml/540 cycles sample, created with a fluence of  $39 \pm 0.4 \text{ mJ} \cdot \text{cm}^{-2}$  and seen under the optical microscope. Short electrode and long electrode.*

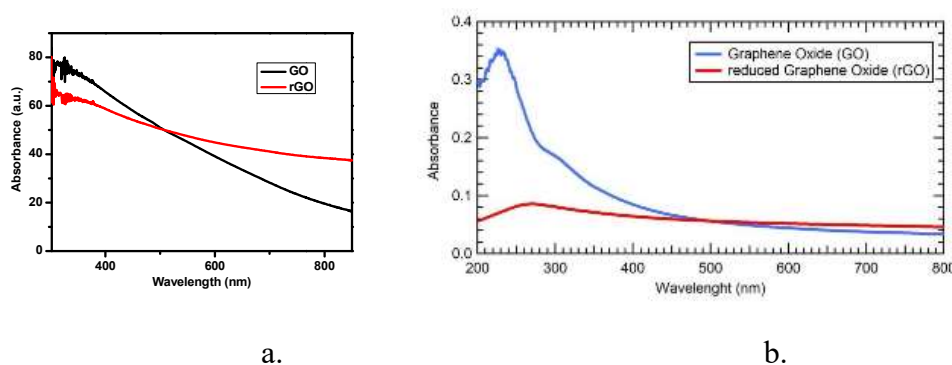
## **5.6 Characterization of both GO and the produced Laser reduced GO electrodes**

The field emission scanning electron microscope (FE-SEM) was used to acquire the cross-sectional view of spray gun coated GO and LrGO film. Figure 5.63a represents the cross-sectional view of a GO film on glass substrate. The average thickness of the GO film is  $200 \pm 45 \text{ nm}$  (average value calculated using the thickness values from 12 different locations along the length of the film). Figure 5.63b,c show the cross-sectional view of a LrGO film on glass substrate. The average thickness of the LrGO film is  $76 \pm 20 \text{ nm}$  (average value calculated using the thickness values from 11 different locations along the length of the reduced area). The thickness of both GO and LrGO films was determined accurately on glass substrate since the ‘rubbery’ nature of the parylene does not allow a clear cross sectional cut.



*Figure 5.63.* Cross-sectional view of a) GO film on glass substrate and b, c) LrGO film on glass substrate made utilizing  $39 \text{ mJ} \cdot \text{cm}^{-2}$  and used for thickness measurements at two different locations.

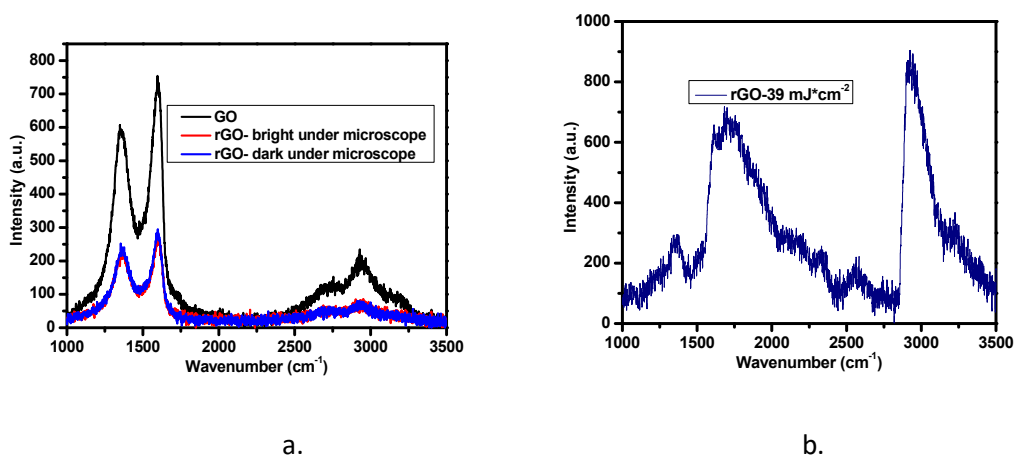
GO and LrGO were then characterized by UV-Vis absorption spectroscopy. A special sample was created for this characterization with dimensions  $4 \times 6 \text{ mm}^2$ . Absorbance spectra of GO and rGO are shown in Figure 5.64a. A characteristic peak of GO, shown at around 310 nm, was observed in the pristine GO spectrum. This peak can be correlated to the electronic transition from  $n-\pi^*$  orbital, while in lower wavelength there was a lot of noise, making impossible the detection of the peak corresponding to the transition from  $\pi-\pi^*$ . Figure 5.64a also shows the absorbance spectrum of rGO, which, according to literature [171], has a peak at a wavelength around 268 nm, which corresponds to the change from the  $sp^3$  to  $sp^2$  hybridization. However, due to the limitation of the instrument used, the detection of peaks below 300 nm was not possible. Nonetheless, it is observed that in longer wavelengths than 600 nm the rGO spectrum tends to become constant, as in the case of the absorbance spectrum of pristine graphene [172]. The last outcome is the first indication of an effective laser reduction of GO. Furthermore, the GO absorbance spectrum from the experiments of Rokmana *et al.* [171] is very similar to the GO absorbance spectrum found in this study.

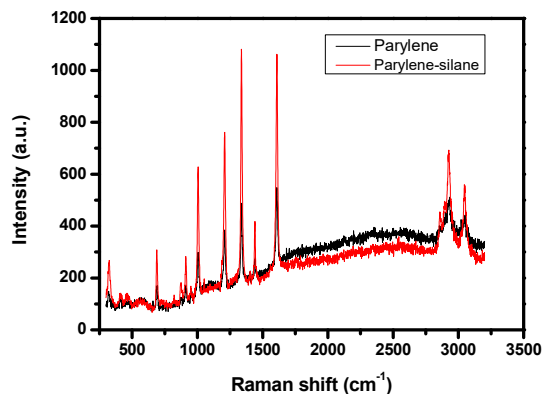


*Figure 5.64.* a) Absorbance spectra of GO and rGO on commercial glass substrate and b) Comparison with the reference [171].

As rGO is darker than GO after the laser reduction, it would be expected to have a higher absorbance than the GO film. However, after the reduction, GO layers have been removed and the rGO film is thinner than the initial pristine GO (see Figure 5.63). Thus, a thinner film, especially as it is also non uniform, with structure more similar to graphene will be more transparent than a thicker film of GO and therefore less absorbent.

Afterwards, the Raman spectra of pristine and irradiated GO films were recorded. In Figure 5.65a the Raman spectra obtained from pristine (GO) and LrGO samples are shown. The spectra of GO featured the characteristic peaks at  $\sim 1361\text{ cm}^{-1}$ ,  $\sim 1591\text{ cm}^{-1}$ ,  $\sim 2701\text{ cm}^{-1}$ ,  $\sim 2926\text{ cm}^{-1}$  and  $\sim 3189\text{ cm}^{-1}$ , which correspond to the D, G, 2D, D+G and 2D' bands of the GO lattice, respectively. All the Raman band peak positions were determined after Lorentzian function fitting. Note that the Raman spectra obtained from irradiated areas (LrGO) with different brightness under the optical microscope (measurements are differentiated between bright and dark LrGO areas) are shown in Figure 5.66. The Raman spectra of LrGO displayed characteristic peaks at  $\sim 1364$ ,  $\sim 1595$ ,  $\sim 2722$  and  $\sim 2930\text{ cm}^{-1}$ , corresponding to D, G, 2D and D+G bands, respectively. In which, the intensity of all Raman modes (in LrGO bright and dark areas) remain the same. However, compared to pristine GO the intensity of LrGO Raman modes is significantly reduced. The peak intensities reduction can occur due to the oxidative burning and/or due to the reduction of functional groups at basal plane, as the D band is associated with the structural defects [149], while the G band indicates the  $E_{2g}$  vibration mode of  $sp^2$  carbon domains [44]. Table 5.19 represents the values obtained from the Raman spectra of pristine and irradiated GO. In Figure 5.65b the Raman spectrum of LrGO areas containing parylene on the top of the glass substrate is shown. Parylene bands underneath LrGO can be identified via Raman characterization (Figure 5.65b), as it is confirmed by the parylene bands observed after Raman characterization on naked parylene substrate seen in Figure 5.65c.





c.

*Figure 5.65. a) Raman spectra of GO and LrGO on glass substrates (EPI.SG.014), b) Raman spectrum of LrGO on glass-parylene substrates (samples EPI.SG.016, EPI.SG.021, EPI.SG.022 in table 5.18) and c) Raman spectra of parylene and parylene-silane on glass substrate.*

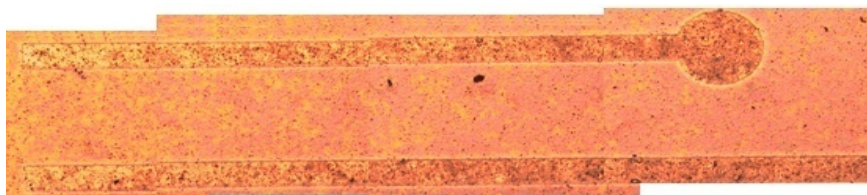
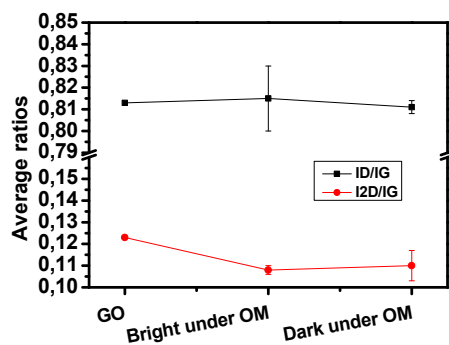


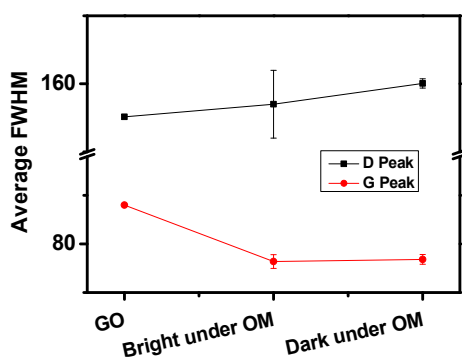
*Figure 5.66. Image of the LrGO electrodes. The irradiated area looked brighter in some regions and darker in others.*

**Table 5.19.** Average ratios and FWHM of Lorentzian fitted results for D,G and 2D bands.

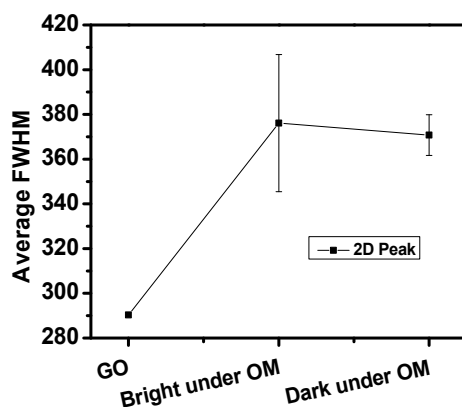
	$(I_D/I_G)$ Average	$(I_{2D}/I_G)$ Average	(D FWHM) Average	(G FWHM) Average	(2D FWHM) Average
<b>Pristine GO</b>	0.813	0.123	155	88	290
<b>rGO- bright under OM</b>	$0.815 \pm 0.015$	$0.108 \pm 0.002$	$157 \pm 5$	$76 \pm 1$	$376 \pm 31$
<b>rGO- dark under OM</b>	$0.811 \pm 0.003$	$0.110 \pm 0.007$	$160 \pm 1$	$77 \pm 1$	$371 \pm 9$



a.



b.



c.

*Figure 5.67. a) Average  $I_D/I_G$  and  $I_{2D}/I_G$  ratios, b) Average FWHM for D and G bands and c) Average FWHM for 2D band, for GO and LrGO irradiated areas, both bright and dark under OM.*

After reduction, the  $I_D/I_G$  ratio remains almost at the same levels with a slight increase in the brighter areas and a slight decrease in the darker irradiated areas under the optical microscope. This indicates that despite the removal of oxygen functional groups it is not possible to totally rearrange the carbon lattice and that some defects have been preserved. Furthermore, the absence of an intense and strong 2D band after

the reduction shows a lower degree of graphitization [44], without excluding the possibility of sufficient laser reduction and consequently the increase of conductivity. UV-Vis spectroscopy and color changes observed via optical microscopy, from light brown (GO) to dark brown-black (LrGO) confirm the reduction of GO and the production of electrodes.

In the end, electrical characterization of the laser reduced area and the recording of the I-V measurements were performed, in order to investigate the effectiveness of laser reduction on GO film. Figure 5.68a shows the current-voltage (I-V) characteristics of LrGO areas and Figure 5.68b displays the sheet resistance calculated by the I-V curves.

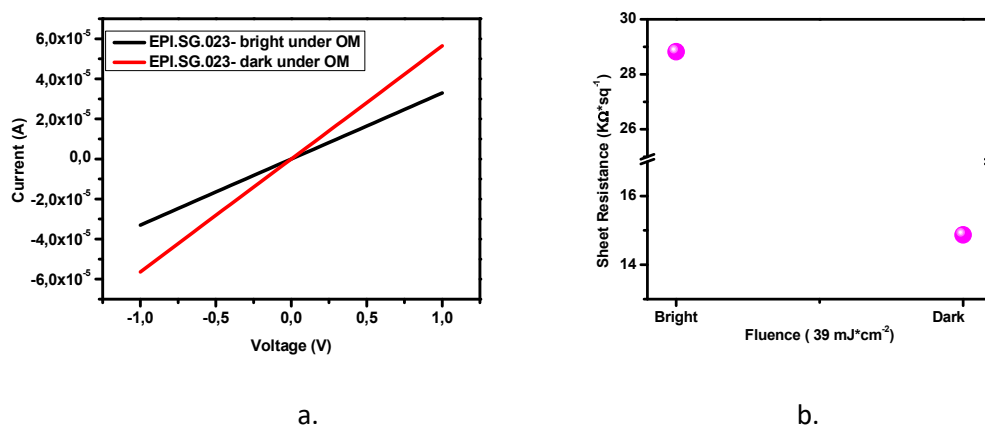


*Figure 5.68. a) Current-voltage characteristics of laser irradiated GO films on top of commercial glass (EPI.SG.023) with  $39 \pm 0.4 \text{ mJ} \cdot \text{cm}^{-2}$  laser fluence for brighter and darker areas under the optical microscope and b) Sheet resistance calculated for darker and brighter areas.*

**Table 5.20.** Resistance and Sheet Resistance values for LrGO micro-electrodes.

Fluence ( $\text{mJ} \cdot \text{cm}^{-2}$ )	Resistance ( $\text{K}\Omega$ )	Length (mm) $\pm 0.001$	Width (mm) $\pm 0.001$	Sheet Resistance ( $\text{K}\Omega/\text{sq}$ )
39- bright under OM	30	0.75	0.7	$29 \pm 0.05$
39 - dark under OM	18	0.85	0.7	$15 \pm 0.03$

The sheet resistance obtained by laser fluence of  $39 \pm 0.4 \text{ mJ} \cdot \text{cm}^{-2}$ , varies between 15  $\text{K}\Omega/\text{sq}$  for darker areas and 29  $\text{K}\Omega/\text{sq}$  for brighter areas under optical microscope. The deviation between the two values of the sheet resistance, bright and dark areas could be attributed to the thickness variation of the GO film. These values are very close to the sheet resistance reported by Kymakis *et al.* [49, 45] for a 4.5-nm thick laser rGO (LrGO) film, which was 18  $\text{K}\Omega/\text{sq}$ . Furthermore, the comparison between the resistivity value for pristine GO [173] and the resistivity values for LrGO (bright and dark areas under microscope) show a significant decrease for the laser irradiated areas

(Table 5.21 and Figure 5.69). Therefore, the I-V characteristics prove the successful laser reduction and conductivity of the electrodes.

**Table 5.21.** Comparison of resistivity values for pristine GO and laser reduced GO (LrGO)

	Resistivity ( $\Omega \cdot \text{mm}$ )
<b>Pristine GO</b>	$\sim 10^4$ [173]
<b>rGO - bright under OM</b>	$2 \pm 0.6$
<b>rGO - dark under OM</b>	$1 \pm 0.3$

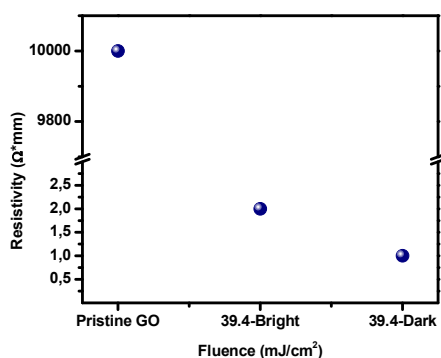


*Figure 5.69. Comparison of resistivity values between pristine GO and LrGO sample (EPI.SG.023) irradiated with  $39 \pm 0.4 \text{ mJ} \cdot \text{cm}^{-2}$  laser fluence, both for brighter and darker areas under the optical microscope.*

## CHAPTER 6

### CONCLUSIONS AND FUTURE WORK

Bioelectronics and biosensors are two topics of great scientific interest. These domains advance knowledge to higher levels, as they require the understanding of a variety of fields. Innovation in preventing, diagnosing and treating diseases can be achieved with the creation of new bioelectronic devices. The treatment of illnesses poses an enormous challenge, particularly when they involve the implantation of electronic devices in the human body, as the materials utilized play a key role in the interface between the microelectronics and the biological tissue. Thus, materials that exhibit characteristics suitable for both the body (such as biocompatibility) and the electrical components (such as conductivity) are crucial.

In this thesis, graphene oxide has been used for the fabrication of graphene-based electrodes for bioelectronic devices. More precisely, these electrodes will be incorporated into a single device with an inorganic ion pump and an electrophysiological sensor. The aim of such a device is to be implanted on the brain of patients suffering from Epilepsy, in order to prevent and control epileptic seizures. One of the biggest challenges of this project, besides the creation of the electrodes themselves, is to expand the use of such a device for other neurological disorders as well.

The methods used in this work for the fabrication of GO thin films were vacuum filtration and spray gun. After scientific evidence, spray gun was selected as the fabrication technique, given that films made by vacuum filtration detached from the substrate after a small period of time. Thus, they didn't fulfil the minimum requirement for implantation. Afterwards, characterizations of the films were performed in order to identify the molecular structure, the electronic transitions and the film topography and thickness. Laser treatment was followed by a parametric study with different fluences and scanning speeds to better understand the conductivity properties and find the optimum conditions.

GO was coated on top of three different substrates. The first substrate was glass; the second consisted on parylene on top of glass, and the third one on parylene on top of silane-treated glass. Parylene is a soft and flexible material, which makes it convenient for implantation on brain tissues. Glass is biocompatible; however it is hard and not flexible. Therefore, experiments with all these composites had a main purpose; to find out which of the different composite combinations is the most suitable for being implanted. The parylene on top of silane-treated glass has a stronger bonding; hence the parylene cannot be detached from it and the whole composite of glass/parylene/GO is going to be tested. The glass that is not treated with silane has not such strong bonding with parylene, thus parylene can be peeled off and, with the GO on top of it, to be used as a free-standing device. Thus, GO on top of glass substrates are more suitable for the in vitro experiments with cells and the in vitro

device development, while the GO on top of parylene substrate as a free-standing device is better suited for being used for the ex vivo experiments on top of mice brain slices.

A parametric study for fluences and scanning speeds was performed in order to find out the optimum conditions of reduction. After the laser reduction of GO films with different scanning speeds and fluences on top of glass substrate, Raman mapping and I-V characteristics took place among other characterization techniques. The results displayed that the lowest scanning speed ( $250 \mu\text{m}\cdot\text{s}^{-1}$ ) and the highest fluence ( $157 \text{mJ}\cdot\text{cm}^{-2}$ ) resulted in the lowest sheet resistance and therefore, they could be considered as the optimum conditions. However, even if  $250 \mu\text{m}\cdot\text{s}^{-1}$  was indeed the best speed for the reduction, such a high fluence ( $157 \text{mJ}\cdot\text{cm}^{-2}$ ) ablates the GO film at a high level and can burn both glass and parylene substrates.

Due to the parylene substrate which is a very sensitive material, the fluences used needed to be very low, sacrificing some conductivity, but obtaining reduced electrodes without burnt parylene and complete ablation of the GO film. That is why only the lowest fluences were tested ( $26, 52$  and  $79 \text{mJ}\cdot\text{cm}^{-2}$ ) including also one more intermediate fluence of  $39 \text{mJ}\cdot\text{cm}^{-2}$  as it was observed that, especially on top of parylene, even irradiating with just  $52 \text{mJ}\cdot\text{cm}^{-2}$  the GO film was partially reduced and partially ablated. After the Raman results and the I-V characteristics, the fluence of  $39 \text{mJ}\cdot\text{cm}^{-2}$  was the optimum fluence to create the electrodes as it was the one resulting the highest conductivity (lowest sheet resistance) both on glass and parylene substrates.

The final LrGO electrodes were created using the  $(39 \pm 0.4) \text{mJ}\cdot\text{cm}^{-2}$  fluence on top of glass substrate, of glass substrate treated with silane with a parylene coating on top and of untreated glass with parylene on top. A full characterization study followed, confirming the low sheet resistance and the high conductivity of the electrodes. Finally, these electrodes were sent to our partners at LiU in order to be incorporated in an all-in-one device with the rest of the components (organic electronic ion pump, electrophysiological sensor) and then to be tested in vitro and ex vivo by our partners at Aix-Marseille University.

Despite the fact that in the end, the development of the graphene-based electrodes was successful for both attached and free-standing devices, there were hurdles in some of the techniques and parameters used. This section, besides stating the conclusions, also aims to address how to overcome some of those obstacles and to discuss our future plans.

A major issue encountered in this work was that the utilization of a homemade spray gun tool led to the creation of GO films with non-uniform thickness and non repeatable amount of cycles. This non-uniformity of the thickness caused that, during the reduction process, some areas of the films were properly reduced, while others were ablated or burnt. An alternative to this approach would consist on increasing the

volume of GO solution used, which would create thicker films. While this could address the issue of some areas being ablated or burnt, it would still not solve the problem of the non uniform thickness of the films. Therefore, the optimum solution is the use of a professional commercial tool, which would diminish the non-uniform effect, due to its controlled spray nozzle parameters and droplet size, providing repeatable and uniform results.

As for our future plans, the next step is the functionalization of the rGO area with suitable biomolecules. Typically, biomolecules are attached on top of a substrate, such as a conjugative polymer, that can be both deposited on the electrodes and also be functionalized with the biomolecules. The conductivity of the conjugative polymer facilitates the transfer of signals (electrons) created by the redox reactions, so that the electrons travel through the polymer to the electrodes, where the sensing takes place. One of the many advantages of utilizing rGO electrodes is that as some oxygen containing groups have been removed by reduction, the biomolecules can be attached directly on top of rGO electrodes. This direct contact between the electrodes and the biomolecules allows to electrons to travel shorter distances, paving the way for sensors with faster response times.

The biomolecule that will be functionalized on the rGO for the biosensing is Glucose Oxidase (GOx). GOx will interact with the glucose and will produce  $H_2O_2$ . Through redox reactions,  $H_2O_2$  will lead to changes in the current flow, resulting in their detection by the sensor. In such a case the sensing of the variation of glucose levels will be performed, displaying whether this variation can be a predictive biomarker for the epileptic seizures. Besides GOx, other enzymes will also be tested, such as lactate oxidase, for the detection of lactate, as it can also be a predictive biomarker for this kind of seizures. The reaction between lactate and lactate oxidase will convert lactate to an electroactive product, which will be detected by the biomolecular sensor.

Moreover, another future plan is the examination of many immobilization strategies for the enzymes on top of the LrGO electrodes, as well as the examination of different patterns of electrodes for facilitating the integration with the rest of the components. As these electrodes will be integrated with the sensor and the OEIP made by LiU, the prediction of seizures will be followed by drug delivery (release of GABA) from the capillary OEIP.

Finally, this device is expected to have a significant impact in the fields of graphene-related materials, biosensors-bioelectronics and medicine. The prediction of seizures and the local targeted delivery will improve the quality of life of patients suffering from epileptic seizures, without affecting the nearby healthy brain regions. This device could be a breakthrough in the field, as it has the potential to be used for all neurological disorders.

## REFERENCES

1. Lala, S., Kumar, A., & Prasad, R. (2019). *Active Transformation of Mind and Body Through Abundant Natural Methods (ATMAN)*. Wireless Personal Communications. doi:10.1007/s11277-019-06333-x
2. Laughlin, S. B. (2003). *Communication in Neuronal Networks*. Science, 301(5641), 1870–1874. doi:10.1126/science.1089662
3. Majhi, S., K.Bera, B., Ghosh, D., & Perc, M. (2018). *Chimera states in neuronal networks: A review*. Physics of Life Reviews. doi:10.1016/j.plrev.2018.09.003
4. World Health Organization (WHO). (2005). Atlas: Epilepsy Care in the World. Who Library Cataloguing-in Public Data, p. 24-27. ISBN: 92 4 156303
5. Nir, Y., Andriillon, T., Marmelshtein, A., Suthana, N., Cirelli, C., Tononi, G., & Fried, I. (2017). *Selective neuronal lapses precede human cognitive lapses following sleep deprivation*. Nature Medicine, 23(12), 1474–1480. doi:10.1038/nm.4433
6. <https://indiabioscience.org/news/2012/sree-chitra-tirunal-institute-epilepsy-management> (Accessed on 17<sup>th</sup> November 2019)
7. Younus, I., & Reddy, D. S. (2018). *A resurging boom in new drugs for epilepsy and brain disorders*. Expert Review of Clinical Pharmacology, 11(1), 27–45. doi:10.1080/17512433.2018.1386553
8. Lasefr, Z., Ayyalasomayajula, S. S. V. N. R., & Elleithy, K. (2017). *Epilepsy seizure detection using EEG signals*. IEEE 8th Annual Ubiquitous Computing, Electronics and Mobile Communication Conference (UEMCON). doi:10.1109/uemcon.2017.8249018
9. Pato-Pato, A. *Evaluation of the direct costs of epilepsy*, Available from Journal of Neurology and Neuroscience online, <http://www.jneuro.com/neurology-neuroscience/evaluation-of-the-direct-costs-of-epilepsy.php?aid=6463> , (Accessed 1<sup>0th</sup> December 2019)
10. McLin, W. M., & Boer, H. M. (1995). *Public Perceptions About Epilepsy*. Epilepsia, 36(10), 957–959. doi:10.1111/j.1528-1157.1995.tb00952.x
11. Harvard Health topics (<https://www.drugs.com/health-guide/epilepsy.html>) (Accessed on 10<sup>th</sup> December 2019)
12. Baillet, S. (2017). *Magnetoencephalography for brain electrophysiology and imaging*. Nature Neuroscience, 20(3), 327–339. doi:10.1038/nn.4504
13. Waser, M., Benke, T., Dal-Bianco, P., Garn, H., Mosbacher, J. A., Ransmayr, G., ...Jennum, P. J. (2018). *Neuroimaging markers of global cognition in early Alzheimer's disease: A magnetic resonance imaging-electroencephalography study*. Brain and Behavior, e01197. doi:10.1002/brb3.1197
14. Georgiadis, I., Kapsalaki, E. Z., & Fountas, K. N. (2013). *Temporal Lobe Resective Surgery for Medically Intractable Epilepsy: A Review of*

- Complications and Side Effects*. *Epilepsy Research and Treatment*, 2013, 1–12. doi:10.1155/2013/752195
15. Verrotti, A., Lattanzi, S., Brigo, F., & Zaccara, G. (2020). *Pharmacodynamic interactions of antiepileptic drugs: From bench to clinical practice*. *Epilepsy & Behavior*, 104, 106939. doi:10.1016/j.yebeh.2020.106939
  16. Ortinski, P., & Meador, K. J. (2004). *Cognitive side effects of antiepileptic drugs*. *Epilepsy & Behavior*, 5, 60–65. doi:10.1016/j.yebeh.2003.11.008
  17. Kwan, P., & Brodie, M. J. (2001). *Neuropsychological effects of epilepsy and antiepileptic drugs*. *The Lancet*, 357(9251), 216–222. doi:10.1016/s0140-6736(00)03600-x
  18. Perucca, P., & Gilliam, F. G. (2012). *Adverse effects of antiepileptic drugs*. *The Lancet Neurology*, 11(9), 792–802. doi:10.1016/s1474-4422(12)70153-9
  19. Rivnay, J., Owens, R. M., & Malliaras, G. G. (2014). *The Rise of Organic Bioelectronics*. *Chemistry of Materials*, 26(1), 679–685. doi:10.1021/cm4022003
  20. Valentinuzzi, M. E. (2017). *Cardiac Pacemakers: A Multiauthored Breakthrough Technology [Retrospectroscope]*. *IEEE Pulse*, 8(4), 74–78. doi:10.1109/mpul.2017.2700427
  21. Khodagholy, D., Gelinias, J. N., Thesen, T., Doyle, W., Devinsky, O., Malliaras, G. G., & Buzsáki, G. (2015). *NeuroGrid: recording action potentials from the surface of the brain*. *Nature Neuroscience*, 18(2), 310–315. doi:10.1038/nn.3905
  22. Denison, T. (2019). *Bioelectronic devices*. *Ingenia magazine - Royal Academy of Engineering*. Issue 80. 25-28.
  23. Asada, H. H., Shaltis, P., Reisner, A., Sokwoo Rhee, & Hutchinson, R. C. (2003). *Mobile monitoring with wearable photoplethysmographic biosensors*. *IEEE Engineering in Medicine and Biology Magazine*, 22(3), 28–40. doi:10.1109/memb.2003.1213624
  24. Rosset, S., Niklaus, M., Dubois, P., & Shea, H. R. (2009). *Metal Ion Implantation for the Fabrication of Stretchable Electrodes on Elastomers*. *Advanced Functional Materials*, 19(3), 470–478. doi:10.1002/adfm.200801218
  25. Kermanizadeh, A., Jantzen, K., Ward, M. B., Durhuus, J. A., Juel Rasmussen, L., Loft, S., & Møller, P. (2017). *Nanomaterial-induced cell death in pulmonary and hepatic cells following exposure to three different metallic materials: The role of autophagy and apoptosis*. *Nanotoxicology*, 11(2), 184–200. doi:10.1080/17435390.2017.1279359
  26. Liao, C., Zhang, M., Yao, M. Y., Hua, T., Li, L., & Yan, F. (2014). *Flexible Organic Electronics in Biology: Materials and Devices*. *Advanced Materials*, 27(46), 7493–7527. doi:10.1002/adma.201402625

27. Rodrigo, D., Limaj, O., Janner, D., Etezadi, D., Garcia de Abajo, F. J., Pruneri, V., & Altug, H. (2015). *Mid-infrared plasmonic biosensing with graphene*. *Science*, 349(6244), 165–168. doi:10.1126/science.aab2051
28. FLAG-ERA JTC 2017 Full Proposal, Project EPIGRAPH. European Reference Code: 26632
29. Taylor, N. (2000). *Laser: The Inventor, The Nobel Laureate, and The Thirty-Year Patent War*. Simon & Schuster. ISBN 978-0684835150.
30. Siegman, Anthony E. (1986). *Lasers*. University Science Books. p. 2. ISBN 978-0-935702-11-8.
31. <https://en.wikipedia.org/wiki/Laser> (Accessed on 28<sup>th</sup> December 2019)
32. Svelto, O. (2009). *Introductory Concepts*. Principles of Lasers, 1–15. doi:10.1007/978-1-4419-1302-9\_1
33. Kannatey-Asibu Jr, E. (2009). *Principles of laser materials processing* (Vol. 4). John Wiley & Sons. ISBN 978-0-470-17798-3.
34. Haken, H. (1970). *Laser Theory*. Light and Matter Ic / Licht Und Materie Ic, 1–304. doi:10.1007/978-3-662-22091-7\_1
35. <https://www.daenotes.com/electronics/microwave-radar/laser-light-properties> (Accessed on 28<sup>th</sup> December 2019)
36. Loryuenyong, V., Totepvimarn, K., Eimburanaprat, P., Boonchompoo, W., & Buasri, A. (2013), *Preparation and Characterization of Reduced Graphene Oxide Sheets via Water-Based Exfoliation and Reduction Methods*. *Advances in Materials Science and Engineering*. 1–5. doi:10.1155/2013/923403
37. Zhou, Y., Bao, Q., Tang, L. A. L., Zhong, Y., & Loh, K. P. (2009). *Hydrothermal Dehydration for the “Green” Reduction of Exfoliated Graphene Oxide to Graphene and Demonstration of Tunable Optical Limiting Properties*. *Chemistry of Materials*, 21(13), 2950–2956. doi:10.1021/cm9006603
38. Tung, V. C., Allen, M. J., Yang, Y., & Kaner, R. B. (2008). *High-throughput solution processing of large-scale graphene*. *Nature Nanotechnology*, 4(1), 25–29. doi:10.1038/nnano.2008.329
39. Ma, B., Rodriguez, R. D., Ruban, A., Pavlov, S., Sheremet, E. (2019). *The Correlation Between Electrical Conductivity and Second-Order Raman Modes of Laser-Reduced Graphene Oxide*. *Physical Chemistry Chemical Physics*. 21(19):10125-10134. doi: 10.1039/c9cp00093c
40. Pei, S., & Cheng, H.-M. (2012). *The reduction of graphene oxide*. *Carbon*, 50(9), 3210–3228. doi:10.1016/j.carbon.2011.11.010
41. Cote, L. J., Cruz-Silva, R., & Huang, J. (2009). *Flash Reduction and Patterning of Graphite Oxide and Its Polymer Composite*. *Journal of the American Chemical Society*, 131(31), 11027–11032. doi:10.1021/ja902348k
42. Gao, X., Jang, J., & Nagase, S. (2009). *Hydrazine and Thermal Reduction of Graphene Oxide: Reaction Mechanisms, Product Structures, and Reaction*

- Design*. The Journal of Physical Chemistry C, 114(2), 832–842. doi:10.1021/jp909284g
43. Shang, Y., Zhang, D., Liu, Y., & GUO, C. (2015). *Preliminary comparison of different reduction methods of graphene oxide*. Bulletin of Materials Science, 38(1), 7–12. doi:10.1007/s12034-014-0794-7
  44. Alazmi, A., Rasul, S., Patole, S. P., & Costa, P. M. F. J. (2016). *Comparative study of synthesis and reduction methods for graphene oxide*. Polyhedron, 116, 153–161. doi:10.1016/j.poly.2016.04.044
  45. Kymakis, E., Savva, K., Stylianakis, M. M., Fotakis, C., & Stratakis, E. (2013). *Flexible Organic Photovoltaic Cells with In Situ Nonthermal Photoreduction of Spin-Coated Graphene Oxide Electrodes*. Advanced Functional Materials, 23(21), 2742–2749. doi:10.1002/adfm.201202713
  46. Stankovich, S., Dikin, D. A., Piner, R. D., Kohlhaas, K. A., Kleinhammes, A., Jia, Y., ... Ruoff, R. S. (2007). *Synthesis of graphene-based nanosheets via chemical reduction of exfoliated graphite oxide*. Carbon, 45(7), 1558–1565. doi:10.1016/j.carbon.2007.02.034
  47. Petridis, C., Lin, Y.-H., Savva, K., Eda, G., Kymakis, E., Anthopoulos, T. D., & Stratakis, E. (2013). *Post-fabrication, in situ laser reduction of graphene oxide devices*. Applied Physics Letters, 102(9), 093115. doi:10.1063/1.4794901
  48. Trusovas, R., Ratautas, K., Račiukaitis, G., Barkauskas, J., Stankevičienė, I., Niaura, G., & Mažeikienė, R. (2013). *Reduction of graphite oxide to graphene with laser irradiation*. Carbon, 52, 574–582. doi:10.1016/j.carbon.2012.10.017
  49. Kymakis, E., Petridis, C., Anthopoulos, T. D., & Stratakis, E. (2014). *Laser-Assisted Reduction of Graphene Oxide for Flexible, Large-Area Optoelectronics*. IEEE Journal of Selected Topics in Quantum Electronics, 20(1), 106–115. doi:10.1109/jstqe.2013.2273414
  50. Antonelou, A., Sygellou, L., Vrettos, K., Georgakilas, V., & Yannopoulos, S. N. (2018). *Efficient defect healing and ultralow sheet resistance of laser-assisted reduced graphene oxide at ambient conditions*. Carbon, 139, 492–499. doi:10.1016/j.carbon.2018.07.012
  51. Hamad, A. H. (2016). Effects of Different Laser Pulse Regimes (Nanosecond, Picosecond and Femtosecond) on the Ablation of Materials for Production of Nanoparticles in Liquid Solution. High Energy and Short Pulse Lasers. doi:10.5772/63892
  52. Perrière, J., Millon, E., Seiler, W., Boulmer-Leborgne, C., Craciun, V., Albert, O., ... Etchepare, J. (2002). Comparison between ZnO films grown by femtosecond and nanosecond laser ablation. Journal of Applied Physics, 91(2), 690–696. doi:10.1063/1.1426250
  53. Zeng, X., Mao, X. L., Greif, R., & Russo, R. E. (2005). Experimental investigation of ablation efficiency and plasma expansion during femtosecond and nanosecond laser ablation of silicon. Applied Physics A, 80(2), 237–241. doi:10.1007/s00339-004-2963-9

54. Kasaai, M. R., Kacham, V., Theberge, F., & Chin, S. L. (2003). *The interaction of femtosecond and nanosecond laser pulses with the surface of glass*. *Journal of Non-Crystalline Solids*, 319(1-2), 129–135. doi:10.1016/s0022-3093(02)01909-9
55. Zergioti, I., Mailis, S., Vainos, N. A., Ikiades, A., Grigoropoulos, C. P., & Fotakis, C. (1999). *Microprinting and microetching of diffractive structures using ultrashort laser pulses*. *Applied Surface Science*, 138-139, 82–86. doi:10.1016/s0169-4332(98)00526-1
56. <https://www.nobelprize.org/uploads/2018/10/press-fig4-fy-en-femtosecondlaser.pdf> (Accessed on 1<sup>st</sup> February 2020)
57. Zhang, Q., Liu, W., Liu, L., Xu, L., Xu, Y., & Chen, G. (2007). *Large and opposite changes of the third-order optical nonlinearities of chalcogenide glasses by femtosecond and continuous-wave laser irradiation*. *Applied Physics Letters*, 91(18), 181917. doi:10.1063/1.2805636
58. Karu, T. I., Tiphlova, O. A., Matveyets, Y. A., Yartsev, A. P., & Letokhov, V. S. (1991). *Comparison of the effects of visible femtosecond laser pulses and continuous wave laser radiation of low average intensity on the clonogenicity of Escherichia coli*. *Journal of Photochemistry and Photobiology B: Biology*, 10(4), 339–344. doi:10.1016/1011-1344(91)80019-e
59. Roy, N. K., Dibua, O. G., Jou, W., He, F., Jeong, J., Wang, Y., & Cullinan, M. A. (2017). *A Comprehensive Study of the Sintering of Copper Nanoparticles Using Femtosecond, Nanosecond, and Continuous Wave Lasers*. *Journal of Micro and Nano-Manufacturing*, 6(1), 010903. doi:10.1115/1.4038455
60. Buzea, C., Pacheco, I. I., & Robbie, K. (2007). *Nanomaterials and nanoparticles: Sources and toxicity*. *Biointerphases*, 2(4), MR17–MR71. doi:10.1116/1.2815690
61. Alwarappan, S. and Kumar, A. (2014). *Graphene-based Materials, Science and Technology*, CRC Press, Taylor and Francis Group, Chapter 1. ISBN 978-1-4398-8427
62. Novoselov, K. S. (2004). *Electric Field Effect in Atomically Thin Carbon Films*. *Science*, 306(5696), 666–669. doi:10.1126/science.1102896
63. Brumfiel, G. (2010). *Andre Geim: in praise of graphene*. *Nature*. doi:10.1038/news.2010.525
64. Han, S. A., Bhatia, R., & Kim, S.-W. (2015). *Synthesis, properties and potential applications of two-dimensional transition metal dichalcogenides*. *Nano Convergence*, 2(1). doi:10.1186/s40580-015-0048-4
65. <https://www.nobelprize.org/prizes/physics/2010/summary/> (Accessed on 27<sup>th</sup> January 2020)
66. Sheehy, D. E., & Schmalian, J. (2009). *Optical transparency of graphene as determined by the fine-structure constant*. *Physical Review B*, 80(19). doi:10.1103/physrevb.80.193411
67. <https://en.wikipedia.org/wiki/Graphene> (Accessed on 31<sup>st</sup> January 2020)

68. <http://chemistrycarbons.blogspot.com/2012/11/explanation-on-structure-of-graphite.html> (Accessed on 31<sup>st</sup> January 2020)
69. Radamson, H. H. (2017). *Graphene*. Springer Handbook of Electronic and Photonic Materials, 1–1. doi:10.1007/978-3-319-48933-9\_48
70. Zhu, Y., Murali, S., Cai, W., Li, X., Suk, J. W., Potts, J. R., & Ruoff, R. S. (2010). *Graphene and Graphene Oxide: Synthesis, Properties, and Applications*. *Advanced Materials*, 22(35), 3906–3924. doi:10.1002/adma.201001068
71. Singh, V., Joungh, D., Zhai, L., Das, S., Khondaker, S. I., & Seal, S. (2011). *Graphene based materials: Past, present and future*. *Progress in Materials Science*, 56(8), 1178–1271. doi:10.1016/j.pmatsci.2011.03.003
72. İlbay, Z., Haşimoğlu, A., Özdemir, O. K., Ateş, F., & Şahin, S. (2017). *Highly efficient recovery of biophenols onto graphene oxide nanosheets: Valorisation of a biomass*. *Journal of Molecular Liquids*, 246, 208–214. doi:10.1016/j.molliq.2017.09.046
73. Peigney, A., Laurent, C., Flahaut, E., Bacsa, R. R., & Rousset, A. (2001). *Specific surface area of carbon nanotubes and bundles of carbon nanotubes*. *Carbon*, 39(4), 507–514. doi:10.1016/s0008-6223(00)00155-x
74. Lee, C., Wei, X., Kysar, J. W., & Hone, J. (2008). *Measurement of the Elastic Properties and Intrinsic Strength of Monolayer Graphene*. *Science*, 321(5887), 385–388. doi:10.1126/science.1157996
75. Liu, N., Chortos, A., Lei, T., Jin, L., Kim, T. R., Bae, W.-G., ... Bao, Z. (2017). *Ultrasensitive and stretchable graphene electrodes*. *Science Advances*, 3(9), e1700159. doi:10.1126/sciadv.1700159
76. Allen, M. J., Tung, V. C., & Kaner, R. B. (2010). *Honeycomb Carbon: A Review of Graphene*. *Chemical Reviews*, 110(1), 132–145. doi:10.1021/cr900070d
77. Chen, J.-H., Jang, C., Xiao, S., Ishigami, M., & Fuhrer, M. S. (2008). *Intrinsic and extrinsic performance limits of graphene devices on SiO<sub>2</sub>*. *Nature Nanotechnology*, 3(4), 206–209. doi:10.1038/nnano.2008.58
78. Bolotin, K. I., Sikes, K. J., Jiang, Z., Klima, M., Fudenberg, G., Hone, J., ... Stormer, H. L. (2008). *Ultrahigh electron mobility in suspended graphene*. *Solid State Communications*, 146(9-10), 351–355. doi:10.1016/j.ssc.2008.02.024
79. Zhu, S.-E., Yuan, S., & Janssen, G. C. A. M. (2014). *Optical transmittance of multilayer graphene*. *EPL (Europhysics Letters)*, 108(1), 17007. doi:10.1209/0295-5075/108/17007
80. Nair, R. R., Blake, P., Grigorenko, A. N., Novoselov, K. S., Booth, T. J., Stauber, T., ... Geim, A. K. (2008). *Fine Structure Constant Defines Visual Transparency of Graphene*. *Science*, 320(5881), 1308–1308. doi:10.1126/science.1156965
81. Nong, J., Da, H., Fang, Q., Yu, Y., & Yan, X. (2018). *Perfect absorption in transition metal dichalcogenides-based dielectric grating*. *Journal of*

- Physics D: Applied Physics, 51(37), 375105. doi:10.1088/1361-6463/aad608
82. Yamada, Y., Yasuda, H., Murota, K., Nakamura, M., Sodesawa, T., & Sato, S. (2013). *Analysis of heat-treated graphite oxide by X-ray photoelectron spectroscopy*. *Journal of Materials Science*, 48(23), 8171–8198. doi:10.1007/s10853-013-7630-0
  83. Nanowerk, *What is graphene? Graphene properties and applications*, [https://www.nanowerk.com/what\\_is\\_graphene.php](https://www.nanowerk.com/what_is_graphene.php) (Accessed on 13<sup>th</sup> January 2020)
  84. Huang, X., Zeng, Z., Fan, Z., Liu, J., & Zhang, H. (2012). *Graphene-Based Electrodes*. *Advanced Materials*, 24(45), 5979–6004. doi:10.1002/adma.201201587
  85. Hecht, D. S., Hu, L., & Irvin, G. (2011). *Emerging Transparent Electrodes Based on Thin Films of Carbon Nanotubes, Graphene, and Metallic Nanostructures*. *Advanced Materials*, 23(13), 1482–1513. doi:10.1002/adma.201003188
  86. Chonan, T., Taguchi, O., & Omae, K. (2006). *Interstitial pulmonary disorders in indium-processing workers*. *European Respiratory Journal*, 29(2), 317–324. doi:10.1183/09031936.00020306
  87. Hosono, H., Kurita, M., & Kawazoe, H. (1998). *Excimer Laser Crystallization of Amorphous Indium-Tin-Oxide and Its Application to Fine Patterning*. *Japanese Journal of Applied Physics*, 37(Part 2, No. 10A), L1119–L1121. doi:10.1143/jjap.37.11119
  88. Alemu, D., Wei, H.-Y., Ho, K.-C., & Chu, C.-W. (2012). *Highly conductive PEDOT:PSS electrode by simple film treatment with methanol for ITO-free polymer solar cells*. *Energy & Environmental Science*, 5(11), 9662. doi:10.1039/c2ee22595f
  89. Swallow, J., Williamson, B. A. D., Sathasivam, S., Birkett, M., Featherstone, T., Murgatroyd, P., ... Veal, T. (2019). *Resonant doping for high mobility transparent conductors: the case of Mo-doped In<sub>2</sub>O<sub>3</sub>*. *Materials Horizons*. doi:10.1039/c9mh01014a
  90. Vlaanderen, J., Pronk, A., Rothman, N., Hildesheim, A., Silverman, D., Hosgood, H. D., ... Vermeulen, R. (2017). *A cross-sectional study of changes in markers of immunological effects and lung health due to exposure to multi-walled carbon nanotubes*. *Nanotoxicology*, 11(3), 395–404. doi:10.1080/17435390.2017.1308031
  91. Kisin, E. R., Murray, A. R., Sargent, L., Lowry, D., Chirila, M., Siegrist, K. J., ... Shvedova, A. A. (2011). *Genotoxicity of carbon nanofibers: Are they potentially more or less dangerous than carbon nanotubes or asbestos?* *Toxicology and Applied Pharmacology*, 252(1), 1–10. doi:10.1016/j.taap.2011.02.001
  92. Monteiro-Riviere, N. A., & Inman, A. O. (2006). *Challenges for assessing carbon nanomaterial toxicity to the skin*. *Carbon*, 44(6), 1070–1078. doi:10.1016/j.carbon.2005.11.004

93. Lam, C., James, J. T., McCluskey, R., Arepalli, S., & Hunter, R. L. (2006). *A Review of Carbon Nanotube Toxicity and Assessment of Potential Occupational and Environmental Health Risks*. *Critical Reviews in Toxicology*, 36(3), 189–217. doi:10.1080/10408440600570233
94. Dincer, C., Bruch, R., Costa-Rama, E., Fernández-Abedul, M. T., Merkoçi, A., Manz, A., ... Güder, F. (2019). *Disposable Sensors in Diagnostics, Food, and Environmental Monitoring*. *Advanced Materials*, 1806739. doi:10.1002/adma.201806739
95. Heineman, W. R., & Jensen, W. B. (2006). *Leland C. Clark Jr. (1918–2005)*. *Biosensors and Bioelectronics*, 21(8), 1403–1404. doi:10.1016/j.bios.2005.12.005
96. Vo-Dinh, T., & Cullum, B. (2000). *Biosensors and biochips: advances in biological and medical diagnostics*. *Fresenius' Journal of Analytical Chemistry*, 366(6-7), 540–551. doi:10.1007/s002160051549
97. Juzgado, A., Soldà, A., Ostric, A., Criado, A., Valenti, G., Rapino, S., ... Prato, M. (2017). *Highly sensitive electrochemiluminescence detection of a prostate cancer biomarker*. *Journal of Materials Chemistry B*, 5(32), 6681–6687. doi:10.1039/c7tb01557g
98. Jirimali, H.D. (2019) *Advance Biomedical Sensors and Transducers*. In: Paul S. (eds) *Biomedical Engineering and its Applications in Healthcare*. Springer, Singapore. doi:10.1007/978-981-13-3705-5\_7
99. Lipani, L., Dupont, B. G. R., Doungmene, F., Marken, F., Tyrrell, R. M., Guy, R. H., & Ilie, A. (2018). *Non-invasive, transdermal, path-selective and specific glucose monitoring via a graphene-based platform*. *Nature Nanotechnology*, 13(6), 504–511. doi:10.1038/s41565-018-0112-4
100. Hartono, A., Sanjaya, E., & Ramli, R. (2018). *Glucose Sensing Using Capacitive Biosensor Based on Polyvinylidene Fluoride Thin Film*. *Biosensors*, 8(1), 12. doi:10.3390/bios8010012
101. Liu, Y., Dong, X., & Chen, P. (2012). *Biological and chemical sensors based on graphene materials*. *Chem. Soc. Rev.*, 41(6), 2283–2307. doi:10.1039/c1cs15270j
102. Justino, C. I. L., Gomes, A. R., Freitas, A. C., Duarte, A. C., & Rocha-Santos, T. A. P. (2017). *Graphene based sensors and biosensors*. *TrAC Trends in Analytical Chemistry*, 91, 53–66. doi:10.1016/j.trac.2017.04.003
103. Xiao, Y., & Li, C. M. (2008). *Nanocomposites: From Fabrications to Electrochemical Bioapplications*. *Electroanalysis*, 20(6), 648–662. doi:10.1002/elan.200704125
104. Luo, J., Jiang, S., Zhang, H., Jiang, J., & Liu, X. (2012). *A novel non-enzymatic glucose sensor based on Cu nanoparticle modified graphene sheets electrode*. *Analytica Chimica Acta*, 709, 47–53. doi:10.1016/j.aca.2011.10.025
105. Shi, J., Zhang, H., Snyder, A., Wang, M., Xie, J., Marshall Porterfield, D., & Stanciu, L. A. (2012). *An aqueous media based approach for the preparation of a biosensor platform composed of graphene oxide and Pt-*

- black*. *Biosensors and Bioelectronics*, 38(1), 314–320. doi:10.1016/j.bios.2012.06.007
106. Xue, K., Zhou, S., Shi, H., Feng, X., Xin, H., & Song, W. (2014). *A novel amperometric glucose biosensor based on ternary gold nanoparticles/polypyrrole/reduced graphene oxide nanocomposite*. *Sensors and Actuators B: Chemical*, 203, 412–416. doi:10.1016/j.snb.2014.07.018
107. Lin, C.-T., Loan, P. T. K., Chen, T.-Y., Liu, K.-K., Chen, C.-H., Wei, K.-H., & Li, L.-J. (2013). *Label-Free Electrical Detection of DNA Hybridization on Graphene using Hall Effect Measurements: Revisiting the Sensing Mechanism*. *Advanced Functional Materials*, 23(18), 2301–2307. doi:10.1002/adfm.201202672
108. Bora, C., & Dolui, S. K. (2012). *Fabrication of polypyrrole/graphene oxide nanocomposites by liquid/liquid interfacial polymerization and evaluation of their optical, electrical and electrochemical properties*. *Polymer*, 53(4), 923–932. doi:10.1016/j.polymer.2011.12.054
109. Wu, L., Deng, D., Jin, J., Lu, X., & Chen, J. (2012). *Nanographene-based tyrosinase biosensor for rapid detection of bisphenol A*. *Biosensors and Bioelectronics*, 35(1), 193–199. doi:10.1016/j.bios.2012.02.045
110. Cecchelli, R., Berezowski, V., Lundquist, S., Culot, M., Renftel, M., Dehouck, M.-P., & Fenart, L. (2007). *Modelling of the blood–brain barrier in drug discovery and development*. *Nature Reviews Drug Discovery*, 6(8), 650–661. doi:10.1038/nrd2368
111. Jonsson, A., Song, Z., Nilsson, D., Meyerson, B. A., Simon, D. T., Linderoth, B., & Berggren, M. (2015). *Therapy using implanted organic bioelectronics*. *Science Advances*, 1(4), e1500039–e1500039. doi:10.1126/sciadv.1500039
112. Paz, J. T., Davidson, T. J., Frechette, E. S., Delord, B., Parada, I., Peng, K., ... Huguenard, J. R. (2012). *Closed-loop optogenetic control of thalamus as a tool for interrupting seizures after cortical injury*. *Nature Neuroscience*, 16(1), 64–70. doi:10.1038/nn.3269
113. Kullmann, D. M., Schorge, S., Walker, M. C., & Wykes, R. C. (2014). *Gene therapy in epilepsy—is it time for clinical trials?* *Nature Reviews Neurology*, 10(5), 300–304. doi:10.1038/nrneurol.2014.43
114. Williamson, A., Rivnay, J., Kergoat, L., Jonsson, A., Inal, S., Uguz, I., ... Bernard, C. (2015). *Controlling Epileptiform Activity with Organic Electronic Ion Pumps*. *Advanced Materials*, 27(20), 3138–3144. doi:10.1002/adma.201500482
115. Khodagholy, D., Doublet, T., Gurfinkel, M., Quilichini, P., Ismailova, E., Leleux, P., ... Malliaras, G. G. (2011). *Highly Conformable Conducting Polymer Electrodes for In Vivo Recordings*. *Advanced Materials*, 23(36), H268–H272. doi:10.1002/adma.201102378
116. Pundir, C. S., Deswal, R., & Narwal, V. (2017). *Quantitative analysis of hydrogen peroxide with special emphasis on biosensors*. *Bioprocess and*

- Biosystems Engineering, 41(3), 313–329. <https://doi.org/10.1007/s00449-017-1878-8>
117. Skoog, D. A., Holler, F. J., Crouch, S. R. (2007). *Principles of Instrumental Analysis*. (6th ed.). Belmont, CA: Thomson Brooks/Cole. p. 169–173. ISBN 9780495012016
  118. Rocha, F. S., Gomes, A. J., Lunardi, C. N., Kaliaguine, S., & Patience, G. S. (2018). *Experimental Methods in Chemical Engineering: Ultraviolet Visible Spectroscopy|UV-Vis*. *The Canadian Journal of Chemical Engineering*. doi:10.1002/cjce.23344
  119. Thomas, O., Burgess, C. (2017). *UV-Visible Spectrophotometry of water and wastewater*. (2<sup>nd</sup> ed.). Elsevier. p.6-7. ISBN 978-0-444-63897-7
  120. Gorog, S. (2018). *Ultraviolet-Visible spectroscopy in pharmaceutical analysis*. CRC Press. Chapter 2. B. ISBN-13: 9781315898322
  121. Gardiner, D.J. (1989). *Practical Raman spectroscopy*. Springer-Verlag. ISBN 978-0-387-50254-0
  122. Krishnan, R. S., & Shankar, R. K. (1981). *Raman effect: History of the discovery*. *Journal of Raman Spectroscopy*, 10(1), 1–8.
  123. Prof. Kioseoglou, G. *Raman and IR spectroscopy*, lecture on Hard Matter course, postgraduate program of Materials Science and Technology Department, University of Crete
  124. Lewis, E. N., Treado, P. J., & Levin, I. W. (1993). *A Miniaturized, No-Moving-Parts Raman Spectrometer*. *Applied Spectroscopy*, 47(5), 539–543. doi:10.1366/0003702934067144
  125. Cullum, B. M., Mobley, J., Chi, Z., Stokes, D. L., Miller, G. H., & Vo-Dinh, T. (2000). *Development of a compact, handheld Raman instrument with no moving parts for use in field analysis*. *Review of Scientific Instruments*, 71(4), 1602–1607. doi:10.1063/1.1150504
  126. [https://en.wikipedia.org/wiki/Raman\\_spectroscopy](https://en.wikipedia.org/wiki/Raman_spectroscopy) (Accessed on 21<sup>st</sup> January 2020)
  127. Bumrah, G. S., & Sharma, R. M. (2016). *Raman spectroscopy – Basic principle, instrumentation and selected applications for the characterization of drugs of abuse*. *Egyptian Journal of Forensic Sciences*, 6(3), 209–215. doi:10.1016/j.ejfs.2015.06.001
  128. Edwards, H. G. M. (2005). *Modern Raman spectroscopy—a practical approach*. Ewen Smith and Geoffrey Dent. John Wiley and Sons Ltd, Chichester, 2005. ISBN 0 471 49668 5 (cloth, hb); 0 471 49794 0 (pbk). *Journal of Raman Spectroscopy*, 36(8), 835–835. doi:10.1002/jrs.1320
  129. Settle, F.A. (1997). *Handbook of instrumental techniques for analytical chemistry*. Prentice Hall PTR. ISBN 0131773380
  130. Durickovic, I. (2016). *Using Raman spectroscopy for characterization of aqueous media and quantification of species in aqueous solution*. *World's Largest Science, Technology & Medicine*. 405-28. doi:10.5772/64550

131. Ferrari, A. C., & Robertson, J. (2000). *Interpretation of Raman spectra of disordered and amorphous carbon*. *Physical Review B*, 61(20), 14095–14107. doi:10.1103/physrevb.61.14095
132. Smith, B.C. (2011). *Fundamentals of Fourier Transform Infrared Spectroscopy*. (2<sup>nd</sup> Ed.). CRC Press. ISBN 978-1-4200-6930-3
133. Faix, O. (1992). *Fourier Transform Infrared Spectroscopy*. Springer Series in Wood Science, 83–109. doi:10.1007/978-3-642-74065-7\_7
134. Table 1: Principal IR absorptions for certain functional groups, [http://academics.wellesley.edu/Chemistry/chem211lab/Orgo\\_Lab\\_Manual/Appendix/Instruments/InfraredSpec/Chem211%20IR%20Lit%20Value%20Table.pdf](http://academics.wellesley.edu/Chemistry/chem211lab/Orgo_Lab_Manual/Appendix/Instruments/InfraredSpec/Chem211%20IR%20Lit%20Value%20Table.pdf) (Accessed on 2<sup>nd</sup> January 2020)
135. Diaspro, A., Bianchini, P., Vicidomini, G., Sheppard, C.J.R., Lanzano, L., Znacchi, F.C. and Galeno, L. (2016). *In the Realm of Super-Resolved Fluorescence Microscopy*. CRC Press. ISBN 978-1-4822-4434-2
136. Prof. Kyriakidis, G. and Dr. Binas, V. *Introduction to Electron Microscopy*, lecture on Electron Microscopy course, undergraduate program of Physics Department, University of Crete (UoC)
137. Masters, B. R. (2008). *History of the Optical Microscope in Cell Biology and Medicine*. Encyclopedia of Life Sciences. doi:10.1002/9780470015902.a0003082
138. [https://en.wikipedia.org/wiki/Current%E2%80%93voltage\\_characteristic](https://en.wikipedia.org/wiki/Current%E2%80%93voltage_characteristic) (Accessed on 4<sup>th</sup> January 2020)
139. Azarova, N. A., Owen, J. W., McLellan, C. A., Grimminger, M. A., Chapman, E. K., Anthony, J. E., & Jurchescu, O. D. (2010). *Fabrication of organic thin-film transistors by spray-deposition for low-cost, large-area electronics*. *Organic Electronics*, 11(12), 1960–1965. doi:10.1016/j.orgel.2010.09.008
140. Chan, C. K., Richter, L. J., Dinardo, B., Jaye, C., Conrad, B. R., Ro, H. W., ... Gundlach, D. J. (2010). *High performance airbrushed organic thin film transistors*. *Applied Physics Letters*, 96(13), 133304. doi:10.1063/1.3360230
141. Schwarz, J.A., Contescu, C.I. and Putyera, K. (2004). *Dekker encyclopédia of nanoscience and nanotechnology*. Volume 1. CRC Press. p. 263. ISBN 978-0-8247-5047-3
142. Li, G. (2020). *Direct laser writing of graphene electrodes*. *Journal of Applied Physics*, 127(1), 010901. doi:10.1063/1.5120056
143. Wan, Z., Wang, S., Haylock, B., Kaur, J., Tanner, P., Thiel, D., ... Li, Q. (2018). *Tuning the sub-processes in laser reduction of graphene oxide by adjusting the power and scanning speed of laser*. *Carbon*. doi:10.1016/j.carbon.2018.09.030
144. Zhang, Y., Guo, L., Wei, S., He, Y., Xia, H., Chen, Q., ... Xiao, F.-S. (2010). *Direct imprinting of microcircuits on graphene oxides film by femtosecond laser reduction*. *Nano Today*, 5(1), 15–20. doi:10.1016/j.nantod.2009.12.009

145. Casalino, G., Losacco, A. M., Arnesano, A., Facchini, F., Pierangeli, M., & Bonserio, C. (2017). *Statistical Analysis and Modelling of an Yb: KGW Femtosecond Laser Micro-drilling Process*. *Procedia CIRP*, 62, 275–280. doi:10.1016/j.procir.2016.06.111
146. Lai, Q., Zhu, S., Luo, X., Zou, M., & Huang, S. (2012). *Ultraviolet-visible spectroscopy of graphene oxides*. *AIP Advances*, 2(3), 032146. doi:10.1063/1.4747817
147. Kaniyoor, A., & Ramaprabhu, S. (2012). *A Raman spectroscopic investigation of graphite oxide derived graphene*. *AIP Advances*, 2(3), 032183. doi:10.1063/1.4756995
148. Ferrari, A. C., Meyer, J. C., Scardaci, V., Casiraghi, C., Lazzeri, M., Mauri, F., ... Geim, A. K. (2006). *Raman Spectrum of Graphene and Graphene Layers*. *Physical Review Letters*, 97(18). doi:10.1103/physrevlett.97.187401
149. Díez-Betriu, X., Álvarez-García, S., Botas, C., Álvarez, P., Sánchez-Marcos, J., Prieto, C., ... de Andrés, A. (2013). *Raman spectroscopy for the study of reduction mechanisms and optimization of conductivity in graphene oxide thin films*. *Journal of Materials Chemistry C*, 1(41), 6905. doi:10.1039/c3tc31124d
150. Rattana, Chaiyakun, S., Witit-anun, N., Nuntawong, N., Chindaudom, P., Oaew, S., ... Limsuwan, P. (2012). *Preparation and characterization of graphene oxide nanosheets*. *Procedia Engineering*, 32, 759–764. doi:10.1016/j.proeng.2012.02.009
151. Sudesh, Kumar, N., Das, S., Bernhard, C., & Varma, G. D. (2013). *Effect of graphene oxide doping on superconducting properties of bulk MgB<sub>2</sub>*. *Superconductor Science and Technology*, 26(9), 095008. doi:10.1088/0953-2048/26/9/095008
152. Valencia, C., Valencia, C., Zuluaga, F., Valencia, M., Mina, J., & Grande-Tovar, C. (2018). *Synthesis and Application of Scaffolds of Chitosan-Graphene Oxide by the Freeze-Drying Method for Tissue Regeneration*. *Molecules*, 23(10), 2651. doi:10.3390/molecules23102651
153. Rey-Garcia, F. (2012). *Planar waveguides obtained on commercial glass substrates by sol-gel and laser irradiation methods*. PhD Thesis. Universidade de Santiago de Compostela.
154. Childres, I., Jauregui, L.A., Park, W., Cao, H. and Chen, Y.P. (2013). *Chapter 19- Raman Spectroscopy of Graphene and Related Materials*. *New developments in Photon and Materials Research*. ISBN: 978-1-62618-339-1
155. Lee, Y.-K., Peng, Y. L., & Tomozawa, M. (1997). *IR reflection spectroscopy of a soda-lime glass surface during ion-exchange*. *Journal of Non-Crystalline Solids*, 222, 125–130. doi:10.1016/s0022-3093(97)90104-6
156. Tuinstra, F., & Koenig, J. L. (1970). *Raman Spectrum of Graphite*. *The Journal of Chemical Physics*, 53(3), 1126–1130. doi:10.1063/1.1674108

157. Smolsky, J. M., & Krasnoslobodtsev, A. V. (2018). *Nanoscopic imaging of oxidized graphene monolayer using tip-enhanced Raman scattering*. Nano Research. doi:10.1007/s12274-018-2158-x
158. Zhang, X., Yin, J., Peng, C., Hu, W., Zhu, Z., Li, W., ... Huang, Q. (2011). *Distribution and biocompatibility studies of graphene oxide in mice after intravenous administration*. Carbon, 49(3), 986–995. doi:10.1016/j.carbon.2010.11.005
159. Mokni, M., Maggioni, G., Kahouli, A., Carturan, S. M., Raniero, W., & Sylvestre, A. (2019). *Nanocomposite-parylene C thin films with high dielectric constant and low losses for future organic electronic devices*. Beilstein Journal of Nanotechnology, 10, 428–441. doi:10.3762/bjnano.10.42
160. Jorio, A., Ferreira, E. H. M., Moutinho, M. V. O., Stavale, F., Achete, C. A., & Capaz, R. B. (2010). *Measuring disorder in graphene with the G and D bands*. Physica Status Solidi (b), 247(11-12), 2980–2982. doi:10.1002/pssb.201000247
161. Shi, H., Wang, C., Sun, Z., Zhou, Y., Jin, K., & Yang, G. (2014). *Transparent conductive reduced graphene oxide thin films produced by spray coating*. Science China Physics, Mechanics & Astronomy, 58(1), 1–5. doi:10.1007/s11433-014-5614-y
162. Bhaumik, A., Haque, A., Taufique, M., Karnati, P., Patel, R., Nath, M., & Ghosh, K. (2017). *Reduced Graphene Oxide Thin Films with Very Large Charge Carrier Mobility Using Pulsed Laser Deposition*. Journal of Material Science & Engineering, 06(04). doi:10.4172/2169-0022.1000364
163. Deschamps, T., Martinet, C., Bruneel, J. L., & Champagnon, B. (2011). *Soda-lime silicate glass under hydrostatic pressure and indentation: a micro-Raman study*. Journal of Physics: Condensed Matter, 23(3), 035402. doi:10.1088/0953-8984/23/3/035402
164. Torrisi, L., Silipigni, L., & Cutroneo, M. (2018). *Radiation effects of IR laser on graphene oxide irradiated in vacuum and in air*. Vacuum, 153, 122–131. doi:10.1016/j.vacuum.2018.04.010
165. Ortigoza-Diaz, J., Scholten, K., Larson, C., Cobo, A., Hudson, T., Yoo, J., ... Meng, E. (2018). *Techniques and Considerations in the Microfabrication of Parylene C Microelectromechanical Systems*. Micromachines, 9(9), 422. doi:10.3390/mi9090422
166. Golda-Cepa, M., Engvall, K., Hakkarainen, M., & Kotarba, A. (2020). *Recent progress on parylene C polymer for biomedical applications: A review*. Progress in Organic Coatings, 140, 105493. doi:10.1016/j.porgcoat.2019.105493
167. Huang, Y., Wang, X., Zhang, X., Chen, X., Li, B., Wang, B., ... Ruoff, R. S. (2018). *Raman Spectral Band Oscillations in Large Graphene Bubbles*. Physical Review Letters, 120(18). doi:10.1103/physrevlett.120.186104

168. Bunch, J. S., Verbridge, S. S., Alden, J. S., van der Zande, A. M., Parpia, J. M., Craighead, H. G., & McEuen, P. L. (2008). *Impermeable Atomic Membranes from Graphene Sheets*. *Nano Letters*, 8(8), 2458–2462. doi:10.1021/nl801457b
169. Georgiou, T., Britnell, L., Blake, P., Gorbachev, R. V., Gholinia, A., Geim, A. K., ... Novoselov, K. S. (2011). *Graphene bubbles with controllable curvature*. *Applied Physics Letters*, 99(9), 093103. doi:10.1063/1.3631632
170. Ramírez-Jiménez, R., Álvarez-Fraga, L., Jimenez-Villacorta, F., Climent-Pascual, E., Prieto, C., & de Andrés, A. (2016). *Interference enhanced Raman effect in graphene bubbles*. *Carbon*, 105, 556–565. doi:10.1016/j.carbon.2016.04.076
171. Rokmana, A. W., Asriani, A., Suhendar, H., Triyana, K., Kusumaatmaja, A., & Santoso, I. (2018). *The Optical Properties of Thin Film Reduced Graphene Oxide/Poly (3,4 Ethylenedioxytriophene):Poly (Styrene Sulfonate)(PEDOT:PSS) Fabricated by Spin Coating*. *Journal of Physics: Conference Series*, 1011, 012007. doi:10.1088/1742-6596/1011/1/012007
172. Naliatha, R., Kumar, V., Kaura, I., & Singh, K. L. (2013). *Synthesis and Study of Bio-conjugated Graphene*. *Journal of NanoScience, NanoEngineering & Applications*, 3(3), 21-26
173. Lin, S., Yuan, S., Zhang, J., & Jiang, D. (2018). *Effects of Microwave Irradiation on Electricity of Graphene Oxide Films*. *Advanced Functional Materials*, 75–81. doi:10.1007/978-981-13-0110-0\_10